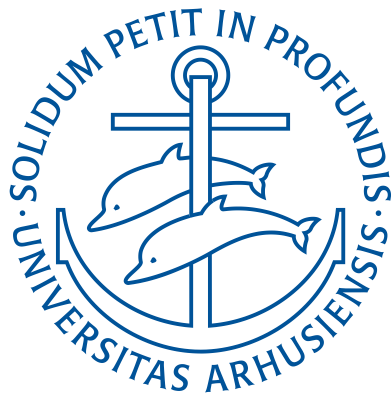


Pressure sensing and electro-optomechanics with suspended membrane arrays



PhD thesis

Sepideh Naserbakht



December 11, 2019
Department of Physics and Astronomy
Aarhus University

Abstract (English)

Suspended drum-shaped micro-/nano-mechanical resonators possessing high frequency and high quality factor resonances are ubiquitous in sensing and metrology applications, as their vibrations can be extremely sensitive to small external perturbations/forces and can efficiently couple to pressure due to their interaction with electromagnetic radiation or with a fluid. In this thesis, we investigate assemblies of suspended silicon nitride nanodrums oscillating at MHz frequencies with high mechanical quality factors ($\sim 10^5$) for pressure sensing and electro-optomechanics applications.

In the first part of the thesis, after discussing the generic mechanical and optical properties of such drums, the assembly and characterization of optomechanical sandwiches consisting of pairs of such membranes, suspended parallel and close to each other are presented.

The second part of the thesis reports on an investigation of the effects of air pressure on the mechanical properties of these membrane sandwiches. The resonance frequency shifts, damping and couplings between the resonators induced by the compression of the gas inside the gap between the membranes are studied in detail and the pressure responsivity and sensitivity of the realized squeeze film pressure sensors are evaluated.

In the last part, we investigate the electromechanical couplings induced in these membrane arrays via piezoelectricity. By applying a compressive force to the frame supporting the membranes in order to piezoelectrically control their tensile stress, noninvasive tuning of their vibrational mode spectrum, intermembrane coupling and enhancement of their nonlinear response under parametric actuation are demonstrated.

Abstract (Danish)

Suspenderede højkvalitets nanomekaniske resonatorer udnyttes hyppigt som sensorer og for præcisionsmålinger, idet deres vibrationer kan være ekstremt følsomme over for små perturbationer, induceret fx af trykket fra elektromagnetisk stråling eller fra en væske. I denne afhandling undersøger vi rækker af suspenderede silicium nitrid membraner, med MHz resonansfrekvenser og høje mekaniske kvalitetsfaktorer ($\sim 10^5$), for tryksensor og elektro-optomekaniske anvendelser.

I den første del af afhandlingen, efter en diskussion af de generelle mekaniske og optiske egenskaber af sådanne resonatorer, præsenteres fabrikationen og karakteriseringen af optomekaniske sandwicher bestående af et par membraner, suspenderet parallelt tæt på hinanden.

I den anden del af afhandlingen undersøges hvordan lufttrykket påvirker de mekaniske egenskaber af sådanne sandwicher. Resonansfrekvensskift, dæmpning og kobling mellem membranerne induceret af sammentrykningen af gasset mellem membranerne måles og diskuteres grundigt, og tryksensorernes respons og følsomhed evalueres.

I den sidste del undersøges elektromekaniske koblinger i disse rækker. Ved hjælp af en piezoelektrisk induceret sammentrykkende kraft på membranernes ramme, demonstreres en ikke invasiv kontrol af membranernes resonansfrekvenser, kobling mellem dem, såvel som en forstærket ikke-lineær respons til parametrisk excitering.

List of Publications

- Sepideh Naserbakht, Andreas Naesby, and Aurélien Dantan, "Frequency tuning and parametric amplification of the vibrations of coupled nanomembranes by piezoelectrical control of their tensile stress", Manuscript in preparation
- Sepideh Naserbakht and Aurélien Dantan , "Squeeze film pressure sensors based on SiN membrane sandwiches", Sensors and Actuators A: Physical 298, 111588, 2019
- Sepideh Naserbakht, Andreas Naesby, and Aurélien Dantan, "Electromechanics in vertically coupled nanomembranes", Applied Physics Letters 115, 061105, 2019
- Andreas Naesby, Sepideh Naserbakht, and Aurélien Dantan, "Effects of pressure on suspended micromechanical membrane arrays", Applied Physics Letters 111, 201103, 2017

Contents

1	Introduction	1
2	Basic theory	7
2.1	Mechanics	7
2.1.1	Square drum mechanical oscillator	7
2.1.2	Single mode dynamics	9
2.1.2.1	Thermal oscillations	10
2.1.2.2	Periodically driven oscillations	14
2.1.2.3	Parametrically driven oscillator	15
2.1.2.4	Duffing oscillator	18
2.1.3	Coupled oscillators	21
2.2	Optics	25
2.2.1	One-dimensional transfer matrix model	25
2.2.2	Single membrane	28
2.2.3	Double-membrane array	29
2.3	Optomechanics	30
3	Membrane array assembly and characterization	35
3.1	Si ₃ N ₄ membrane arrays	35
3.2	Previous work	37
3.2.1	Fabrication and optical characterization	37
3.2.2	Effect of parallelism on the transmission	40
3.3	Second generation of double-membrane arrays	41
3.3.1	Fabrication	41
3.3.1.1	Experimental setup	41
3.3.1.2	Calibration	43
3.3.2	Optical characterization	45
3.3.2.1	"Large" d	45
3.3.2.2	"Medium" d	48
3.3.2.3	"Short" d	50
3.3.3	Summary	52

3.3.4	Mechanical characterization	53
3.3.4.1	Experimental setup	53
3.3.4.2	Spectrum analyzer measurements	56
3.3.4.3	Q determination	58
3.3.4.3.1	Thermal noise spectra	58
3.3.4.3.2	Ringdown spectroscopy	60
3.3.4.4	Effect of the resolution bandwidth	62
4	Pressure sensing with membrane sandwiches	65
4.1	Effects of pressure on the mechanics	66
4.1.1	Knudsen number	66
4.1.2	Squeeze film effect	68
4.1.3	Squeeze film dynamics in the rarefied air regime	72
4.2	Experimental setup	73
4.3	Experimental results	75
4.3.1	Effects of pressure on "medium" arrays	75
4.3.2	Effects of pressure on "short" arrays	80
4.3.2.1	2.95 μm double-membrane array	82
4.3.2.2	2.10 μm double-membrane array	86
4.3.3	Pressure sensitivity	88
4.4	Conclusion	91
5	Electromechanics in membrane arrays	93
5.1	Electromechanical array	94
5.1.1	Electromechanical array assembly	94
5.1.2	Experimental characterization	95
5.1.3	Experimental results	96
5.1.3.1	Single membrane	96
5.1.3.2	"Long" array	97
5.1.3.3	"Medium" array	99
5.2	Parametric actuation	103
5.2.1	Parametric gain study	104
5.2.2	Amplification at different bias voltages	108
5.3	Nonlinearity of the linearly driven mode	110
5.4	Conclusion	113
6	Conclusion	115

1

Introduction

Optomechanics is a fastly developing field that deals with the interaction of electromagnetic (EM) radiation with mechanical motion as a result of radiation pressure [1, 2]. Radiation pressure results from the exchange of momentum between a movable object and electromagnetic radiation impinging on it. The existence of radiation pressure was first conjectured in the 17th century by Kepler while observing a comet transit, and put later on firmer theoretical grounds by Maxwell before the first experimental observations in 1901 by Nichols and Hull, and Lebedew [1]. On the other hand, interferometry with EM radiation is a widespread technique to measure extremely small displacements and detect small forces. An important motivation for studying the effects of radiation pressure on movable mirrors was provided by the early gravitational wave detectors built in the 1970s and 1980s which were large Michelson interferometers, with kilometers-long optical cavity (as arms) and suspended kilogram mirrors, that have been used to detect very small displacements caused by the gravitational waves [3–5]. Since then, progress in micro/nano fabrication has led to the design of very small and high-quality mechanical resonators for which the operation regime is dominated by the optical forces [6–10] and which can be used in MEMS sensing, telecommunication or even to investigate mechanics in the quantum regime [11–13].

Micro/nano mechanical resonators can efficiently couple to EM radiation pressure over a broad spectrum, from low frequency (radiofrequency, microwave) to high frequency (optical) domain. Hence, using micro-opto-electromechanical (MOEM) systems, such as micro-/nano-beams, cantilevers, and membranes, it is possible

to bridge the gap between these two domains [14]. In that context, suspended drum resonators made of low loss material such as silicon nitride are particularly interesting, as their vibrations can be made to strongly coupled to either cavity microwave [15, 16] or optical [10] fields and be used in the context of cavity optomechanics [1, 17] for e.g. electro-optical conversion or transduction of signals [18–20].

Electro- or optomechanical arrays consisting of multiple drum resonators are also interesting and may offer attractive features as compared to single resonators, such as the enhancement of radiation pressure force [21, 22], the emergence of collective dynamics [21–25], the exploitation of synchronization [26], the engineering of phonon dynamics [27, 28], the generation of multimode squeezing or entanglement [29–32]. To illustrate the principle of radiation pressure force enhancement, for instance, Fig. 1.1a shows a pair of parallel suspended drum resonators transmitting an EM wave. The multiple momentum exchanges between the resonators and the photons bouncing back and forth between them can create strong optomechanical correlations [21]. Such optomechanical arrays –their fabrication, characterization, and applications– are the focus of this thesis.

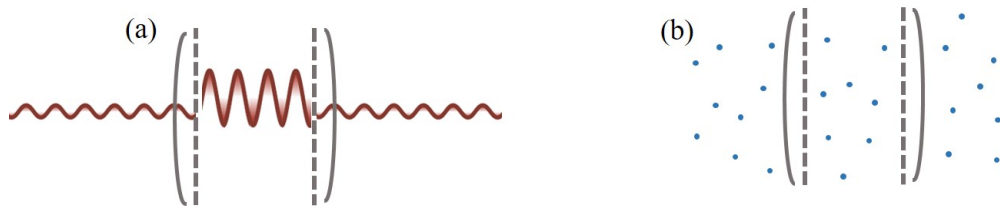


Figure 1.1: Schematic picture of a pair of parallel resonators experiencing (a) radiation pressure and (b) pressure from a compressed fluid. The dashed vertical lines indicate the equilibrium positions.

Suspended drums with a large area/small thickness are also naturally sensitive to the pressure exerted by a surrounding fluid, as the interaction with the fluid affects their mechanical properties [33], and this makes them excellent candidates for pressure sensing [34]. At high pressures, where pressure sensors based on diaphragms and capacitive drums are typically used, fluid-structure interactions typically become the dominant source of damping and limit the quality factors of the mechanical resonances [34]. At low pressures, the damping of vibrating suspended membranes is essentially determined by material properties and boundaries [35]. However, not only damping is influenced by the interaction with the gas. For instance, for a pair of parallel suspended resonators as depicted in Fig. 1.1b, the isothermic compression of a fluid in the free molecular regime between the resonators results in can substantially modify the mechanical frequencies and

damping (squeeze film effect). The squeeze film induced-spring constant in particular can be directly related to the pressure in a species-independent fashion [36–41]. Squeeze film effects have been investigated by different research groups for pressure sensing application [38, 39, 41–49] and squeeze film pressure sensors [36, 50] allow in principle absolute and direct pressure measurements. In this project, we studied the effect of pressure on suspended membrane sandwiches and investigated their potential use as absolute pressure sensors in the free molecular flow regime.

As above-mentioned, for MEOM applications, e.g. electro-optical conversion, integrating both electrical and optical actuation to the mechanics can be obtained in different ways, such as patterning of electrodes on membrane resonators [18, 20, 51]. For membrane arrays, dynamical tuning of the mechanics and engineering of couplings can be achieved by modifying the stress of the mechanical resonator e.g. capacitively [50, 52], electro- or photo-thermally [53, 54], by bending [55] or by heating [56]. Engineering linear and nonlinear couplings in such arrays is desirable for a wide range of collective dynamics studies such as synchronization [57, 58] or coherent phonon manipulations between them [59–65]. Later on in this thesis, by applying a compressive force to the frame supporting the membranes, we investigate the electromechanics in fabricated electro-optomechanical membrane arrays and demonstrate noninvasive tuning of their linear and nonlinear mechanical response –properties which are essential for the above-mentioned applications.

The resonators studied in this thesis are commercial Si_3N_4 (SiN) membranes (see Fig. 1.2) made by NORCADA [66] using Low Pressure Chemical Vapour Deposition (LPCVD). These are thin (100 nm), high tensile stress (GPa) silicon nitride square drums with $\sim\text{mm}^2$ area, exhibiting mechanical modes in the MHz range with record high-quality factors ($> 10^6$) [67, 68] and small effective masses (ng). In addition to these outstanding mechanical properties, the low loss of silicon nitride allows for inserting them into standard Fabry Perot cavities without deteriorating the cavity finesse. This approach –also referred to as ”membrane in the middle”– was pioneered by J. Harris’ group at Yale [69] and has since then been widely used, particularly in the context of quantum optomechanics [17–20, 26, 32, 51, 70–76]. Some recent experimental achievements with SiN membrane resonators include the observation of the radiation pressure shot-noise [19], the optomechanical cooling of their vibrations to or close to the ground state [51, 73], the observation of ponderomotive squeezing [32], the observation of optomechanically induced transparency at room temperature [77], their coupling to cold atoms [78, 79], or electro-optical conversion [18, 20, 80]. The first experiments of coupling arrays of SiN membranes, as pioneered in Aarhus [81], to optical cavity fields have also very recently been performed [74, 82, 83], opening new avenues for exploring collective optomechanics

with these outstanding resonators.

In this thesis, progress in assembly, characterizing and functionalizing such SiN membrane arrays for optomechanics and sensing applications are reported and the outline of the thesis is the following:



Figure 1.2: Picture of commercial SiN membrane on Si chip.

- Chapter 2 introduces the theoretical models that will be used to describe the mechanical and optical properties of the resonators, as well as their interferometric measurements. It begins with the description of the vibrations of square drum resonators and discusses generic dynamics of single/coupled, harmonic/anharmonic oscillators. The optics section discusses light propagation in systems of one-dimensional scatterers and introduces the transfer matrix formalism. The chapter ends with a discussion on the basic principles of the optical interferometer which will be used to measure the mechanical motion of the membranes.
- Chapter 3 reports on the fabrication process and optomechanical characterization of SiN membrane arrays. The chapter begins with an overview of these resonators and after a brief review of the work carried out by Bhagya Nair in her PhD thesis [84] on the first generation of arrays, as well as the challenges for achieving high parallelism. The new experimental setup to improve the assembly process is detailed and the assembly and optical characterization of various double-membrane arrays are discussed. Finally, the interferometry setup and methods used for monitoring the vibrations of the resonators is presented.
- Chapter 4 presents a practical application of SiN membrane sandwiches as pressure sensors containing the results published in [85, 86]. The chapter begins with a general discussion of the dynamics of plates oscillating in a fluid and introduces the hydrodynamics models, including the squeeze film effect, required to interpret the experimental observations. The results of the

experimental investigations of the effect of pressure on the mechanical properties of various membrane sandwiches are then reported, and the potential of these resonators for absolute pressure sensing are discussed.

- Chapter 5 deals with the investigation of electromechanical couplings induced in double-membrane arrays by piezoelectrical control of their tensile stress presented in [87, 88]. The experimental details including the fabrication and installation of the samples are first described as well as the experimental setup. The chapter continues with an experimental investigation of the noninvasive tuning and coupling of the mechanical modes of the membranes. Their dynamical actuation and the tuning of their nonlinear response via piezoelectricity is also reported. Such an activation is achieved by performing parametric amplification of the thermal fluctuations of membranes' fundamental modes, which is demonstrated, along with observations of an enhancement of the nonlinear response evidenced by reduction of the parametric oscillation thresholds due to the bias voltage.
- Chapter 6 concludes with a summary of the results achieved in this thesis and the future prospects of using such resonator arrays for optomechanics and sensing.

2

Basic theory

In order to understand and model the experimental observations presented in the next chapters, this chapter introduces basic theoretical tools in mechanics, optics, and optomechanics. The chapter begins with how the vibrational modes of square drum membranes are described and discusses their dynamics in terms of single and coupled mechanical oscillator models in Sec. 2.1. It is followed by Sec. 2.2 where the propagation of electromagnetic plane waves in a lossless medium using Maxwell's equations leads to the introduction of the transfer matrix model (TMM). The optical properties and transmission of membranes and membrane arrays are then discussed in the framework of this one-dimensional scattering theory. Section 2.3 ends the chapter by explaining the principle of the measurement of the vibrations of the membranes via optical interferometry.

2.1 Mechanics

2.1.1 Square drum mechanical oscillator

The mechanical oscillators used in this project and shown in Fig. 2.1 are thin, high tensile stress square membranes having uniformly distributed density across the square region and clamped to a frame which defines boundary conditions for the deformations of the square drum and allows for the existence of transverse vibrations (two-dimensional standing waves). The study of such structures is based on discussions in [70, 89–92].

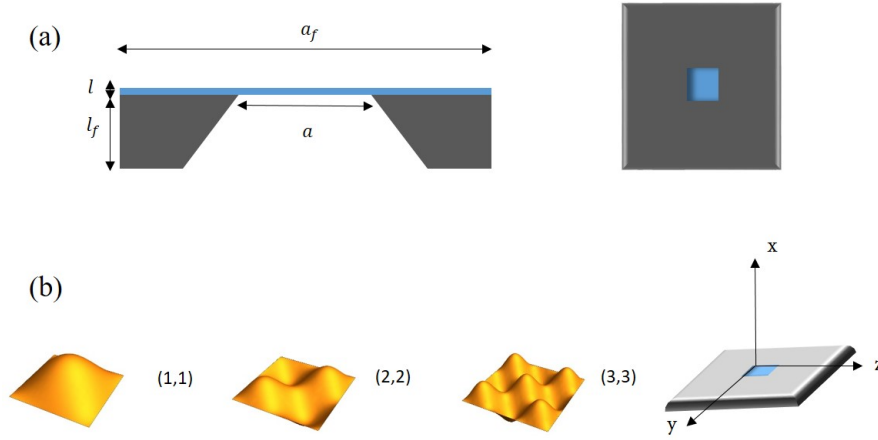


Figure 2.1: (a) Schematic picture of a thin membrane with thickness l and transverse dimension a , clamped on a square frame with transverse dimension $a_f \gg a$ and thickness $l_f \gg l$. (b) Amplitudes of the square drum modes (1,1), (2,2) and (3,3).

A first assumption comes from the bending properties of the vibrating plate. Since the membrane has a very large transverse size (0.5 mm) as compared to its thickness (100 nm), one can make use of the "thin" plate approximation and neglect the volume changes due to the transverse vibrations (see Fig. 2.1a). Due to the boundary conditions imposed by the frame in the (yz) -plane, the amplitude and the speed of the standing waves at the boundary have to be equal to zero and the elastic wave equation describing the displacement in the x -direction, $u(y, z, t)$, leads to

$$-\frac{D}{l} \nabla^4 u + T \nabla^2 u = \rho \frac{\partial^2 u}{\partial t^2}, \quad (2.1)$$

where ρ is the membrane density, l is the thickness and T is the in-plane tension. The right-hand side represents the kinetic energy of the mass element $\rho dydz$ of the membrane, while the left-hand side represents its potential energy deformations due to flexural rigidity and tension. The flexural rigidity D is defined as:

$$D = \frac{El^3}{12(1-\nu^2)} \quad (2.2)$$

where E and ν are Young's modulus and Poisson's ratio, respectively.

In order to satisfy the boundary condition, $u = \partial^2 u / \partial n^2 = 0$, where n is the coordinate normal to the boundary and we also have $y \in [0, a]$, $z \in [0, a]$. Solutions

for the displacement are two-dimensional standing waves fluctuating harmonically with a frequency ω_{mn} :

$$u_{mn}(y, z, t) = x(t) \sin\left(\frac{m\pi y}{a}\right) \sin\left(\frac{n\pi z}{a}\right), \quad x(t) = x_0 \sin(\omega_{mn}t + \phi), \quad (2.3)$$

where ω_{mn} is the normal mode frequency characterized by two integers m and n , and ϕ is an arbitrary phase. The variations of the amplitude are given as a function of y , z and are presented in Fig. 2.1b for the lowest $m = n$ modes.

The membranes that we consider acquire high tensile stress (\sim GPa) during the deposition process, which means that the bending terms can effectively be neglected with respect to the tensile stress terms in Eq. (2.1):

$$T \nabla^2 u = \rho \frac{\partial^2 u}{\partial t^2}. \quad (2.4)$$

This gives the following expression for the resonance frequencies of a tensile stress-dominated square drum:

$$\omega_{mn} |_{D=0} = \frac{\pi}{a} \sqrt{\frac{T}{\rho}} \sqrt{m^2 + n^2}, \quad (m, n \in \mathbb{N}^+). \quad (2.5)$$

2.1.2 Single mode dynamics

For the silicon nitride membranes we consider in this work, intrinsic damping is essentially due to clamping losses [70] and it can be considered as a viscous force [92], although generally, it is possible to have some other forms of dissipation in such a structure. The study of the dynamics of a single vibrational mode in this section follows the discussions in [70, 91, 92].

We focus on the evolution of the amplitude $x(t)$ of a single vibrational mode, whose displacement is of the form Eq. (2.3) and whose effective mass is m . Including a viscous damping force, its evolution can be described by a single damped harmonic oscillator equation:

$$m\ddot{x}(t) + m\gamma\dot{x}(t) + m\omega_m^2 x(t) = F_{th}(t) + F_d(t), \quad (2.6)$$

where m is the effective mass of the mode considered, ω_m is the resonance frequency, γ is the mechanical damping rate which gives the loss of mechanical energy to the environment and F_{th} and F_d are the thermal fluctuation force and the potential external driving force, respectively. The thermal fluctuation force F_{th} describes the coupling with a thermal bath at equilibrium temperature T . The

driven force F_d can be an oscillating force applied externally to coherently drive the mechanical oscillations, as will be discussed later.

A key parameter for the dynamics of the mechanical oscillator is the dimensionless quality factor, Q , which is defined as 2π times the total energy of the system, divided by the energy loss per cycle of oscillation:

$$Q = 2\pi \frac{W_m}{\Delta W_m}. \quad (2.7)$$

Based on the ratio of the damping γ to the resonant frequency ω_m , the mechanical system can evolve in an under-damped ($\omega_m \gg \gamma$), an over-damped ($\omega_m \ll \gamma$) or a critically-damped ($\omega_m = \gamma$) regime. For an under-damped harmonic oscillator in absence of external force, ΔW_m can be determined by the work done via the oscillator on the environment over a single cycle:

$$\Delta W_m = \oint m\gamma \dot{x} dx = \int_0^{2\pi/\omega_m} \dot{x}^2 dt = 2\pi \frac{\gamma}{\omega_m} W_m, \quad (2.8)$$

which gives:

$$Q_m = \frac{\omega_m}{\gamma}. \quad (2.9)$$

The modes of the membrane resonators used in this work, typically have Q factors in the range $10^4 - 10^6$ and operate well in the under-damped regime.

2.1.2.1 Thermal oscillations

In the absence of the external drive force ($F_d = 0$), the motion dynamics of the system are only affected by thermal fluctuations:

$$\ddot{x}(t) + \gamma \dot{x}(t) + \omega_m^2 x(t) = \frac{F_{th}(t)}{m}. \quad (2.10)$$

In order to discuss the spectral content of the solution to this equation, we introduce the Fourier transform (FT) and inverse Fourier transform (IFT) as:

$$x(t) = \int_{-\infty}^{+\infty} x(\omega) e^{i\omega t} \frac{d\omega}{2\pi}, \quad (2.11)$$

$$x(\omega) = \int_{-\infty}^{+\infty} x(t) e^{-i\omega t} dt. \quad (2.12)$$

Using this convention we can introduce the Dirac-delta function:

$$\delta(\omega - \omega_m) = \int_{-\infty}^{+\infty} e^{-i\omega_m t} e^{-i\omega t} dt, \quad (2.13)$$

which gives:

$$x(t) = x_0 \cos \omega_m t = \frac{x_0}{2} (e^{i\omega_m t} + e^{-i\omega_m t}), \quad (2.14)$$

$$x(\omega) = \frac{x_0}{2} [\delta(\omega - \omega_m) + \delta(\omega + \omega_m)]. \quad (2.15)$$

If $x(t)$ is a stationary fluctuating variable, both $x(t)$ and $x(t + \tau)$ have the same statistics, so that:

$$\langle x(t)x(t + \tau) \rangle = \lim_{T \rightarrow \infty} \int_{-\frac{T}{2}}^{\frac{T}{2}} x(t)x(t + \tau) dt. \quad (2.16)$$

The FT of this correlation function gives the (double-sided) spectral density:

$$S_{xx}(\omega) \equiv \int_{-\infty}^{+\infty} \langle x(t)x(t + \tau) \rangle e^{-i\omega\tau} d\tau. \quad (2.17)$$

The variance of the fluctuations of $x(t)$ is then given by integration of the spectral density over all positive and negative frequencies:

$$\langle x(t)^2 \rangle = \int_{-\infty}^{+\infty} S_{xx}(\omega) \frac{d\omega}{2\pi}. \quad (2.18)$$

If $x(t)$ is real, one can show that $S_{xx}(\omega) = S_{xx}(-\omega)$ and then it is possible to introduce the "single-sided" spectral density:

$$S_x(\omega) \equiv 2S_{xx}(\omega) \quad \text{for } \omega \geq 0. \quad (2.19)$$

In this case,

$$\langle x^2(t) \rangle = \int_0^{+\infty} S_x(\omega) \frac{d\omega}{2\pi}. \quad (2.20)$$

Now, by Fourier transforming Eq. (2.10), we get the Fourier component of the fluctuations of x at frequency ω :

$$x(\omega) = \frac{F_{th}(\omega)}{\omega_m^2 - \omega^2 - i\gamma\omega}. \quad (2.21)$$

For thermal fluctuations, $F_{th}(t)$ has a zero mean value in time :

$$\langle F_{th}(t) \rangle = 0, \quad (2.22)$$

and a nonzero correlation function given by

$$\langle F_{th}(t)F_{th}(t') \rangle = K\delta(t - t'), \quad (2.23)$$

where K is a constant; it shows that the noise is entirely uncorrelated for different times and no memory exists between each excitation. This implies:

$$\langle F_{th}(\omega) \rangle = 0, \quad (2.24)$$

and the correlation function in Fourier space is

$$\langle F_{th}(\omega) F_{th}(\omega') \rangle = \int dt dt' \langle F_{th}(t) F_{th}(t') \rangle e^{-i\omega t} e^{-i\omega' t'} = K \delta(\omega + \omega'). \quad (2.25)$$

Using the Fluctuation-dissipation theorem one can show that

$$K = S_{F_{th}}(\omega) = 4k_B T \gamma m, \quad (2.26)$$

where k_B is the Boltzmann constant.

Using Eq. (2.21), the thermal noise spectrum of $x(\omega)$ is given by:

$$S_{xx}(\omega) = \frac{\frac{S_{F_{th}}(\omega)}{m^2}}{|(\omega_m^2 - \omega^2) + i\gamma^2 \omega^2|^2}, \quad (2.27)$$

$$S_x(\omega) = 2S_{xx}(\omega) = \frac{\frac{4k_B T \gamma}{m}}{(\omega_m^2 - \omega^2)^2 + \gamma^2 \omega^2}. \quad (2.28)$$

Making the high-Q oscillation assumption ($\omega_m \gg \gamma$) and assuming velocity damping (i.e γ is independent of ω), one can use the following approximations

$$\omega_m^2 - \omega^2 \simeq 2\omega_m(\omega_m - \omega), \quad (2.29)$$

and

$$(\omega_m^2 - \omega^2)^2 + \gamma^2 \omega^2 \simeq 4\omega_m^2 \left[(\omega_m - \omega)^2 + \frac{\gamma^2}{4} \right], \quad (2.30)$$

to obtain

$$S_x(\omega) \simeq \frac{2k_B T \gamma}{m\omega_m^2} \frac{1}{(\omega_m - \omega)^2 + \frac{\gamma^2}{4}}, \quad (2.31)$$

which is a Lorentzian function of ω , centered at ω_m with a Full Width at Half Maximum (FWHM) given by γ . Figure 2.2 shows power spectra density for a weakly damped mechanical mode at resonance frequency $\omega_m/(2\pi) = 1$ MHz using $m = 8.4$ ng, $T = 298$ K, $k_B = 1.38 \times 10^{-23}$ m²kg/(s²K) for $Q = 10$ (Fig. 2.2a) and $Q = 10^4$ (Fig. 2.2b) and two models of with (Eq. (2.31) in blue) and without (Eq. (2.28) in red) the high-Q assumption. Since both models in Fig. 2.2b, are mostly

the same except in off-resonant frequencies where there is a small fraction of energy ($\sim 1/Q$) difference, one can use the Lorentzian approximation to describe this system.

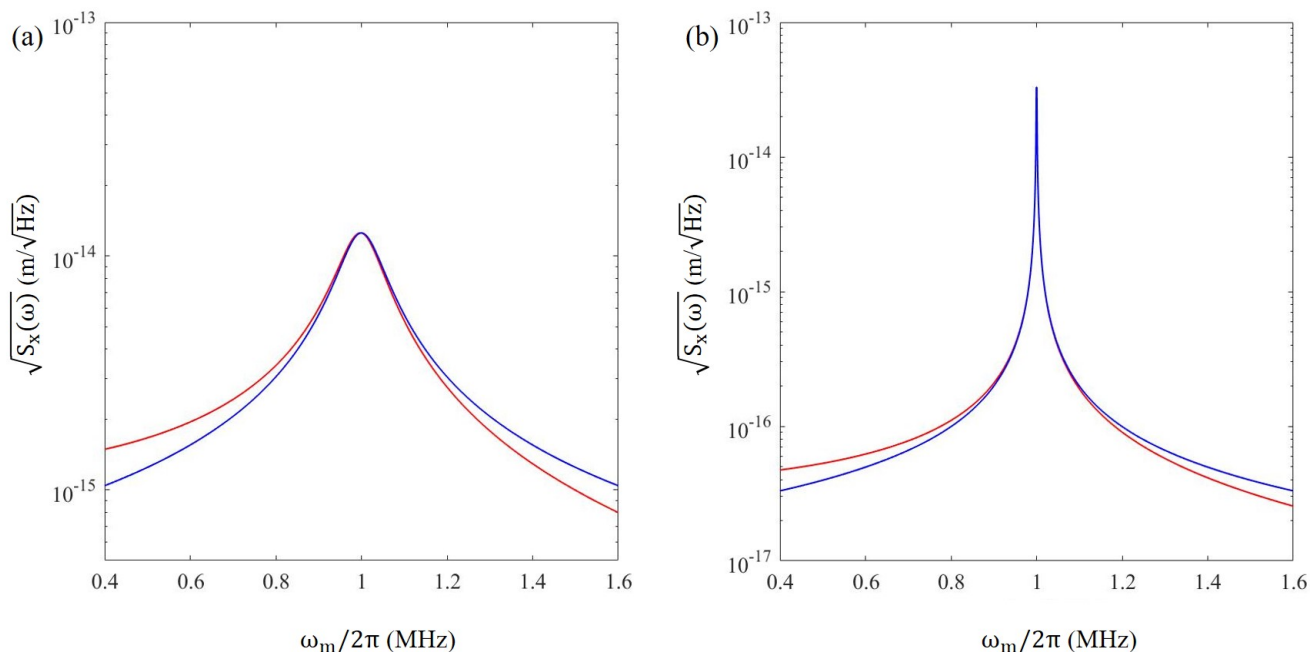


Figure 2.2: Power spectral density of displacement fluctuations for a Brownian oscillator with $\omega_m/(2\pi) = 1$ MHz, $m = 8.4$ ng, $T = 298$ K, $k_B = 1.38 \times 10^{-23}$ m²kg/(s²K), (a) $Q = 10$ and (b) $Q = 10^4$. Red and blue lines in both plots represent the model for velocity damping in Eq. (2.28) and the Lorentzian approximation in Eq. (2.31), respectively.

The variance of the thermal fluctuations is obtained by integrating the thermal noise spectrum:

$$\begin{aligned}
 \langle x^2(t) \rangle &= \int_0^\infty S_x(\omega) \frac{d\omega}{2\pi} \\
 &= \frac{2k_B T \gamma}{m\omega_m^2} \int_0^\infty \frac{\frac{d\omega}{2\pi}}{(\omega_m - \omega)^2 + (\frac{\gamma}{2})^2} \\
 &= \frac{k_B T}{m\omega_m^2},
 \end{aligned} \tag{2.32}$$

which is consistent with the principle of energy equipartition:

$$\frac{1}{2} m \omega_m^2 \langle x^2 \rangle = \frac{1}{2} k_B T. \tag{2.33}$$

2.1.2.2 Periodically driven oscillations

In the case where a periodic force at (or close to) the mechanical resonance frequency, $F_d(t) = F_0 \cos(\omega t)$, is applied with an amplitude much larger than the typical thermal fluctuation amplitude, the system reaches a driven steady state [70, 93]. The amplitude of the Fourier component at ω is then given by:

$$|x(\omega)| = \frac{\frac{F_0}{2m}}{\sqrt{(\omega_m^2 - \omega^2)^2 + \gamma^2 \omega^2}}. \quad (2.34)$$

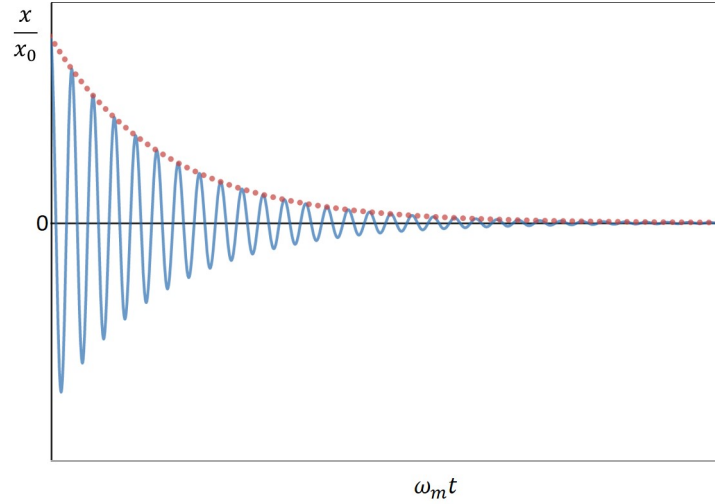


Figure 2.3: An example of an exponentially damped mechanical oscillation. The blue line shows damped oscillation of the resonator for $\omega_m/(2\pi) = 1$ MHz, $\gamma/(2\pi) = 6$ Hz and $\phi_0 = 0$. The red dot line is the envelope of damped function which represents the maximum amplitude of the oscillations.

By abruptly turning off the external force at a certain time, say $t = 0$, the system returns to thermal equilibrium on a time scale given by the inverse of the mechanical damping rate, as the energy of the driven motion slowly dissipates into the bath as a result of damping (see Fig. 2.3).

Solving Eq. (2.6) with $F_{th} = 0$, and $F_d(t) = F_0 \cos(\omega_m t) \Theta(-t)$, where $\Theta(t)$ is the Heaviside (step) function [$\Theta(t) = 1$ if $t \geq 0$, 0 otherwise], yields an amplitude of the form

$$x(t) = x_0 \cos(\omega_m t + \phi_0) e^{-\frac{\gamma(t-t_0)}{2}} = x_0 \cos(\omega_m t + \phi_0) e^{-\frac{\omega_m(t-t_0)}{2Q}}, \quad (2.35)$$

whose envelope exponentially decays with a time constant $2/\gamma = \omega_m/2Q$, that depends on the mechanical quality factor.

Monitoring the energy dissipation by perturbing the system and measuring the return to thermal equilibrium is the principle of ringdown spectroscopy, which will be discussed in Chap. 3.

2.1.2.3 Parametrically driven oscillator

A periodic modulation of a harmonic oscillator's frequency or damping at certain frequencies can cause a strong, "parametric" excitation of its motion [94–96]. Parametric resonances occur when the external periodic force (pump) has a frequency $\omega_p \simeq (2/n)\omega_m$, where n is a positive integer, and the most intense parametric excitation happens when $n = 1$ [97]. Indeed, while a "direct" driving at ω_m increases the amplitude linearly (Eq. (2.34)), a small parametric driving at $2\omega_m$ can lead to exponential amplification of the motion [98].

During the parametric excitation of driven oscillations, the amplitude of the oscillations around the equilibrium can be amplified or deamplified, depending on the relative phase between the driving force and the parametric force. Here, we focus on the parametric amplification of thermal fluctuations: there is no external drive force at the resonance frequency of the mechanical oscillator and we only have a sinusoidal frequency modulation due to an external force $F_p(t) = f_0 \sin(\omega_p t)$, where f_0 is the amplitude of applied force and ω_p is the pump frequency. Such parametric amplification dynamics can be described by the damped Mathieu equation [71, 96, 97, 99–101]:

$$\ddot{x}(t) + \gamma \dot{x}(t) + \omega_m^2 (1 + \xi \sin(\omega_p t)) x(t) = \frac{F_{th}}{m}, \quad (2.36)$$

where ξ is a constant proportional to modulation amplitude.

Let us take a pump frequency $\omega_p = 2(\omega_m + \delta)$ close to the second harmonic frequency and consider the high Q oscillator regime as before. It is convenient to introduce the slowly-varying envelope $A(t)$, such that

$$x(t) = \frac{1}{2} (A(t)e^{-i\omega_m t} + A^*(t)e^{i\omega_m t}) = \Re(A) \cos \omega_m t + \Im(A) \sin \omega_m t. \quad (2.37)$$

Neglecting the second-order derivatives of the $A(t)$ and $A^*(t)$ under the rotating wave approximation (RWA), Eq. (2.36) becomes:

$$\dot{A} + \frac{\gamma}{2} A + i\delta A - \frac{\omega_m \xi}{4} A^* = \tilde{F}, \quad (2.38)$$

where $\tilde{F} = F_{th} e^{i\omega_m t} / m\omega_m$. Fourier transforming Eq. (2.38) gives:

$$\left(\frac{\gamma}{2} + i\omega + i\delta\right)A(\omega) - \frac{\omega_m \xi}{4}A^* = \tilde{F}, \quad (2.39)$$

and its complex conjugate

$$\left(\frac{\gamma}{2} + i\omega + i\delta\right)A^* - \frac{\omega_m \xi}{4}A = \tilde{F}^*, \quad (2.40)$$

from which one can obtain

$$A(\omega) = \frac{(\Gamma + i\omega - i\delta)\tilde{F}(\omega) + \Gamma\epsilon\tilde{F}^*(\omega)}{(\Gamma + i\omega + i\delta)(\Gamma + i\omega - i\delta) - (\Gamma\epsilon)^2}, \quad (2.41)$$

$$A^*(\omega) = \frac{(\Gamma + i\omega + i\delta)\tilde{F}^*(\omega) + \Gamma\epsilon\tilde{F}(\omega)}{(\Gamma + i\omega + i\delta)(\Gamma + i\omega - i\delta) - (\Gamma\epsilon)^2}, \quad (2.42)$$

where

$$\epsilon = \frac{\omega_m \xi}{4(\gamma/2)} = \frac{Q\xi}{2} \quad \text{and} \quad \Gamma = \frac{\gamma}{2}. \quad (2.43)$$

In terms of the quadratures $X_1 = \Re(A)$ and $X_2 = \Im(A)$ and using Eqs. (2.39) and (2.40), one gets

$$\frac{\tilde{F} + \tilde{F}^*}{2} = (\Gamma + i\omega + i\delta - \epsilon\Gamma)X_1, \quad (2.44)$$

$$\frac{\tilde{F} - \tilde{F}^*}{2i} = (\Gamma + i\omega + i\delta - \epsilon\Gamma)X_2. \quad (2.45)$$

The noise spectrum of an arbitrary quadrature

$$X_\theta = X_1 \cos \theta + X_2 \sin \theta = \frac{\frac{\tilde{F} + \tilde{F}^*}{2}}{\Gamma(1 - \epsilon) + i\omega + i\delta} \cos \theta + \frac{\frac{\tilde{F} - \tilde{F}^*}{2i}}{\Gamma(1 + \epsilon) + i\omega + i\delta} \sin \theta \quad (2.46)$$

is given by:

$$\begin{aligned} S_{X_\theta}(\omega) &= \langle X_\theta(\omega)X_\theta(-\omega) \rangle \\ &= \frac{\frac{1}{2} \frac{S_{\tilde{F}}}{m^2 \omega_m^2}}{\Gamma^2(1 - \epsilon)^2 + \omega^2 + \delta^2} \cos^2 \theta + \frac{\frac{1}{2} \frac{S_{\tilde{F}}}{m^2 \omega_m^2}}{\Gamma^2(1 + \epsilon)^2 + \omega^2 + \delta^2} \sin^2 \theta, \end{aligned} \quad (2.47)$$

where we used the fact that

$$\langle F_{th}(\omega)F_{th}(\omega') \rangle = ak_B T m \gamma \delta(\omega + \omega'), \quad (2.48)$$

such that only $\langle \tilde{F}(\omega)\tilde{F}^*(-\omega) \rangle$ and $\langle \tilde{F}^*(\omega)\tilde{F}(-\omega) \rangle$ are non-zero and equal to $4k_B T\Gamma/m\omega_m^2$, where T is the thermal bath temperature. Furthermore, if one does not keep the track of the phase of the quadratures in the experiment, one observes an average noise spectrum which is equivalent to a random average over all the quadratures

$$\bar{S}(\omega) \equiv \bar{S}_{X_\theta}(\omega) = \frac{2k_B T\gamma}{m\omega_m^2} \frac{\Gamma^2(1+\epsilon^2) + \omega^2 + \delta^2}{[\Gamma^2(1-\epsilon^2) + \delta^2 - \omega^2]^2 + 4\Gamma^2\omega^2}. \quad (2.49)$$

At the parametric resonance ($\delta = 0$), the average noise spectrum can be written as

$$\bar{S}(\omega) \equiv \bar{S}_{X_\theta}(\omega) = \frac{k_B T\gamma}{m\omega_m^2} \left[\frac{1}{\Gamma^2(1-\epsilon)^2 + \omega^2} + \frac{1}{\Gamma^2(1+\epsilon)^2 + \omega^2} \right], \quad (2.50)$$

which, for this choice of phase, is the sum of two Lorentzians with HWHMs $\Gamma(1-\epsilon)$ and $\Gamma(1+\epsilon)$, respectively. If $\epsilon \rightarrow 0$ or $\epsilon \rightarrow 1$, the average spectrum is close to Lorentzian. Lorentzian spectrum with the narrowed width $\Gamma(1-\epsilon)$ corresponds to the noise spectrum of the amplified X_1 quadrature and the Lorentzian with the broadened width $\Gamma(1+\epsilon)$ to that of the deamplified X_2 quadrature.

The parametric oscillation threshold is obtained when the "linewidth" of the first Lorentzian goes to 0, i.e: $\epsilon_{threshold} = 1$, i.e $\xi_{threshold} = \frac{1}{2Q}$ and at the parametric threshold, the linewidth of the noise spectrum diverges (in the absence of nonlinearities). In order to reach the parametric oscillation threshold the amplitude of the parametric modulation has to be large enough (as compared to the damping).

As we can see in Fig. 2.4, for low values of ϵ (e.g. 0.1 in Fig. 2.4a), we get a Lorentzian noise spectrum due to the fact that the HWHM of both quadratures is almost the same and is given by γ . For very high ϵ (e.g. 0.9 in Fig. 2.4c), the HWHM of the average spectrum is dominated by the amplified quadrature spectrum HWHM and the form of the function is again expected to be quite like a Lorentzian, whereas in case of $0 < \epsilon < 1$ (e.g. $\epsilon = 0.5$ in Fig. 2.4b), the function is less Lorentzian.

The variance of the amplitude –and consequently the average energy in the mode $\bar{E} = \frac{1}{2}m\omega_m^2\langle x^2 \rangle$ – can be obtained by

$$\Delta x^2 = \langle x^2 \rangle = \int_0^\infty \bar{S}(\omega) \frac{d\omega}{2\pi} = \frac{k_B T}{m\omega_m^2} \frac{1}{1 - \epsilon^2/(1 + \delta^2/\Gamma^2)}. \quad (2.51)$$

In the absence of parametric modulation, the average energy is $\bar{E}_0 = \frac{1}{2}k_B T$, whereas, in the presence of parametric modulation, the average energy increases as $1/(1 - \epsilon^2)$ and diverges at the threshold. For a nonzero pump detuning, the gain in energy is reduced following Eq. (2.51) and the parametric resonance linewidth

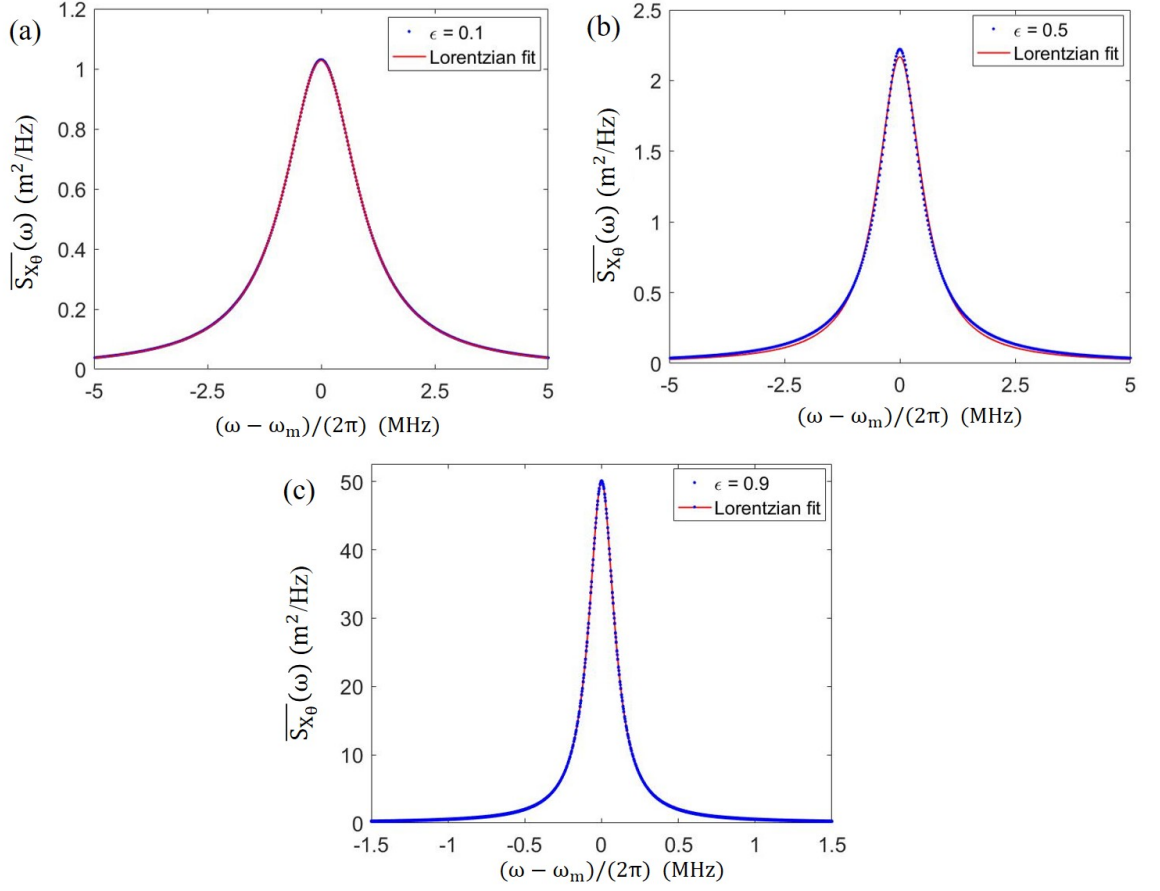


Figure 2.4: Noise spectra of mechanical oscillator with $\gamma/(2\pi) = 1$ Hz and the resonance frequency at $\omega_m/(2\pi) = 1$ MHz for (a) $\epsilon = 0.1$, (b) $\epsilon = 0.5$ and (c) $\epsilon = 0.9$. Red line represents a Lorentzian fit to the parametric noise spectrum.

depends on both Γ and ϵ .

In a linear parametric excitation, the average energy increases and in principle, it diverges at the threshold. In practice, nonlinearities prevents the linewidth to be infinitely narrow and self-oscillations with finite amplitudes are observed above the threshold.

2.1.2.4 Duffing oscillator

Nonlinear behavior can also be exhibited by oscillators driven to high amplitudes. A common case is the case of an oscillator experiencing a nonlinear (e.g. cubic) restoring force in the displacement, which is also referred to as the Duffing oscillator model. In this model the equation of motion (modified by introducing a cubic

nonlinearity in the displacement) according to [102, 103] is:

$$m\ddot{x} + m\gamma\dot{x} + m\omega_m^2(x + \beta x^3) = 0 \quad (2.52)$$

where m and β are the mass and Duffing nonlinearity coefficient of the system, respectively.

In the presence of an external sinusoidal force $F_d = F_\omega \cos(\omega t)$ applied to the system, the forced Duffing equation can also be used to model the forcing of the damped nonlinear elastic structure:

$$\ddot{x} + \gamma\dot{x} + \omega_m^2(x + \beta x^3) = \frac{F_\omega}{m} \cos(\omega t), \quad (2.53)$$

where the sign of β determines whether the nonlinear force becomes more restoring as the amplitude increases (spring hardening) or, on the contrary, less restoring (spring softening).

For a small nonlinearity, the amplitude of the Fourier component at ω can be approximated by [102]:

$$|x(\omega)| = \frac{F_\omega/2m}{\sqrt{(\omega_m^2(1 + \frac{3}{4}\beta|x(\omega)|^2) - \omega^2)^2 + \gamma^2\omega^2}}. \quad (2.54)$$

The results of Eq. (2.54) for $\frac{3}{4}\beta = \pm \frac{1}{x_0^2} \times 10^{-12}$ with different F_ω s for a damped oscillator with $\gamma = 10^{-6}\omega_m$ are shown in Fig. 2.5. One observes asymmetric profiles, distorted towards lower (spring softening) or higher (spring hardening) frequencies. As can be seen, when $\beta \neq 0$ the maximum amplitude no longer happens at ω_m and is shifted due to the nonlinear frequency shift. When this nonlinear shift is at the order of the linewidth, bistability may occur with an hysteresis behavior depending on the direction of the scanning frequency of the force.

Figure 2.6 illustrates this behavior for a Duffing oscillator with $\beta > 0$ by scanning the frequency around ω_m . By moving towards the higher frequencies, after reaching the maximum value of the amplitude (1), a sudden drop happens (2) and going to higher frequencies no longer increases the amplitude. When going backward in frequencies, the amplitude grows (3), jumps to a higher amplitude (4) which is not the same as before. [102]

Interestingly, Eq. (2.54) can also be interpreted as describing the amplitude of an oscillating solution of the form $\cos(\omega t + \phi)$. It means that the term in x^3 in (2.54) can be seen as an effective parametric modulation in the Mathieu equation

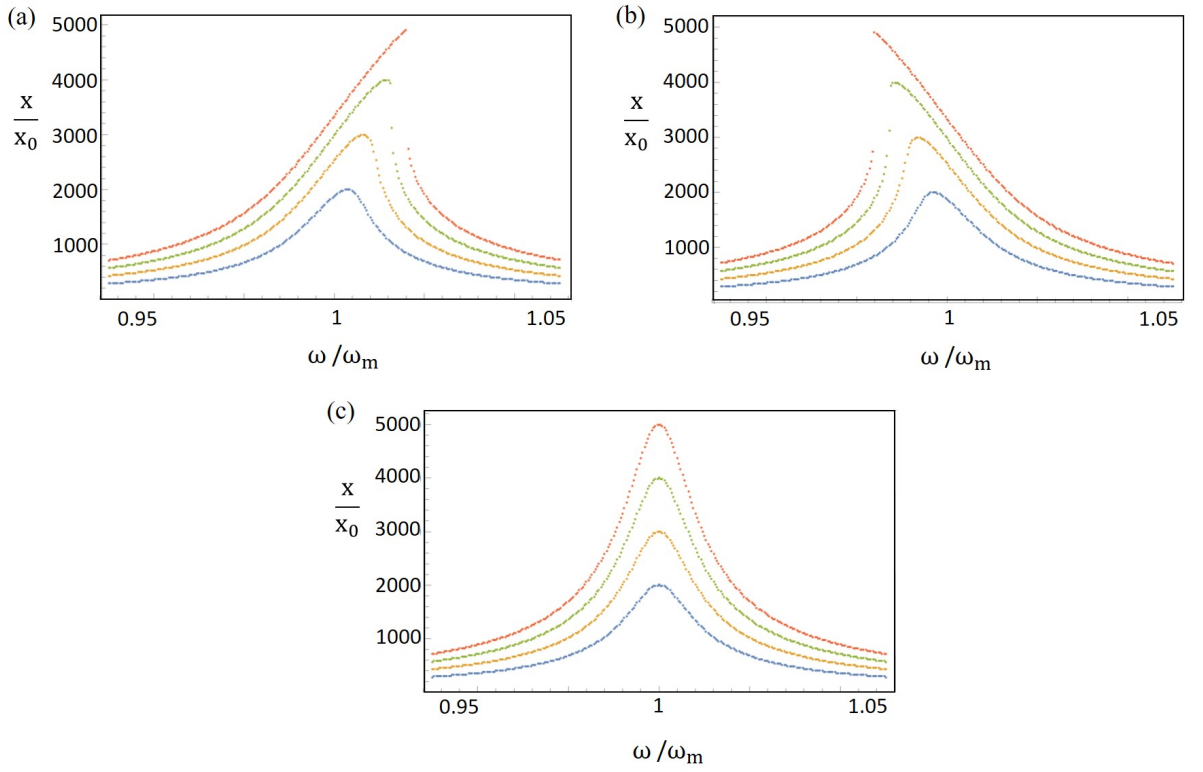


Figure 2.5: Amplitude-frequency curves of Eq. (2.54) for $\omega_m/(2\pi) = 1$ MHz and $\gamma = 10^{-6}\omega_m$ with (a) $\frac{3}{4}\beta = +\frac{1}{x_0^2} \times 10^{-12}$, (b) $\frac{3}{4}\beta = -\frac{1}{x_0^2} \times 10^{-12}$ and (c) $\beta = 0$, for different F_ω s in red (5×10^5 kgHz²), green (4×10^5 kgHz²), orange (3×10^5 kgHz²) and blue (2×10^5 kgHz²).

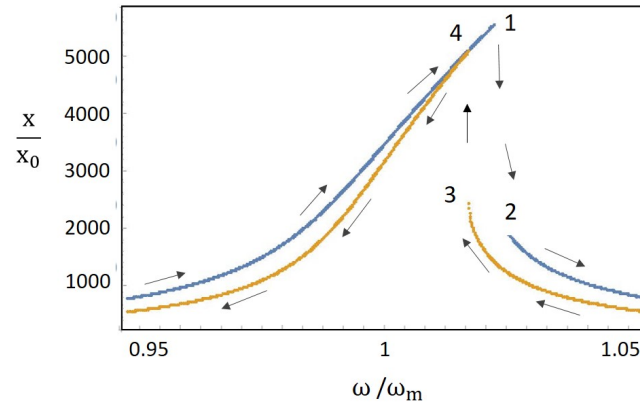


Figure 2.6: An example of a hysteresis behaviour of amplitude-frequency curve of Eq. (2.54) for $\omega_m/(2\pi) = 1$ MHz, $\gamma = 10^{-6}\omega_m$, $F_\omega = 5 \times 10^5$ kgHz² and $\beta = 10^{-12}/x_0$.

$\cos(2\omega t)x$. The mathematical connection between the forced Duffing equation and the damped Mathieu equation is discussed in [102].

2.1.3 Coupled oscillators

We have so far discussed the dynamics of a single isolated mechanical mode. However, a mechanical resonator typically possesses many vibrational modes. Or the modes of distinct mechanical resonators can also be coupled together, as we will see several examples in the next chapters. In order to discuss in a simple fashion generic features of coupled-oscillator modes, we consider here two mechanical oscillators connected to one another by a spring (see Fig. 2.7). The bare spring constants are denoted by κ_1 and κ_2 and the spring constant connecting the two masses is denoted by κ_{12} . Assuming a linear harmonic response, the restoring forces on each mass are given by:

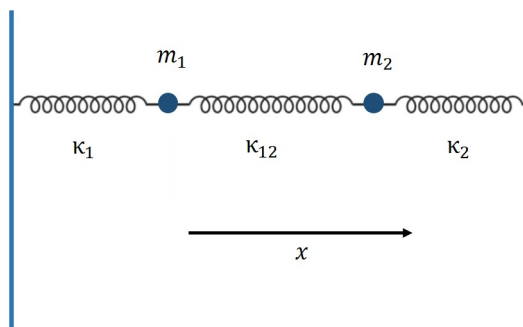


Figure 2.7: Schematic picture of a two linearly coupled harmonic oscillators with masses m_1 and m_2 attached to two springs with the spring constants κ_1 and κ_2 . The third spring with the spring constant κ_{12} represents the linear coupling between them.

$$F_1 = -\kappa_1 x_1 + \kappa_{12}(x_2 - x_1), \quad (2.55)$$

$$F_2 = -\kappa_2 x_2 + \kappa_{12}(x_1 - x_2) \quad (2.56)$$

which give the equations of motion:

$$m_1 \ddot{x}_1 + (\kappa_1 + \kappa_{12})x_1 - \kappa_{12}x_2 = 0, \quad (2.57)$$

$$m_2 \ddot{x}_2 + (\kappa_2 + \kappa_{12})x_2 - \kappa_{12}x_1 = 0. \quad (2.58)$$

Assuming the same mass ($m_1 = m_2 = m$) and adding damping and the thermal fluctuation forces, the equations of motion become:

$$\ddot{x}_1 + \gamma_1 \dot{x}_1 + \omega_1^2 x_1 = \kappa(x_2 - x_1) + F_{th1}, \quad (2.59)$$

$$\ddot{x}_2 + \gamma_2 \dot{x}_2 + \omega_2^2 x_2 = \kappa(x_1 - x_2) + F_{th2}, \quad (2.60)$$

where $\kappa = \kappa_{12}/m$ is the intermode spring constant due to the coupling, $F_{th1,2}$ are the thermal noise forces (divided by the mode effective mass), $\gamma_{1,2}$ and $\omega_{1,2} = \sqrt{\kappa_{1,2}/m}$ are the mechanical damping rates and resonance frequencies of each mode, respectively.

In the presence of the coupling, Fourier transforming of Eqs. (2.59) and (2.60) gives:

$$[-\omega^2 - i\omega\gamma_1 + \omega_1^2]x_1(\omega) = \kappa(x_2(\omega) - x_1(\omega)) + F_{th1}(\omega), \quad (2.61)$$

$$[-\omega^2 - i\omega\gamma_2 + \omega_2^2]x_2(\omega) = \kappa(x_1(\omega) - x_2(\omega)) + F_{th2}(\omega). \quad (2.62)$$

In the good oscillator limit, one obtains the frequencies of these normal modes as:

$$\omega_{\pm} = [\omega_0^2 + \delta^2 + 2\eta\omega_0 \pm 2\omega_0\sqrt{\delta^2 + \eta^2}]^{1/2} \quad (2.63)$$

where

$$\omega_0 = (\omega_1 + \omega_2)/2, \quad \delta = (\omega_1 - \omega_2)/2, \quad \eta = \frac{\kappa}{2\omega_0}, \quad (2.64)$$

and η is the intermode coupling constant. The dynamics of the coupled modes and thereby their thermal noise spectra depend on the relative strength of the intermode coupling, the frequency separation between the modes and their respective dampings.

Very non-degenerate frequency modes behave essentially independently of each other and their mechanical resonance frequencies are both shifted by a nearly equal amount when the coupling η is increased. For nearly degenerate frequency modes, however, hybridization occurs and normal "bright" and "dark" modes have to be defined [85], due to the intermode coupling. For $\eta \ll \delta$ (like the uncoupled oscillators), changes in frequencies happen independently for each mode whereas the increase in η leads to the mode hybridizing and when $\eta \gg \delta$, the bright mode frequency keeps increasing while the dark mode frequency becomes constant.

Figure 2.8 illustrates the variations of the frequencies and frequency shifts, $\delta\omega_{\pm} = \omega_{\pm} - (\omega_0 \pm \delta)$, as a function of η in the case of a positive $\delta = 0.005\omega_0$. Two regimes can be distinguished:

- When $\eta \ll \delta$, the dynamics of both modes are essentially independent and they experience the same positive frequency shift η . When η becomes of the order of δ , the bare modes hybridize.

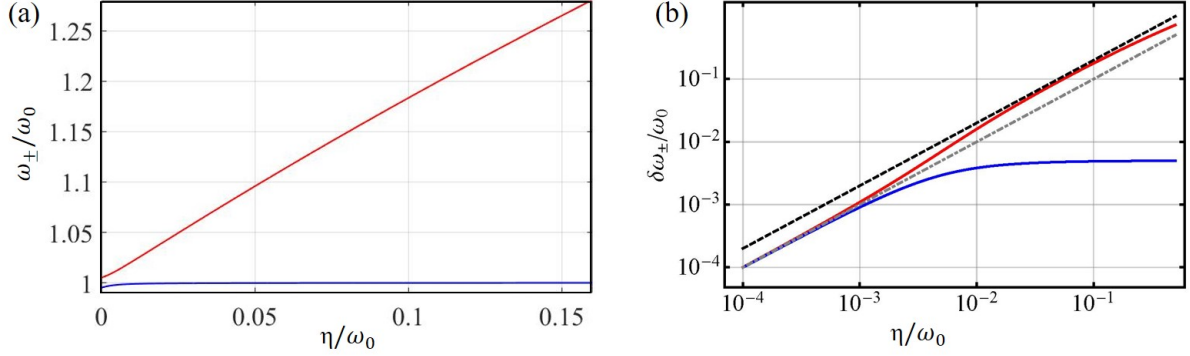


Figure 2.8: Normal mode (a) frequencies and (b) frequency shifts [86] as a function of coupling (in units of ω_0) for $\delta = 0.005\omega_0$. The plain red lines are ω_+ and $\delta\omega_+$ and the plain blue lines correspond to ω_- and $\delta\omega_-$. The dot-dashed gray and the dashed black lines show linear shifts equal to η and 2η , respectively.

- When $\eta \gg \delta$, the bright mode –corresponding to the relative motion of the membranes– experiences a doubled frequency shift, 2η , while the dark mode –corresponding to their center-of-mass motion– no longer experiences any frequency shift and converges to the mean of the bare frequencies ω_0 .

At very large couplings the bright mode frequency shift no longer scales linearly with η , but rather as $\sqrt{\eta}$. When δ is negative the roles of ω_+ and ω_- are reversed.

Alternatively, one can look at the evolution of the normal mode frequencies when the coupling η is fixed and the frequency separation δ is varied. Figure 2.9 shows this evolution for a zero and nonzero coupling. When $\delta = 0$, i.e. at the uncoupled mode frequency degeneracy, an avoided crossing can be observed, the splitting between the frequencies giving a measure of the coupling η . When this splitting becomes of the order or larger than the individual linewidths $\gamma_{1,2}$, the oscillators are said to be strongly coupled.

In the experiments that we will discuss in the next chapters, the dynamics of the membrane vibrational modes are monitored via their noise spectra. The noise spectrum of x_1 and x_2 can be readily obtained from Eqs. (2.61) and (2.62), which give:

$$x_1(\omega) = \frac{\chi_2(\omega)F_{th1}(\omega) + \kappa F_{th2}(\omega)}{\chi_1(\omega)\chi_2(\omega) - \kappa^2}, \quad (2.65)$$

$$x_2(\omega) = \frac{\chi_1(\omega)F_{th2}(\omega) + \kappa F_{th1}(\omega)}{\chi_2(\omega)\chi_1(\omega) - \kappa^2}, \quad (2.66)$$

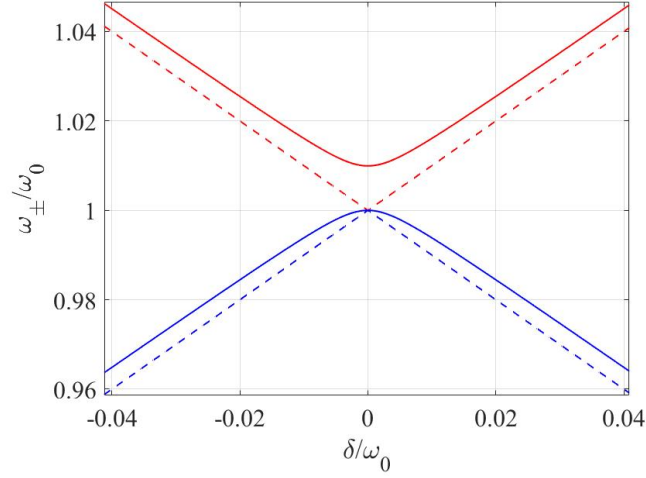


Figure 2.9: Frequencies for two coupled modes as a function of δ (in units of ω_0) with $\eta/(2\pi) = 0.05$ Hz in plain lines which shows the increase of avoided crossing point as a result of the coupling strength and two uncoupled modes $\eta = 0$ in dashed lines.

where

$$\chi_\alpha(\omega) = (-\omega^2 - i\omega\gamma_\alpha + \omega_\alpha^2) + \kappa \quad (\alpha = 1, 2). \quad (2.67)$$

Anticipating on the following, the interferometric signal typically provides the noise spectrum of a combination of x_1 and x_2 , e.g. $x_1 - x_2$. In this case, one gets:

$$S_{x_1-x_2}(\omega) = \frac{|\chi_2(\omega) - \kappa|^2 S_{F_{th1}}(\omega) + |\chi_1(\omega) - \kappa|^2 S_{F_{th2}}(\omega)}{|\chi_1\chi_2 - \kappa^2|^2}, \quad (2.68)$$

which, in the absence of coupling ($\kappa = 0$), would be reduced to the sum of two independent thermal noise spectra.

In Fig. 2.10, the result of Eq. (2.68) is presented around $\omega_0/(2\pi) = 1$ MHz for different values of δ for two modes with $\gamma_1/(2\pi) = 8$ Hz and $\gamma_2/(2\pi) = 4$ Hz, respectively which means $\gamma_2 = 2\gamma_1$. In the absence of coupling (Fig. 2.10a), the amplitude of the noise simply adds up at the crossing point, whereas, in case of non-zero coupling (compare κ to the γ s), the correlations between the modes strongly alter the shape of the noise spectrum in the vicinity of the degeneracy point. In case of having a coupling, $\eta/(2\pi) = 0.5$ Hz, Fig. 2.10b shows that the combination of both modes is no longer the summation of amplitudes at the crossing point.

To conclude this section, we have introduced the basic elements that we will be using in the next chapters to describe the dynamics and noise properties of the

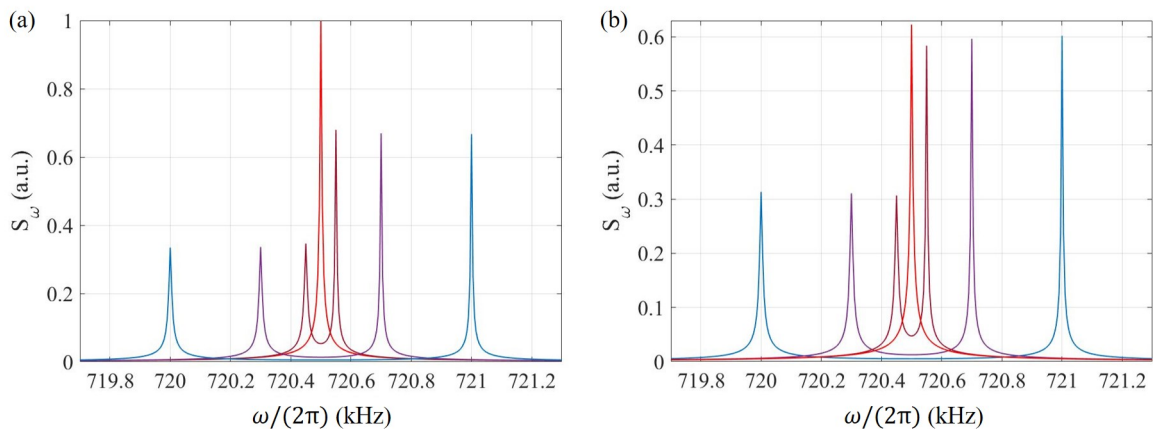


Figure 2.10: Example of the noise spectrum of two mechanical modes with resonance frequencies $\omega_1 = \omega_0 - \delta$ and $\omega_2 = \omega_0 + \delta$ with $\gamma_1/(2\pi) = 8$ Hz and $\gamma_2/(2\pi) = 4$ Hz, respectively, while $\omega_0/(2\pi) = 720.5$ kHz. (a) In the absence of coupling, $\eta = 0$ and (b) while coupling is present, $\eta/(2\pi) = 0.5$ Hz.

vibrational modes of the membrane resonators. We now turn to the description of their optical properties.

2.2 Optics

For most of the experiments discussed in this thesis, the optical properties of the resonators –dielectric slabs or parallel assembly of slabs– are well-described in the frame of a one-dimensional scattering model, in which the light fields impinging on the resonators can be considered as plane waves.

2.2.1 One-dimensional transfer matrix model

We consider the propagation of plane waves in a lossless one-dimensional dielectric along z -direction, which is described by Maxwell's equations:

$$\begin{aligned}
 \nabla \times \vec{E} &= -\mu \frac{\partial \vec{H}}{\partial t}, \\
 \nabla \times \vec{H} &= -\epsilon \frac{\partial \vec{E}}{\partial t}, \\
 \nabla \cdot \vec{E} &= 0, \\
 \nabla \cdot \vec{H} &= 0,
 \end{aligned} \tag{2.69}$$

where \vec{E} and \vec{H} are the electric and magnetic fields, ϵ and μ are the electric

permittivity and magnetic permeability, respectively. The latter are related to the impedance η and the speed of light in vacuum c by:

$$\epsilon = \frac{1}{\eta c}, \quad \mu = \frac{\eta}{c}, \quad c = \frac{1}{\sqrt{\mu\eta}}, \quad \eta = \sqrt{\frac{\mu}{\epsilon}}. \quad (2.70)$$

The fields can be decomposed in forward ("+" subscript) and backward ("-") subscript) propagating fields:

$$\begin{aligned} \vec{E}(z, t) &= \vec{E}_+(z, t) + \vec{E}_-(z, t), \\ \vec{H}(z, t) &= -\frac{1}{\eta} \cdot \hat{z} \times [\vec{E}_+(z, t) - \vec{E}_-(z, t)] \end{aligned} \quad (2.71)$$

or, equivalently,:

$$\begin{aligned} \vec{E}_+ &= \frac{1}{2}(\vec{E} + \eta\vec{H} \times z), \\ \vec{E}_- &= \frac{1}{2}(\vec{E} - \eta\vec{H} \times z). \end{aligned} \quad (2.72)$$

At a planar interface between two dielectric media with refractive indices n and n' (Fig. 2.11), the Fresnel coefficients relate the amplitudes of the backward- and forward-propagating fields on each side of the interface:

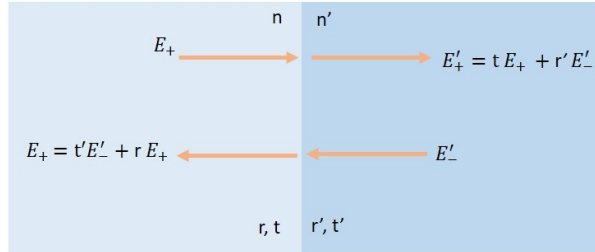


Figure 2.11: Schematic picture of a dielectric interface between two mediums with different refractive indices n, n' and Fresnel reflection and transmission coefficients r, r' and t, t' , respectively.

$$\begin{aligned} r &= \frac{n - n'}{n + n'}, & r' &= \frac{n' - n}{n' + n}, \\ t &= \frac{2n}{n + n'}, & t' &= \frac{2n'}{n' + n}. \end{aligned} \quad (2.73)$$

In order to describe the propagation of light through a single dielectric slab with index n (and surrounded by vacuum), as depicted in Fig. 2.12, it is convenient to model the transmission of such system by using the transfer matrix, which generally relates the amplitudes of the backward-propagating (A and C) and

forward-propagating (B and D) plane waves [104] incident on the right and the left of a one-dimensional scatterer in Fig. 2.13.

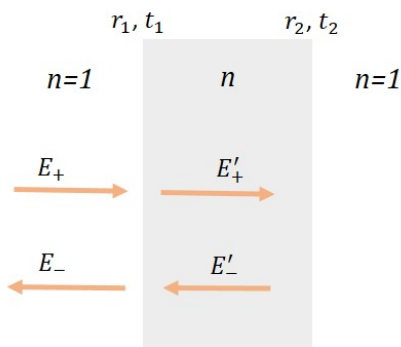


Figure 2.12: Schematic picture of a single dielectric slab with the refractive index n and vacuum/dielectric interfaces with r_1, r_2 and t_1, t_2 as the reflection and transmission coefficients.

$$\begin{bmatrix} A \\ B \end{bmatrix} = M \begin{bmatrix} C \\ D \end{bmatrix} = \begin{bmatrix} m_{1,1} & m_{1,2} \\ m_{2,1} & m_{2,2} \end{bmatrix} \begin{bmatrix} C \\ D \end{bmatrix}. \quad (2.74)$$

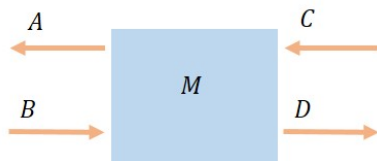


Figure 2.13: Schematic picture of propagating waves on each side of a one-dimensional scatterer described by the transfer matrix M .

The transfer matrices for the interfaces vacuum/dielectric and dielectric/vacuum are given by:

$$M_{int,i} = \frac{1}{t_i} \begin{bmatrix} 1 & r_i \\ r_i & 1 \end{bmatrix}, \quad (i = 1, 2) \quad (2.75)$$

where the Fresnel coefficients for the reflectivity (r_1 and r_2) and the transmittivity (t_1 and t_2) at the normal incidence at the left and right vacuum/dielectric interfaces are given by:

$$r_1 = -r_2 = \frac{1-n}{1+n} = r, \quad t_1 = \frac{2}{1+n}, \quad t_2 = \frac{2n}{1+n}. \quad (2.76)$$

Moreover, the propagation of monochromatic light with a wavelength λ over a distance d in a medium with refractive index n can be described by the transfer matrix:

$$M_f(nd) = \begin{bmatrix} e^{\frac{i2\pi nd}{\lambda}} & 0 \\ 0 & e^{-\frac{i2\pi nd}{\lambda}} \end{bmatrix}. \quad (2.77)$$

Using the transfer matrices Eqs. (2.75) and (2.77) one can analyze the propagation through a succession of media by simply multiplying the relevant transfer matrices together, as we will now illustrate in the case of membranes and membrane arrays.

2.2.2 Single membrane

The single membranes considered in this work can be assumed to be a dielectric slab with thickness l and refractive index n , the absorption in the considered wavelength range being negligible for the purpose of this thesis. Using the transfer matrices introduced previously, the transfer matrix for a single membrane is given by:

$$M_m = M_{int,1} \cdot M_f(nl) \cdot M_{int,2}. \quad (2.78)$$

For light incident from the left-hand side, complex transmissivity and reflectivity of a system with transfer matrix M are given by:

$$t_m = \frac{1}{m_{2,2}}, \quad r_m = \frac{m_{1,2}}{m_{2,2}}. \quad (2.79)$$

This leads to the membrane reflectivity and transmittivity coefficients [21]:

$$r_m = \frac{r(1 - \exp(2i\theta))}{1 - r^2 \exp(2i\theta)}, \quad t_m = \frac{t_1 t_2 \exp(2i\theta)}{1 - r^2 \exp(2i\theta)}, \quad \text{where } \theta = \frac{2\pi nl}{\lambda}. \quad (2.80)$$

Thereby, the transmission for a single membrane is:

$$T_{single} = |t_m|^2 = \left| \frac{t_1 t_2}{1 - r^2 \exp(2i\theta)} \right|^2, \quad (2.81)$$

which is that of a linear Fabry Perot etalon (Airy function). Internal resonances (perfect transmission) occur when $\lambda = \frac{2nl}{p}$ where p is an integer number. The red line in Fig. 2.14 shows an example of transmission of a single membrane with $l = 100$ nm and $n = 2$ over the wavelength range 200-1000 nm for which the first internal resonance occurs at $\lambda = 400$ nm.

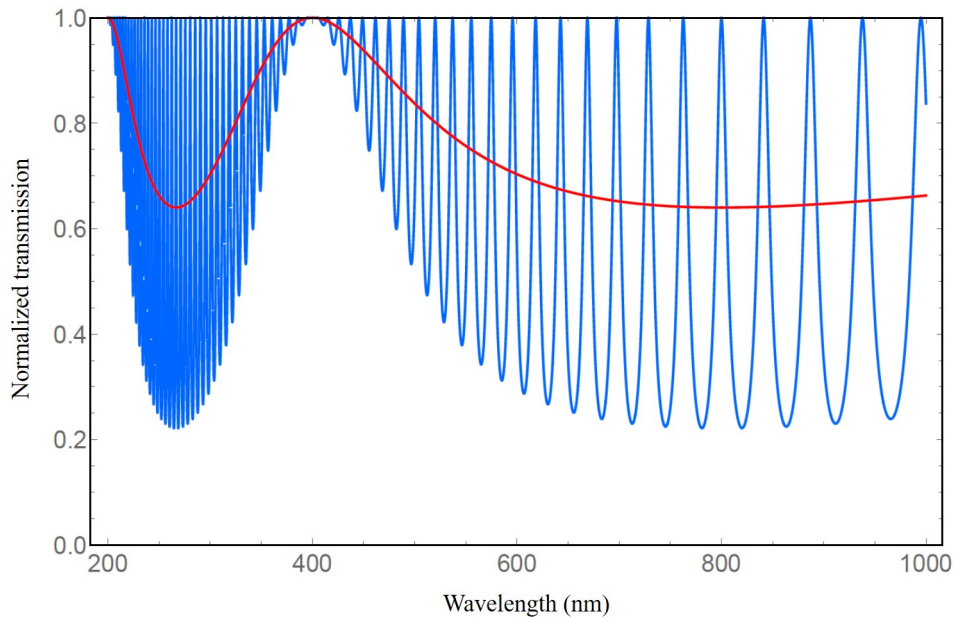


Figure 2.14: Transmission spectrum of a single membrane (red) and a double-membrane array (blue). The membranes have both $l = 100$ nm and $n = 2$, and the intermembrane distance in the array is $d = 8$ μm .

2.2.3 Double-membrane array

We now consider a double-membrane array, consisting of two parallel, identical membranes separated by a distance d , as depicted in Fig. 2.15.

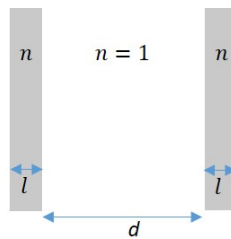


Figure 2.15: Schematic picture of a double-membrane array with identical parallel membranes. l and n are the thickness and refractive index of the membranes, respectively, and d is the intermembrane separation in vacuum.

The double-membrane transfer matrix is given by:

$$M_{double} = M_m \cdot M_f(d) \cdot M_m, \quad (2.82)$$

which gives a transmission ($\phi = \frac{2\pi d}{\lambda}$):

$$T_{double}(\lambda) = \left| \frac{t_m^2}{1 - r_m^2 \exp(2i\phi)} \right|^2, \quad (2.83)$$

that can also be rewritten as a canonical linear Fabry Perot Airy function:

$$T_{double}(\lambda) = \frac{1}{1 + F \sin^2(\phi + \theta + \psi)}, \quad (2.84)$$

where F is the factor of finesse

$$F = \frac{4|r_m|^2}{(1 - |r_m|^2)^2}, \quad (2.85)$$

and

$$\tan 2\psi = \frac{r^2 \sin 4\theta - 2r^2 \sin 2\theta}{1 - 2r^2 \cos 2\theta + r^4 \cos 4\theta}. \quad (2.86)$$

The final expression in Eq. (2.84) is the standard Airy function for a linear Fabry Perot cavity with two identical mirrors in which the factors θ and ψ account for the thickness of the mirrors. Note that the Fabry Perot fringes, whose spacing is determined by d , are modulated by the wavelength-dependent single slab transmission (determined by l). The transmission spectrum of an 8 μm -long double-membrane array is shown in Fig 2.14 as an example.

2.3 Optomechanics

The membrane resonators being flexible mirrors, their vibrations can be naturally investigated by optical interferometry. The description of how the mechanics affect the transmission of light impinging on the membranes follows then naturally from the two previous sections. To illustrate the optical interferometry technique, we consider a low-finesse Fabry Perot cavity, as shown in Fig. 2.16 which consists in a beamsplitter (BS) with reflectivity r_1 and a membrane with reflectivity r_m separated by an equilibrium distance L . The amplitude of the vibrating membrane around its equilibrium position is $x(t)$ and gives the changes in the length of interferometer. The cavity is exposed to a monochromatic laser beam with the frequency ω_L whose transmitted intensity can be measured with a photodetector.

The transmission of this interferometer is sensitive to its length changes:

$$T = \frac{T_{max}}{1 + F \sin^2\left(\frac{2\pi(L+x(t))}{\lambda}\right)}, \quad T_{max} = \left(\frac{t_m t_1}{1 - r_m r_1}\right)^2, \quad (2.87)$$

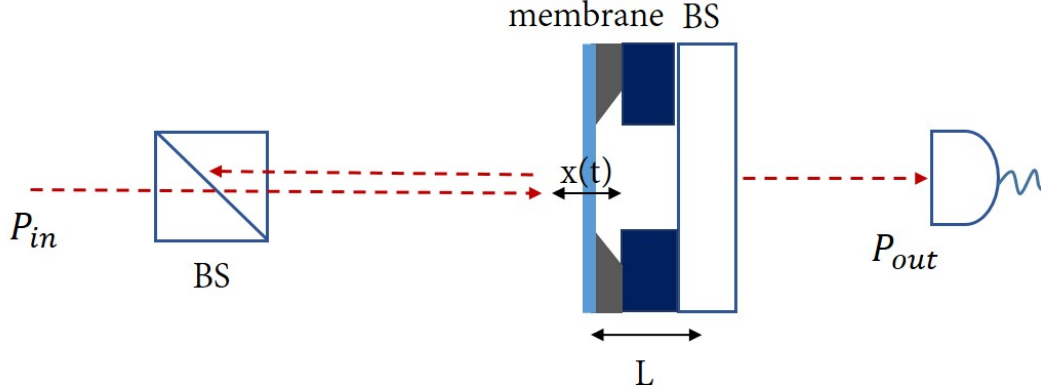


Figure 2.16: Schematic picture of a low-finesse Fabry Perot interferometer with a suspended membrane as its movable end mirror and a 50:50 beamsplitter (BS) as the other end mirror. L is the cavity length at equilibrium, $x(t)$ is the displacement of the membrane. A monochromatic laser beam is focused on the interferometer and the amplitude of the transmitted and/or reflected field is monitored on a photodetector.

where the factor of finesse F of this lossless asymmetric cavity, in this case, is:

$$F = \frac{4r_m r_1}{(1 - r_m r_1)^2}. \quad (2.88)$$

The steady-state transmitted power is given by [70, 105]:

$$P_{out} = \frac{T_{max}}{1 + F^2 \sin^2(2\pi L/\lambda)} \times P_{in}, \quad (2.89)$$

which can be used to calculate the expected value for the maximum transmission T_{max} and the visibility of the interference fringes which is defined as:

$$V(F) = \frac{P_{max} - P_{min}}{P_{max} + P_{min}} = \frac{2F}{2F + 1}. \quad (2.90)$$

In order to be sensitive to small displacements, we monitor the power transmitted from the interferometer at the mid-slope of the transmission by changing the wavelength of laser (Fig. 2.17).

The length-to-power transduction is maximum at the position half-way between the maximum and minimum value of the transmission and given by [70]:

$$\frac{dP_{out}}{dL} = -P_{out} \times \frac{2\pi\sqrt{F}}{\lambda} C(F) \quad (2.91)$$

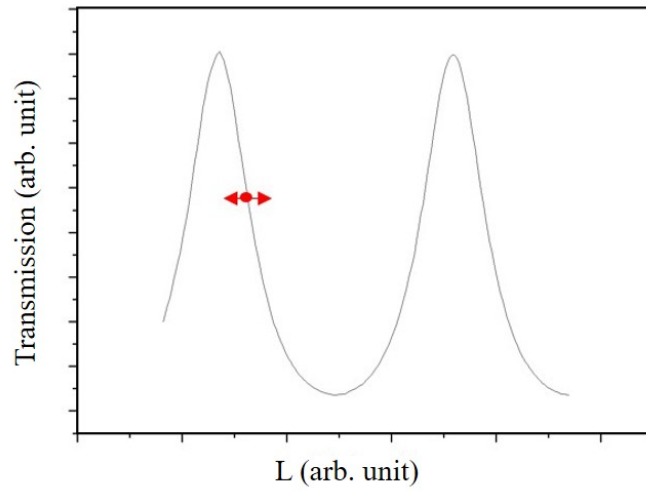


Figure 2.17: Schematic transmission plot in arbitrary unit.

where P_{out} is the average transmitted power at the half-way and $C(F)$ is the correction factor and is calculated by:

$$C(F) = \sqrt{\frac{F}{1+F}}. \quad (2.92)$$

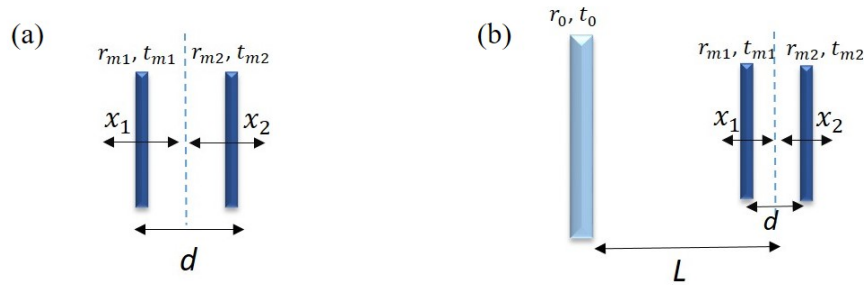


Figure 2.18: Schematic picture of (a) the interferometer represented by a double-membrane array and (b) the three-mirror interferometer consisting of the two movable membranes and one fixed BS.

The same analysis holds in principle for a double-membrane array, which constitutes in itself a linear Fabry Perot interferometer with length d . The only difference is that both end mirrors' positions are now fluctuating and can be monitored on the transmission signal. Once the array is assembled, d is however fixed. If d is not too small (Fig. 2.18a), it may be possible, given the available tuning range of the laser, to operate at midfringe and obtain an optimal displacement sensitivity, which

is, ideally, equal for each membrane. If d is too small, one can still use the previous interferometer with the beamsplitter in Fig. 2.18b, where the double-membrane array now constitutes the end mirror and the interferometer length L is tuned as previously. The variations of the displacement sensitivity with L and λ are then more complex in this three-mirror system and can in principle be analyzed as in [106]. In practice, as we will see in the next chapter, one varies the interferometer length and the laser wavelength so as to optimize the displacement sensitivity of one and/or the other membrane modes.

3

Membrane array assembly and characterization

Before we discuss the applications of SiN membrane arrays for pressure sensing and for electro-optomechanics in the next chapters, this chapter introduces their fabrication process and explains the techniques for characterizing their optical and mechanical properties. The chapter begins with an overview of the commercial silicon nitride membranes used (Sec. 3.1) and illustrates the geometries used to assemble the double-membrane array. A brief review of the work carried out by Bhagya Nair in her PhD thesis [84] on the first generation of arrays is given in Sec. 3.2 and the challenges for achieving high parallelism are discussed. The new experimental setup to improve the assembly process is introduced in Sec. 3.3 which also presents examples of the measured transmission spectra of different membrane arrays under monochromatic or broadband illumination. The interferometric displacement setup used to characterize the mechanical properties of the resonators is introduced in Sec. 3.3.4.

3.1 Si_3N_4 membrane arrays

The resonators used in this project are stoichiometric Si_3N_4 membranes bought from a MEMS company, NORCADA, Edmonton (Canada) [66] which produces commercial membranes in various chip sizes (Si frame), membrane sizes and thicknesses. These are thin high tensile stress (\approx GPa) membranes fabricated by Low Pressure

Chemical Vapour Deposition (LPCVD) of SiN layer on a Si wafer. To define the membrane window in this technique, deposition of electron beam resist and electron beam lithography (EBL) were performed and followed by further development and etching to create the suspended SiN membrane [70]. These membranes typically have $\sim\text{mm}^2$ area, thickness $\approx 50 - 100$ nm and effective mass \approx ng. In all the studies in this thesis, the chips were made of stoichiometric Si_3N_4 films with membrane size $a = 0.5$ mm and thickness $l = 100$ nm suspended on the Si frame with size $a_f = 5$ mm. Frame thicknesses l_f of either 200 or 500 μm were used.

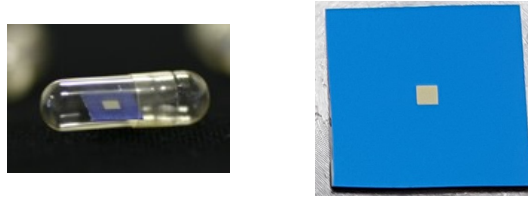


Figure 3.1: Pictures of commercial SiN membrane on Si chip.

To form a double-membrane array, these could be positioned parallel to each other by using two geometries: front-to-front or back-to-front, as shown in Fig. 3.2.

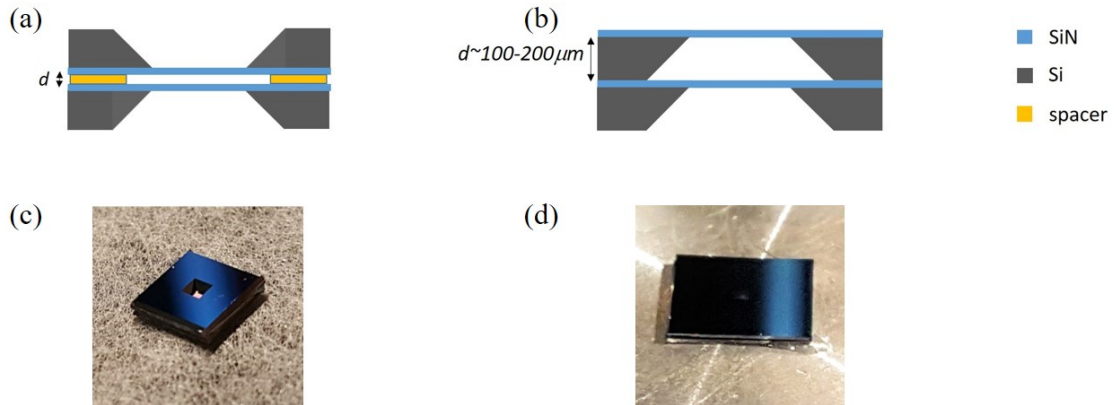


Figure 3.2: Schematic pictures of (a) front-to-front and (b) back-to-front geometries for Si_3N_4 double-membrane arrays and d is the intermembrane separation. Bottom pictures of double-membrane arrays made in (c) front-to-front and (d) back-to-front geometries.

In the front-to-front geometry, one of the chips has a spacer deposited on top of the SiN film. This spacer can have been deposited by NORCADA during a custom

fabrication process or created post-fabrication in the Interdisciplinary Nanoscience Center (iNANO) cleanroom by depositing metal (e.g. Al) or UV resist on one of the standard chips, as it will be discussed later in Sec. 3.3.2. The assembly is done by placing the front of the membranes on top of the each other (see Fig. 3.2a) which gives a well-defined intermembrane separation d . d can in principle be down to even below microns in order to form very short arrays.

In the back-to-front geometry, the assembly starts with positioning two standard chips on top of each other in a way that both membranes face upwards (see Fig. 3.2b). In this case, d is the frame thickness and hence much larger (at least 30-50 microns). In this geometry, it is in principle possible to build periodic arrays having more than 2 membranes.

3.2 Previous work

The first double-membrane arrays in the Optomechanics group were assembled and characterized by Bhagya Nair during her PhD [84]. This section briefly summarizes the process, achievements, and challenges of the first generation fabrication technique in order to highlight the main reason for improving the procedure which led to a new experimental setup in Sec. 3.3 used for assembling the second generation of arrays.

3.2.1 Fabrication and optical characterization

Assembly process was started by preselection of the pairs of commercial SiN membranes in order to have similar lateral chip dimensions or using notched samples –custom samples from NORCADA with well-specified alignment features (tolerance $\pm 10 \mu\text{m}$) for the transverse dimensions (Fig. 3.3c)– to ensure a good transverse overlap of the windows. The lateral alignment was ensured by steel bars (Fig. 3.3b) and parallelism adjustments were done by applying a compressive force via a top holder (cross) mounted on low- k springs manually. The transmission through the array of light from a broadband source was monitored using a fiber spectrometer during the alignment (see Fig. 3.3a). After getting to the desired result, the process was ended by applying small dabs of epoxy or UV resist to the sides of the array to finalize the assembly. [84]

The observed normalized spectrum for an $8.5 \mu\text{m}$ array in Fig. 3.4a via the setup in Fig. 3.3a shows the Fabry Perot interference fringes, discussed in Sec. 2.2, with the first internal membrane resonance visible around 400 nm. The data are fitted with the double-membrane transmission function by using fixed input

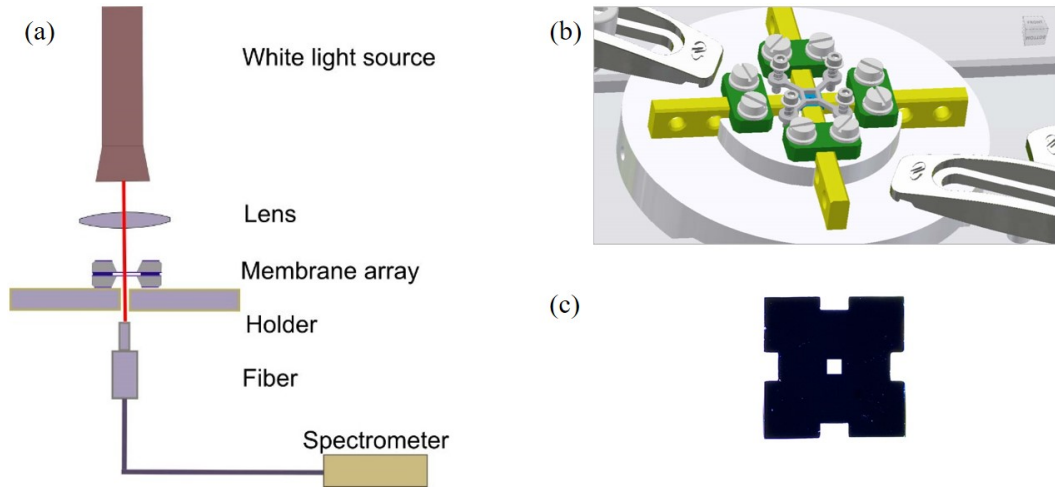


Figure 3.3: (a) Overall schematic figure of assembly setup. The white light source is a flashlight with a tungsten bulb. The beam is focused on the holder by a lens and the transmitted light collected by a multimode optical fiber and detected with a spectrometer. (b) Fabrication setup for the first generation of double-membrane arrays. The array is placed on a sample holder and held transversely by 4 aligning steel bars (yellow). The top holder fixes the membranes in place through a weak compression force. (c) Picture of a "notched" chip (the notches are for facilitating the transverse alignment of the windows in the arrays). [84]

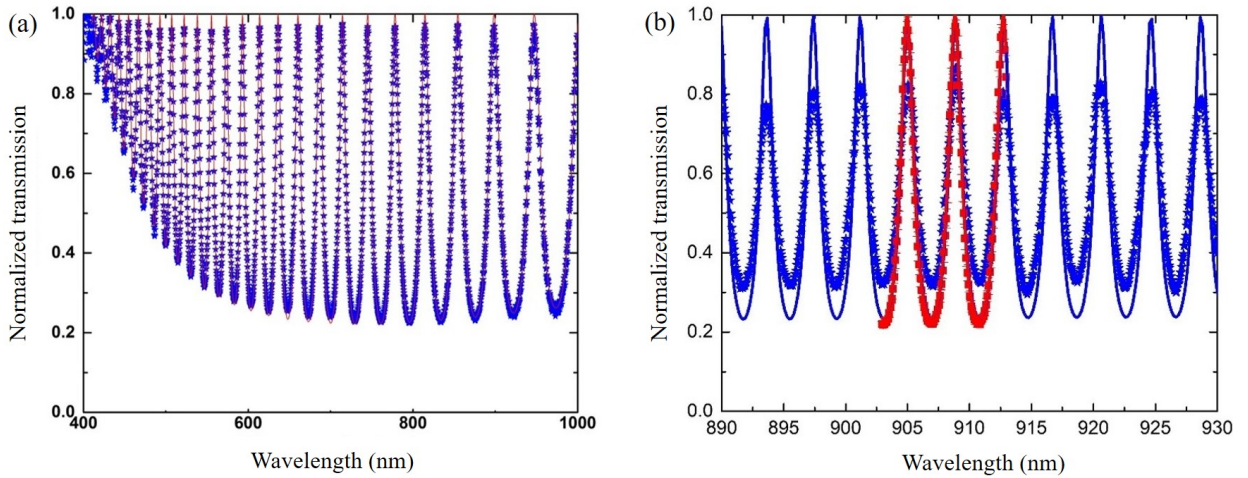


Figure 3.4: Normalized transmission spectrum for (a) a $d = 8.5 \mu\text{m}$ (front-to-front geometry) and (b) a $d = 100 \mu\text{m}$ (back-to-front geometry) double-membrane array measured by the broadband white light source. The solid lines in (a) and (b) are the results of the fits to the theoretical model introduced in Chap. 2 (Eq. (2.84)). [84]

parameters $n(\lambda)$ and thickness (l) which were determined by independent ellipsometry measurements. From such a spectrum, the intermembrane separation can be

estimated as a result of a fit to the model which in this case is $d \sim 8567$ nm [84].

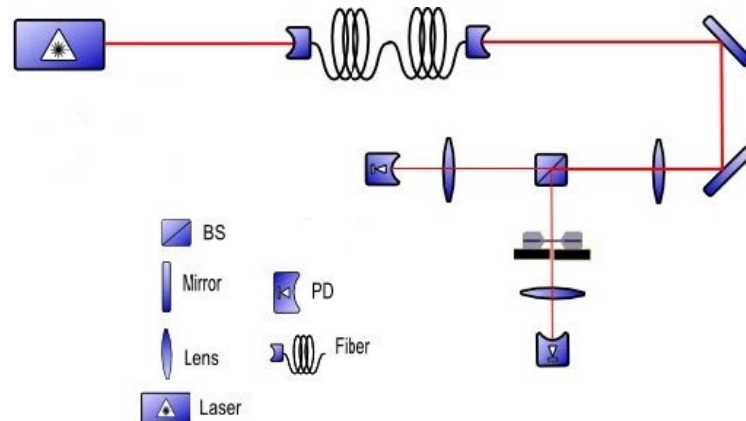


Figure 3.5: Schematic drawing of the experimental setup for accurate measurement of the transmission spectrum of membrane arrays using monochromatic light. [84]

In order to be more precise in determining the peak transmission and therefore the degree of parallelism, it is required to not be limited by the spectral resolution of the spectrometer (0.3 nm for 8.5 μm and 0.1 nm for 100 μm double-membrane arrays). To address this issue, the transmission spectrum was measured using the light from a tunable monochromatic laser source (Sacher LION diode laser (TEC 520) over the range 890-940 nm) as illustrated in Fig. 3.5. The beam was coupled to a single-mode fiber and, after passing through a 50:50 beamsplitter (BS), half of it was detected by the reference detector and the rest was focused on the array which rested on an adjustable mount with 500 μm central hole. Finally the outputs of both detectors were recorded while the laser wavelength was scanned over a certain range. The blue points in Fig. 3.4 correspond to the transmission measured under illumination with the broadband source and the red points in Fig. 3.4b give the transmission under illumination with a monochromatic source.

The highest transmission peak of an 8.5 μm double-membrane array assembled using this method was recorded at $(99.7 \pm 0.1)\%$. However, many other arrays assembled in this fashion showed much lower transmission peak values, around 95% or less. Similar spectra (see for instance Fig.3.4b in red) were also measured for 100 μm and 200 μm arrays for which the maximum transmission was never higher than 95-97%. [84]

3.2.2 Effect of parallelism on the transmission

Absorption being negligible for these films and films from the same production batch having essentially identical refractive index and thickness (and thereby identical transmission), these deviations from the perfect transmission could generally be attributed to imperfect parallelism. In order to estimate the typical intrinsic tilt of the arrays, AFM and profilometer measurements of the spacer thickness and roughness of the samples were performed by Bhagya. The typical intrinsic tilt for the $8.5 \mu\text{m}$ spacer chips was found to be the order of 0.1 mrad and for the other samples in which the surface of the Si chip was measured, the tilt was typically the order of 0.5-1 mrad [84].

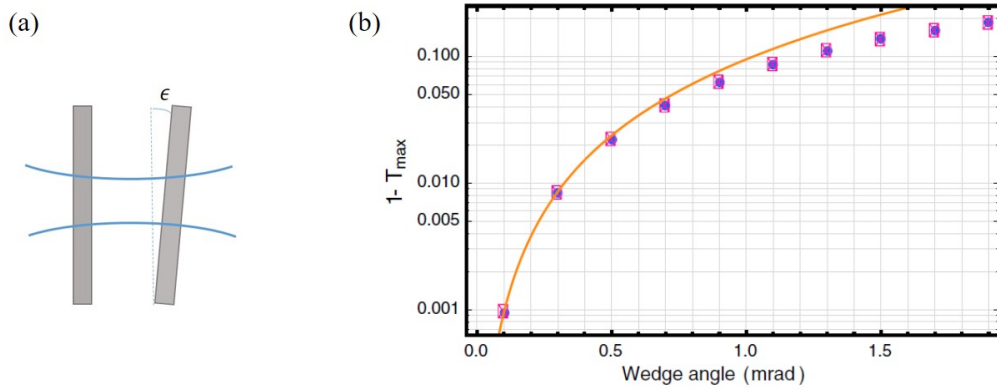


Figure 3.6: (a) Schematic picture of wedged double-membrane array with a tilt angle ϵ . (b) $1 - T_{\max}$ as a function of tilt angle for $w_0 = 50 \mu\text{m}$ and for 35% reflectivity membranes ($\lambda \approx 900 \text{ nm}$) with $n = 1.99$ for $8.5 \mu\text{m}$ (\circ) and $200 \mu\text{m}$ (\square) double-membrane arrays. The orange curve shows the lowest order expansion quadratic in the tilt angle. [81]

In Fig. 3.6b, the expected transmission of a double-membrane array with a tilt between the two identical membranes (Fig. 3.6a) is shown while the Gaussian nature of the beam is taken into account. As can be seen in Fig. 3.6b, the typical intrinsic tilt of the samples can explain the observed levels of peak transmission, although additional tilt during the assembly process or the presence of the dirt may often have contributed. Based on the predictions of Fig. 3.6b, one can see that, in order to achieve a 99.9% peak transmission, it is essential to control the tilt better than 0.1 mrad [81].

This was difficult to achieve for the arrays using a compressive force that was applied manually. Moreover, it required to have a carefully calibrated monochromatic light transmission to monitor the transmission during the assembly, instead of relying on the unprecise transmission levels provided by the fiber spectrometer.

3.3 Second generation of double-membrane arrays

3.3.1 Fabrication

3.3.1.1 Experimental setup

A new setup including both mechanical and optical parts was thus designed and built in order to have more control over the compressive force which is applied on the chips while precisely monitoring the transmission during assembly. As it is shown in Fig. 3.7a, there were four fixed Picomotor Actuators (New Focus 8302-V) on a stage above a homemade sample holder with a 2 mm diameter central hole. Their movements were controlled by a Picomotor Controller (New Focus 8743-CL). The travel range for these actuators is 25.4 mm and the length changes are in form of the number of steps, each step being approximately $0.025 \mu\text{m}$, which allowed fine-positioning during the optimization process. A designed top holder (cross) with dimensions 15 mm \times 15 mm (corresponding to the positions of the tips of the actuators), which made with four springs glued on its corners, such that these could fit the four holes on the sample holder (see Fig. 3.7b). Each actuator moved in fine steps to get in contact with the top holder corners slowly during the optimization process and used to adjust the parallelism. By moving one actuator and pushing on the corresponding corner of the cross, the force on the corner of the top chip will change the parallelism and by repeating this action in a pattern on all corners, it is possible to control the array's parallelism and the intermembrane separation. In order to observe these changes precisely, the transmission under monochromatic illumination was measured during the optimization process, as shown in Fig. 3.8 and described below.

In the optical part of the assembly (see Fig. 3.8), a diode laser (TOPTICA-DLC pro) tunable in the range 915-985 nm, was used as the monochromatic light source. The output beam was coupled to a single-mode, polarization-maintaining fiber and, after passing through a polarizing beamsplitter (PBS), was focused on the sample with a waist of $80 \mu\text{m}$ by a lens. To monitor the intensity fluctuations of the light incident on the sample, half of the light was picked up by 50:50 beamsplitter (BS) prior to focusing. Both the reflected signal by the BS and the signal transmitted through the sample were simultaneously recorded via photodetectors (Thorlabs Si Biased Detector- DET36 A/M) (PDs) which were connected to an Agilent (KEYSIGHT- InfiniiVision DSOX2024A) oscilloscope. The transmitted signal through the sample could be referenced to the reflected signal, thereby allows to minimize the power fluctuations of the laser. This referenced transmission is then normalized by the same referenced transmission spectrum without the sample

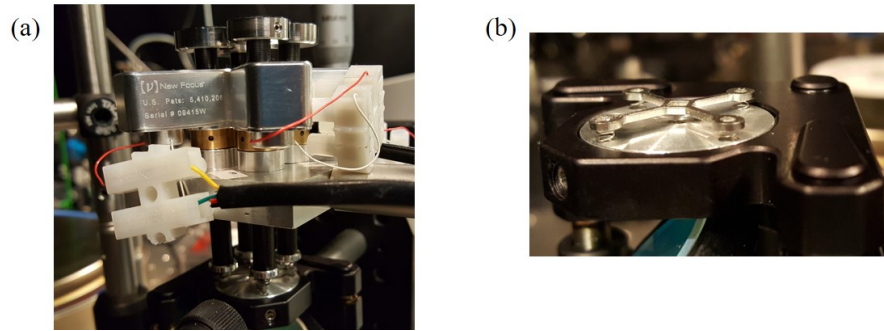


Figure 3.7: (a) Mechanical part of the setup with four fixed actuators on a stage above the sample holder: each one of them is brought in contact with the corresponding corner of the top holder (in a cross shape). (b) Top holder in a shape of a 15 mm \times 15 mm cross with glued springs on each of its corners that could fit into the four holes on the sample holder.

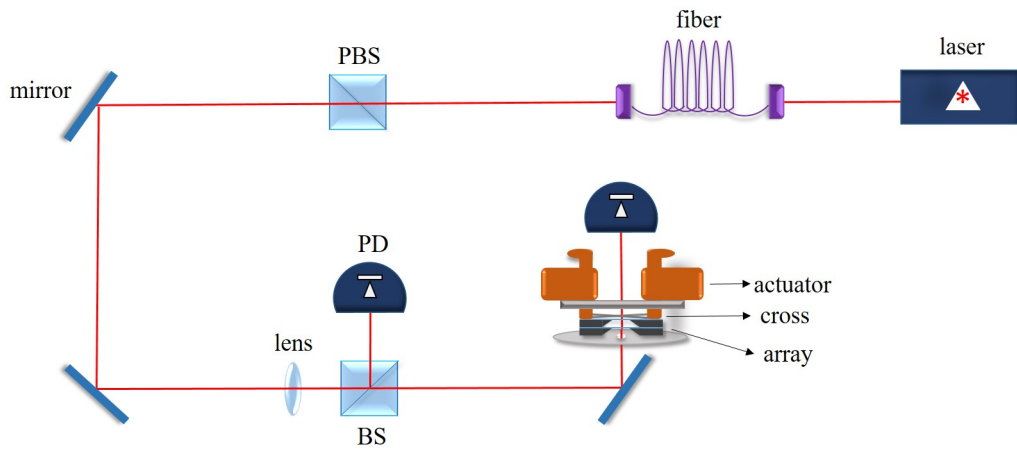


Figure 3.8: Schematic picture of assembly and optical characterization setup. PBS: polarizing beamsplitter, BS: beamsplitter, PD: photodetector.

being present, giving the final normalized transmission at a specific wavelength. The wavelength of the laser was then scanned to obtain the normalized transmission spectrum.

As can be seen from Fig. 3.9, by applying UV resist drops on the corners of the SiN film of the bottom chip, the resist acts as a viscous medium in between the membranes and actuators' forward and backward movements could change the force on each corner of the top holder and eventually it affects the parallelism of the array. During the optimization process, the transmission spectrum of the array was monitored after each step and the parallelism was improved by iterative optimization of the peak transmission spectrum.

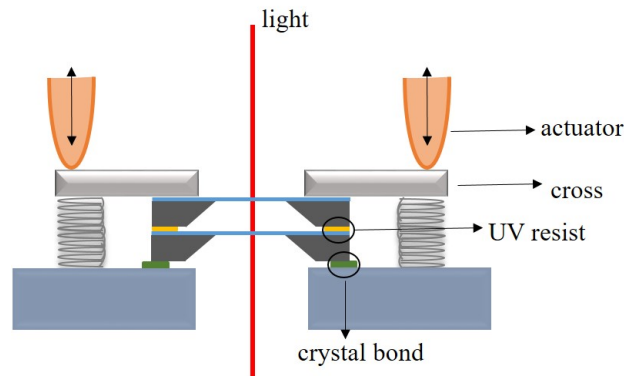


Figure 3.9: Schematic illustration of a sample in the setup in more details.

3.3.1.2 Calibration

The normalized transmission spectrum is obtained by taking the ratio of the referenced transmissions with and without sample present for each wavelength. To assess the precision with which the transmission of a sample can be measured, we can look at calibration spectra without sample. Figure 3.10a shows the dependence of the referenced transmission ratio with the wavelength, which confirms that we need this measurement in the absence of sample in the whole wavelength range. The relative standard deviation as a function of wavelength is presented in Fig. 3.10b and the standard deviation is observed to be below 0.025%, which is an acceptable level if one wishes to measure the transmission at the per mil level.

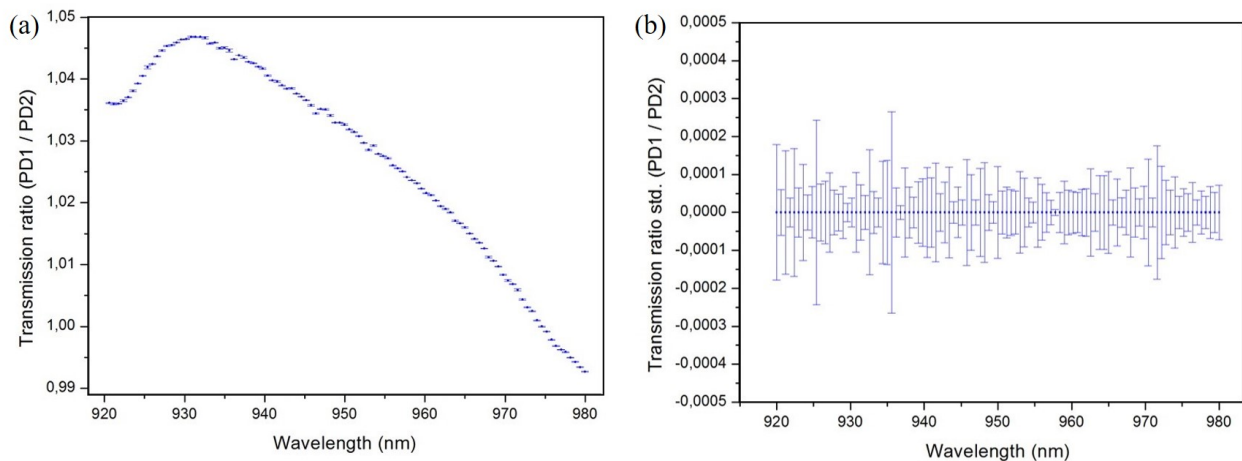


Figure 3.10: (a) Referenced transmission and (b) standard deviation of the measurement in the whole wavelength range of laser without having any sample. Data points are the average of three repetitions.

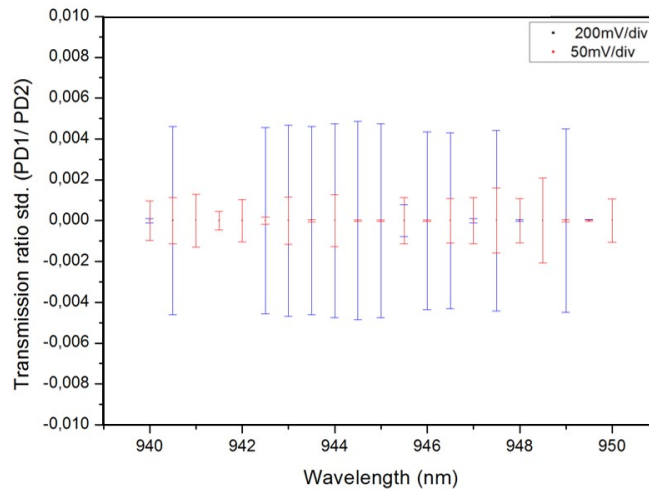


Figure 3.11: Transmission ratio standard deviation recorded by the oscilloscope in dynamic ranges 200 mV/div and 50 mV/div. Each data point is an average of three measurements.

To achieve this goal, the signals measured by each photodiodes (varying between 0 and 10 V) were each recorded on two channels of the oscilloscope: the first channel used a wide dynamic range (200 mV/div) to measure the signal through the whole range and the other channel recorded the signal in a narrower range (50 mV/div) using the offset determined by the first channel. The choice of the dynamic range affects the precision of measurement and as it is shown in Fig.3.11, the standard deviation difference of the measured signal by using these two ranges was about 0.3% . While using 50 mV/div as the measurement final dynamic range could improve the precision, it also lowered the speed of data collection, since it required to find the offset in the wider dynamic range and adjusting it in the 50 mV/div range to record the data in each wavelength.

The aim was to find a way to have the same error bars in 50 mV/div and at the same time reduce the measurement time. The solution was to use four channels of the oscilloscope and each detector was connected to two of those channels, one in the dynamic range of 200 mV/div and the other one in 50 mV/div. Therefore, finding the transmission level in each wavelength of the laser was performed in 200mV/div in the shorter time with fewer averages and at the same time by adjusting the offset, the data could be recorded in 50 mV/div with $\text{std.} \leq 0.1\%$, thus yielding sufficient precision and increasing the speed of measurements by roughly a factor of 2.

3.3.2 Optical characterization

For fabricating the second generation of double-membrane arrays, samples were made from chips having a $5 \times 5 \text{ mm}^2$ Si frame with 200 or 500 μm thickness and a $0.5 \times 0.5 \text{ mm}^2$ Si_3N_4 window with 100 nm thickness. At first, the bottom chip was fixed on the sample holder by applying crystal bond droplets as the adhesive because of its low melting point which makes it easy to remove after finalizing the array just by increasing the temperature slightly. The next steps in the process depend on the desired intermembrane separation which leads to three categories of double-membrane arrays: "large", "medium" and "short" d .

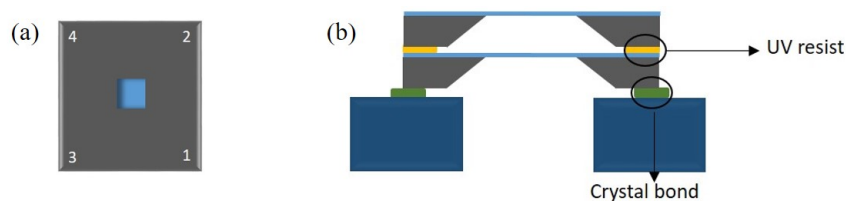


Figure 3.12: Schematic pictures of (a) a chip with labeling Si frame corners and (b) a glued double-membrane array on the mount by crystal bond with UV resist in between Si frames.

3.3.2.1 "Large" d

In this group of arrays, the chosen geometry is back-to-front (see Fig. 3.2b) and the standard chips have Si frames with 200 μm thickness. After fixing the bottom chip on the mount, small dabs of UV resist (OrmoComp, Micro resist technology GmbH) were applied manually by a tip of a 0.8 mm-diameter needle on two diagonal corners of the Si frame (it could be 2 and 3 or 1 and 4 in Fig. 3.12a). The important point is to apply as little resist as possible in order to minimize the risk of dispersing the resist on the membrane window or causing the membrane array to be sealed during the optimization process. In addition, having the dabs of resist close to the frame's edge lowers the risk of affecting the mechanical properties of the membranes, which depends on the residual stress of the SiN film. The top chip was then put in the chosen geometry (Fig. 3.12b), and the parallelism optimization process began.

As shown in Fig. 3.13, the transmission spectrum of the sample in the initial state (before the actuators were brought in contact with the pressing cross) shows a poor peak transmission ($\sim 85\%$), as a result of imperfect parallelism. After multiple displacements of the actuators and maximization of the peak transmission, the final spectrum (red) shown in Fig. 3.13 is obtained. Concomitantly with an increase in the peak transmission, one observes a reduction in the intermembrane distance,

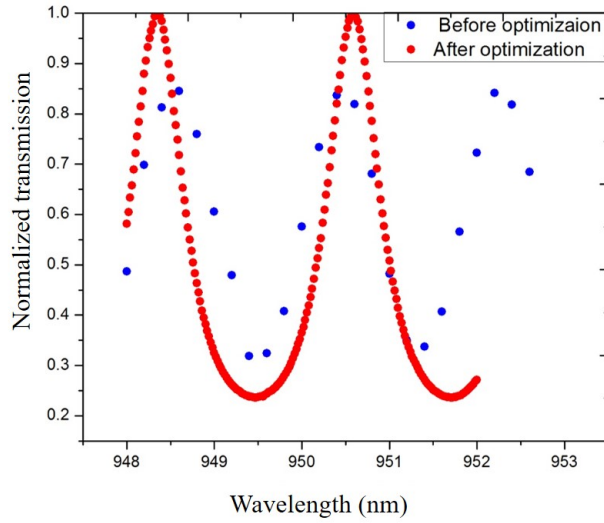


Figure 3.13: Recorded normalized transmission spectrum of the $200\ \mu\text{m}$ double-membrane array before (in blue) and after (in red) the optimization process. Each data point is an average of three repetitions.

from $d \simeq 253.36\ \mu\text{m}$ to $202.02\ \mu\text{m}$ in this example. Data points show that the d is reduced during the process, while a better transmission is achieved. In order to fix the distance between two membranes and stabilize the sample, the UV resist was cured with a UV pointer (at $\lambda = 405\ \text{nm}$ and $5\ \text{mW}$ power) and the actuators and pressing cross were removed and the sample released from the holder. The transmission spectrum of the double-membrane array before and after removing the actuators and pressing cross from the array shows the same intermembrane separation and a stable array.

The normalized transmission of the released sample was remeasured over the whole available wavelength range in order to have a better determination of the intermembrane distance, as well as a precise determination of the peak transmission. This spectrum is shown in Fig. 3.14, together with the results of a fit to the theoretical model introduced in Chap. 2 (Eq. (2.84)). By having the theoretical model in which l and d were the free fitting parameters and the previously determined fixed value for the refractive index ($n = 1.966 \pm 0.001$). The result of the fit gives an estimation for the intermembrane separation $d = (202.026 \pm 0.001)\ \mu\text{m}$ and the membrane thickness $l = (102.83 \pm 0.04)\ \text{nm}$ for this case. The excellent agreement between the data points and the fit results explains the very small error on d . However, several systematic factors have not been taken into account in this estimation, for instance, the laser wavelength was not absolutely calibrated or the refractive index of air was ignored. Finally, let us remark that the final intermem-

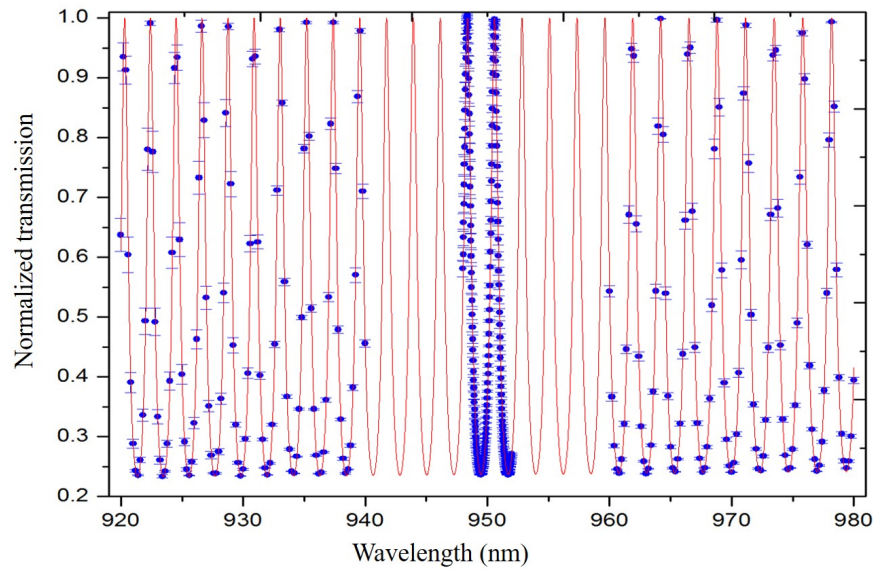


Figure 3.14: Recorded normalized transmission spectrum of the $200\ \mu\text{m}$ double-membrane array for the whole wavelength range of laser (in blue) and the fit to the data points (in red). Data points are the average of three repetitions.

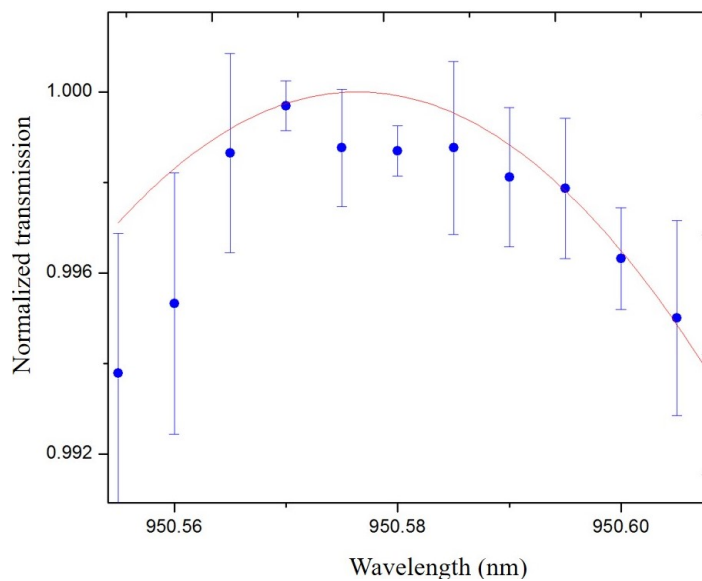


Figure 3.15: Recorded normalized transmission spectrum of the $200\ \mu\text{m}$ double-membrane array around one of the wavelengths with the transmission peak with smaller steps and each data point is the average of three repetitions (in blue). The data is then fitted (in red).

brane distance is the sum of the thickness of the Si frame ($200\ \mu\text{m}$) and the final resist layer. Given the uncertainty on the initial spacer thickness, it was not pos-

sible to precisely evaluate the thickness of the final layer of the resist for this sample.

To determine the peak transmission, the optical transmission was recorded around one of the peak wavelengths (in this case $\lambda = 950.58$ nm) with three repetitions and by fitting the curve again, the peak transmission for this sample was found to be $(99.90 \pm 0.07)\%$, which is substantially higher than the first generation arrays assembled from the same chips. However, lower transmission levels were also sometimes observed using this method for other double-membrane arrays. We surmise that possible reasons could be an intrinsic wedge (higher than expected), dirt or anything that could not be compensated by the thickness of the UV resist layer at the end of the optimization process. Since the (unknown) thickness of the final resist layer is critical in determining how large a degree of nonparallelism can be compensated, we thus decided to investigate arrays with a smaller and well-known d .

3.3.2.2 "Medium" d

In order to have arrays with smaller d and better control on the distance between two membranes, the front-to-front geometry (see Fig. 3.2a) was chosen. Both chips had a 0.5×0.5 mm² SiN window with 100 nm thickness while the 5×5 mm² Si frame had a thickness of 500 μm . One of them was a standard chip and the other one was a custom made chip in which a well-defined 8.5 μm spacer was deposited on the SiN film (see Fig. 3.16a). The chip with the spacer was fixed on the mount and the small dabs of UV resist were applied manually on all the four corners of the spacer (1 to 4 in Fig. 3.12a). To increase the resist viscosity and slow down its spreading during the application of the compressive force, precuring of the resist was performed. To precure the UV resist, the UV pointer was positioned around 10 cm far from a density filter (NE05A-B BBAR COATING 650-1050 nm) and used to illuminate the spots for 15 seconds. After that, the top chip was placed in the front-to-front geometry (see Fig. 3.16b) and the optimization process began. As shown in Fig. 3.17a, there are initially two peaks visible in the available wavelength range that are about 35 nm apart from each other which means that the starting intermembrane separation was higher than 10 μm to start with.

After optimizing the parallelism, reaching the highest possible normalized transmission of the array and curing the UV resist (see Fig. 3.16c) to stabilize the array, the transmission spectrum of the sample was recorded which is shown in Fig. 3.17b. The blue circles are the recorded data points and the red line is the result of a fit with the theoretical model data which gives the intermembrane separation $d = (9.84 \pm 0.23)\mu\text{m}$ and the thickness of the membrane $l = (94.52 \pm 0.09)$ nm. The same procedure was done to determine the peak transmission by taking

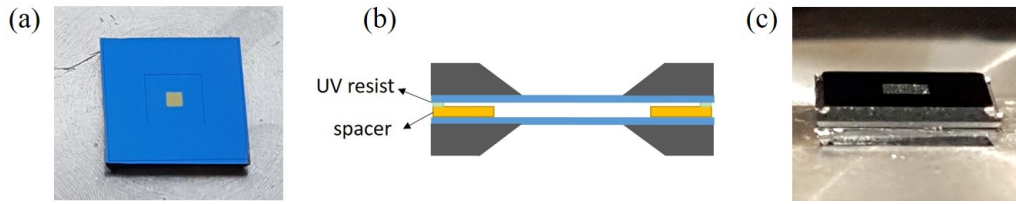


Figure 3.16: (a) A custom made chip from NORCADA with an $8.5 \mu\text{m}$ spacer deposited on the SiN film. (b) Schematic picture of a double-membrane array in the front-to-front geometry. The resulting intermembrane separation is slightly more than $8.5 \mu\text{m}$ (thickness of the spacer). (c) Picture of the double-membrane array made in the front-to-front geometry.

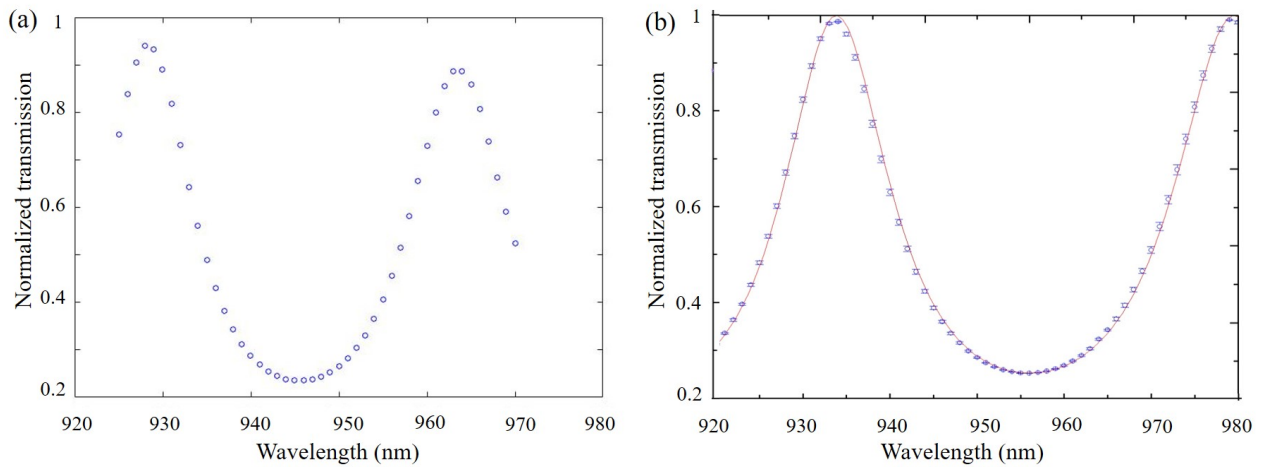


Figure 3.17: For the array with an $8.5 \mu\text{m}$ spacer and UV resist in between we have (a) the transmission at the initial state of positioning the membranes before optimization process and (b) the normalized transmission spectrum of the array (data points in blue) and fit to data points (in red). Data points are the average of three repetitions.

the optical transmission around one of the peaks in Fig. 3.17 which was found to be $(99.80 \pm 0.03)\%$ at $\lambda = 933.4 \text{ nm}$.

Considering the fact that the d is the spacer thickness ($8.5 \mu\text{m}$) plus the remaining resist layer in between, an estimate of the size and distribution of resist on the surface of the frame is possible. By taking a picture of the initial resist dabs on the corners of the bottom chip, it could be seen that they had a hemispherical shape with an approximate radius of 0.1 mm which gives a volume $2 \times 10^{-3} \text{ mm}^3$. Assuming that the final shape of the resist layer to be a quarter of a cylinder, one gets a final resist layer thickness of $h \approx 1.3 \mu\text{m}$ (difference of the d and the spacer thickness). Assuming volume conservation, the radius of the resist layer after the fabrication process is estimated to be 1.4 mm , i.e. the final resist layer is

expected to extend to about halfway between the frame corner to the SiN window. While this shows a possibility to increase the amount of resist to make the distance controllably higher even after distribution, one should bear in mind that the resist layer may affect the residual stress and, thereby, the mechanical properties of the membrane.

3.3.2.3 "Short" d

Motivated among others by the realization of squeeze film sensors with short membrane sandwiches discussed in Chap. 4, we also wanted to investigate arrays with much shorter intermembrane spacing than $8.5 \mu\text{m}$. However, making arrays with d 's of e.g. few microns rendered impossible the measurement of a full interference fringe with the available laser ranges. The setup in Fig. 3.18 was used to address this issue, the laser was replaced by a flashlight with a tungsten bulb (Maglite) as broadband (400-1000 nm) light source and by having an optical fiber connected to a spectrometer (Ocean optics HR4000CG-UV-NIR), the transmission could be monitored.

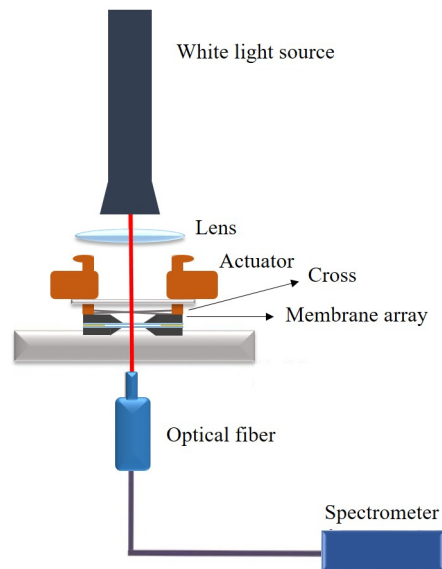


Figure 3.18: Fabrication setup for the "short" d double-membrane arrays. The cross on top of the array transfers the compression force by the four Picomotor Actuators to the top chip. The white light source is a flashlight with a tungsten bulb and the beam is focused on the holder by a lens. Transmitted light collected by a multimode optical fiber and detected with the spectrometer (Ocean optics HR4000CG-UV-NIR).

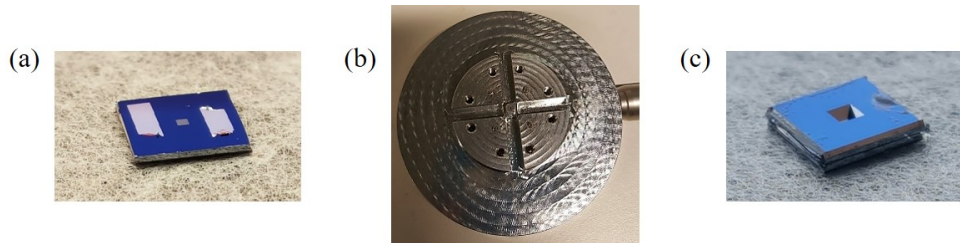


Figure 3.19: (a) Al spacer with 1020 nm thickness deposited on a sample with a $5 \times 5 \text{ mm}^2$ Si frame with $500 \mu\text{m}$ thickness and a $0.5 \text{ mm} \times 0.5 \text{ mm}^2$ SiN windows with 100 nm. (b) Mount with a central hole $300 \mu\text{m}$. (c) Double-membrane array with Al spacer in between.

The first way of decreasing d is to deposit a spacer with a lower thickness, for this case, a chip with an aluminum spacer with 1020 nm thickness was used in the array fabrication. This Al spacer was deposited by Bjarke Rolighed Jeppesen in the Interdisciplinary Nanoscience Center (iNANO) cleanroom on a standard chip with a $500 \mu\text{m}$ frame thickness (see Fig. 3.19a). After fixing the sample with the Al spacer on the mount, the top chip was put in the front-to-front geometry and the optimization process was begun. The optimization process was followed by monitoring the white light spectrum, moving the actuators and finished by applying the UV resist to the side of the sample while there were still actuators on top and then curing it for finalizing the array (see Fig. 3.19c).

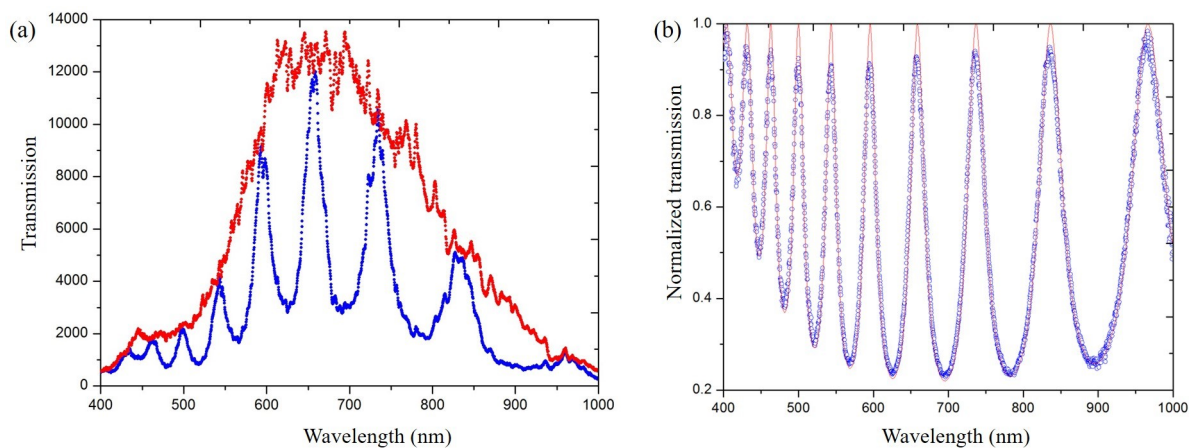


Figure 3.20: (a) White light spectrum for the double-membrane array with Al spacer with sample (blue) and without sample as the reference (red). (b) Normalized transmission data points (blue) and fit to the data (red).

To properly normalize the transmission of the array, it was essential to replace the current mount with the other mount which has a much smaller central hole ($300 \mu\text{m}$) than the membrane window (Fig. 3.19b) since part of the incoming light

was already blocked because of the size of membrane window in the current mount. As it could be seen in Fig. 3.20a, the white light spectrum was recorded both when the sample was on the mount and without it. The ratio of both spectra, after background subtraction, gave the normalized transmission for this sample in the wavelength range 400-1000 nm. Fit to the theoretical model (see Fig. 3.20b) gives $d = (2955.9 \pm 0.1)$ nm and $l = (87.45 \pm 0.05)$ nm.

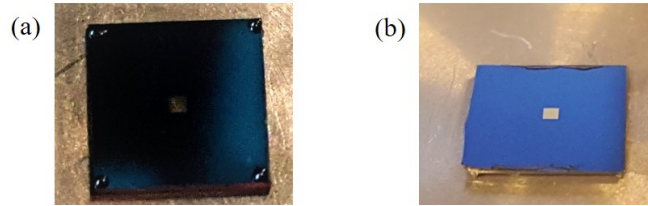


Figure 3.21: Pictures of UV resist in forms of (a) spots on four corners of a SiN film and (b) two lines along two opposite sides of a SiN film.

In another attempt, we aimed at avoiding entirely depositing a spacer by using the resist as a "tunable" spacer. Two standard chips having a Si frame with 500 μm thickness and the same geometry (see Fig. 3.2a) were used to make this sample. The important step was applying the UV resist in small dabs, as identical as possible, on all four corners of the SiN film (Fig. 3.21a) or as two thin lines along opposite sides and close to the edges (Fig. 3.21b). The rest of the fabrication process including precuring proceeded as previously.

At the end of the process, the normalized transmissions for two samples that were made with these two different patterns of UV resist-spacer are shown in Fig. 3.22. As can be seen, d is reduced as compared to the previous case (Al spacer array) since the spacing of the fringes is increased. Using a membrane thickness of 87 nm, for the UV-resist spacer array on all 4 corners of Si frame (see Fig. 3.21a), the fit on Fig. 3.22a gives $d = (1741.05 \pm 0.11)$ nm and for the double-membrane array with the two lines of UV resist as a spacer (see Fig. 3.21b), the fit on Fig. 3.22b gives $d = (2119.70 \pm 0.47)$ nm. In both cases the peak transmission is no longer as high as before since decreasing d and preserving high Q without sealing the array were the first priorities.

3.3.3 Summary

To summarize we improved the previous assembly methods by building a new setup and implementing a more reproducible and controllable process to achieve highly

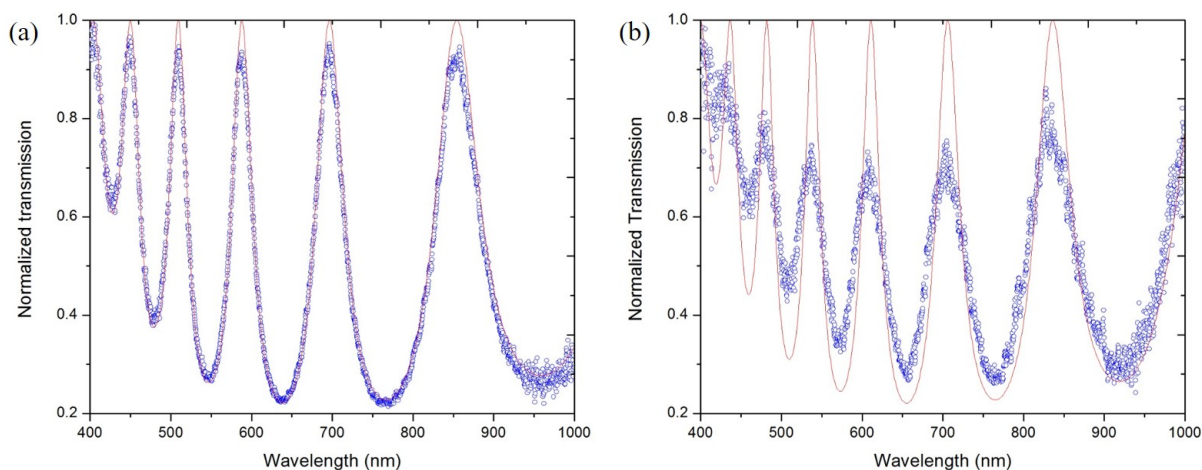


Figure 3.22: White light spectrum for the double-membrane array with UV-resist spacer (a) as spots on four corners and (b) two lines along two opposite sides of the SN film. Normalized transmission data points are in blue and the fit is in red.

parallel membrane arrays. Arrays with substantially higher peak transmissions (at the 99.9% level) or with much shorter ($2 - 3 \mu\text{m}$) intermembrane separation have been made. While the factors sometimes limiting the achievable parallelism and distance still remain to be more systematically investigated, the UV resist assembly method has the potential for realizing either "ultrashort" arrays with controllable spacing or multiple (more than two) membrane arrays. Let us finally note that systematic investigations of the mechanical properties of the resulting arrays should also be carried out in order to fully assess and optimize this new assembly method.

3.3.4 Mechanical characterization

3.3.4.1 Experimental setup

As it was mentioned in Sec. 2.3, the vibrations of the membrane resonators, whether driven or thermal, can be measured by standard optical interferometry. The simplest form of interferometer used in this project is shown in Fig. 3.23a; the light coming from a monochromatic laser source (Sacher LION diode laser (TEC 520)) is injected into a Fabry Perot interferometer which includes a beamsplitter (BS) as a fixed end mirror and a membrane as a second, movable end mirror. The membrane (or array) to be characterized is resting under gravity on the corners of its frame on a circular ring mount whose inner diameter is slightly less than the frame diagonal dimension. This minimizes the coupling with external vibrations [70]. The length of this interferometer can be controlled by a piezoelectric transducer (PZT) (Noliac NAC2124 multilayer using actuation) (see Fig. 3.23b). The transmission through

the interferometer is detected with a low noise, high bandwidth photodetector (Thorlabs PDA8A) and sent to a spectrum analyzer (TEKRONIX RSA 5103B). Before sending the light into the chamber, half it is sent to another detector by a BS to monitor input power fluctuations.

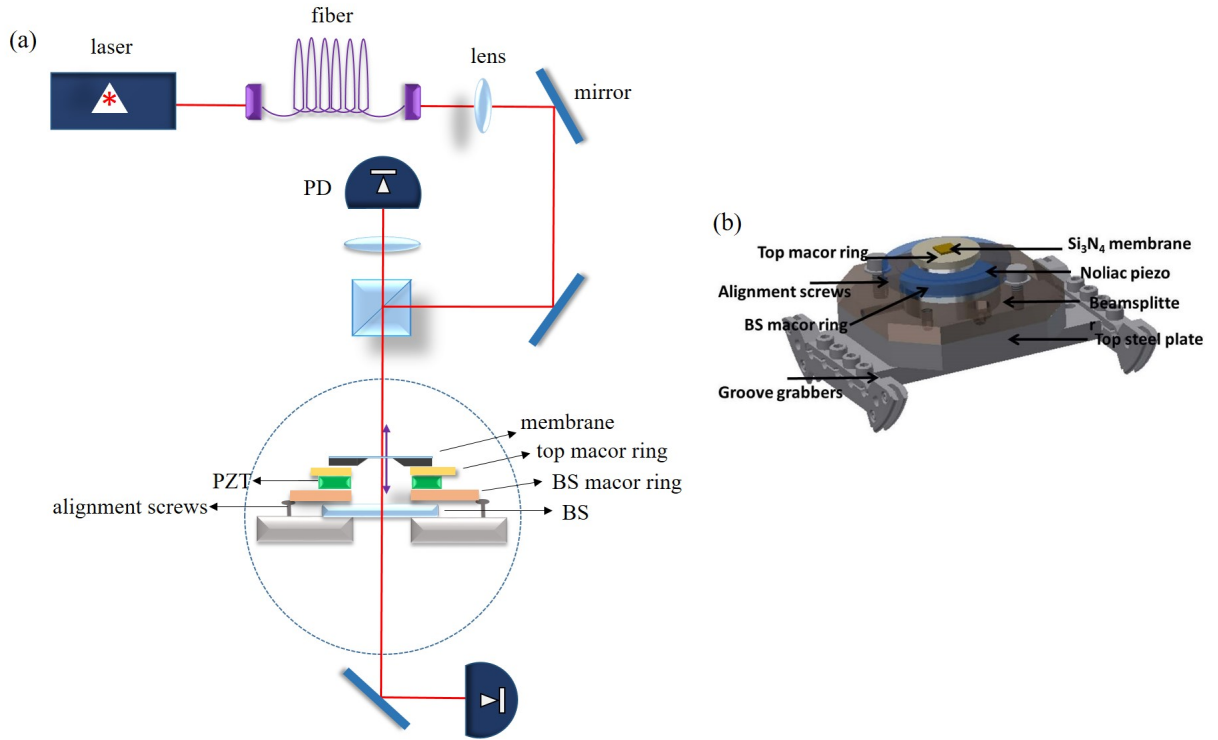


Figure 3.23: (a) Schematic drawing of the mechanical characterization setup in which light coming from a diode laser via an optical fiber is sent into a Fabry Perot interferometer inside a vacuum chamber. PZT: piezoelectric transducer, BS: beamsplitter, PD: photodetector. (b) Schematic picture of the interferometer assembly inside the mechanical characterization chamber [84].

The PZT is connected to a combination box (see Fig. 3.24) made in the electronics workshop which combines the DC signal and the RF modulation. The design uses a capacitor with $4.5 \mu\text{F}$ which is ten times larger than that of the PZT at 1 MHz. Having a $100 \text{ k}\Omega$ resistor enables the combination of the DC signal the waveform generator (Agilent 33220A) with an RF modulation from the RF generator and the combination of the capacitor and resistor results in an RC characteristic time around 0.35 s. The output of the combination box is monitored by the "PZT monitor" which was tested and confirmed that it gives the same values as "Output to PZT".

In such a single membrane-BS interferometer, the transmission of the interferometer is given by:

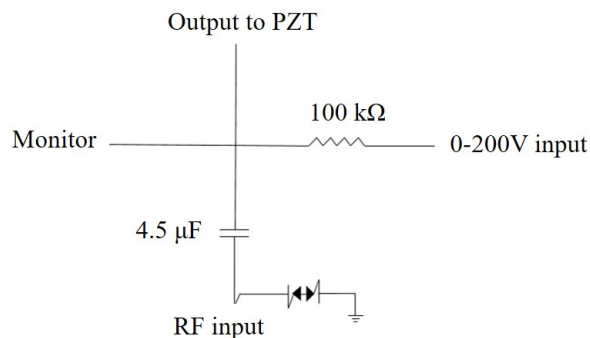


Figure 3.24: Schematic graph of the piezo combination box circuit with the DC and RF inputs.

$$T = \frac{T_0}{1 + F \sin^2\left(\frac{2\pi(L+x(t))}{\lambda}\right)}, \quad (3.1)$$

where F is the factor of the finesse of this resonator that depends on the reflectivity of BS and the membranes, L is the length of the interferometer (about 7 mm, depending on the alignment and the sample) and $x(t)$ is the amplitude of the displacement of the considered. As discussed in Sec. 2.3, varying the length of the interferometer (or the wavelength of the light) yields interference fringes. To maximize the displacement sensitivity one chooses a cavity length (or laser wavelength) so as to operate at mid-slope.

For the mechanical characterization of a double-membrane array, the BS can in principle be removed and one still has a Fabry Perot interferometer with two movable end-mirrors. The distance between the membranes being fixed, one can scan the laser wavelength to operate at mid-slope of the interference pattern (see Fig. 3.25b). In practice, this is possible with arrays with a "large" or a "medium," d , in our case, due to the available laser range.

Making an interferometer consisting of a double-membrane array and the BS may, though, be required –for "short" d arrays– or for not very parallel arrays. The interference pattern is more complex and the best displacement sensitivity can be optimized by tuning both the laser wavelength and the PZT voltage, so as to maximize the displacement peak noise for a specific mode. In addition, optical and mechanical mode overlap, array parallelism and alignment may also considerably influence the sensitivity, as we discuss below.

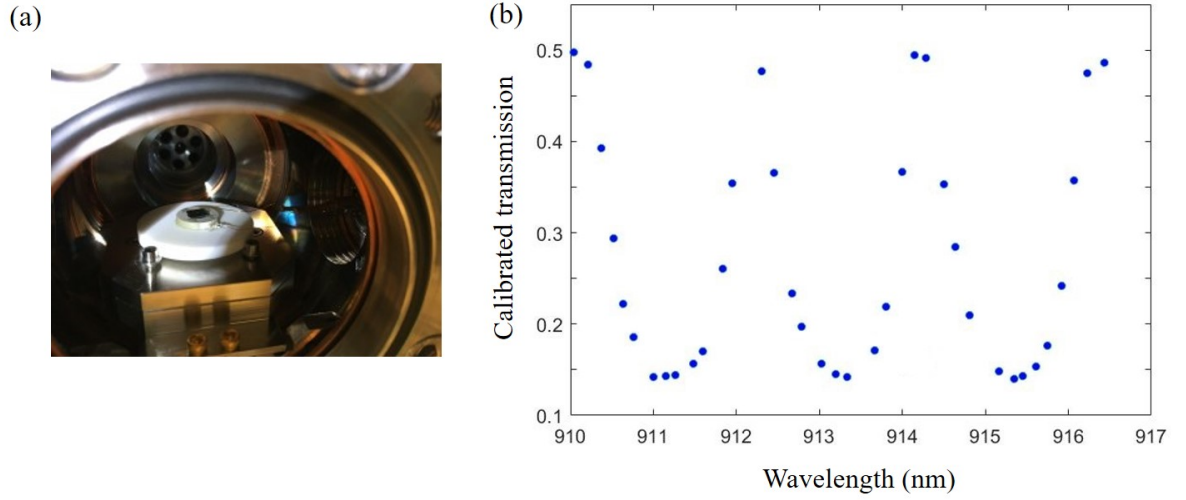


Figure 3.25: (a) Picture of a membrane glued on the PZT lying on the mount. (b) An example of the interference fringes of a double-membrane array's transmission with a large d inside the chamber.

3.3.4.2 Spectrum analyzer measurements

As it was mentioned, the output signal of the PD is sent to the low-resolution bandwidth spectrum analyzer (RSA) as its input voltage. The data collection was done in DPX mode when measuring thermal noise spectra (Section 3.3.4.3.1) and in zero-span mode when performing ringdown spectroscopy (Section 3.3.4.3.2). In zero-span mode, the local oscillator of the spectrum analyzer is fixed at a chosen frequency and the variations of the signal amplitude (or power) are displayed as a function of time. In DPX mode, the spectrum analyzer is used for recording the thermal fluctuations of a mechanical mode, therefore the output is a voltage power spectrum. RSA approximates the power spectral densities by normalizing the measured power spectrum by its effective bandwidth and it is done by defining the power spectrum as the integral of the voltage power spectral density over an effective bandwidth as it was discussed in [70]. One can get try to estimate the best displacement sensitivity that could be obtained in our interferometer if the measurement was shot-noise limited.

Knowing the wavelength-dependent responsivity of the detector, \mathcal{R} , the photocurrent $i(t)$ produced by the transmitted power $P_{out} = TP_{in}$, is given by $i(t) = \mathcal{R}P_{out}$. To quantify the sensitivity of the displacement measurement, the power spectral density $S_i(\omega)$ of photocurrent fluctuations produced by the interferometer length fluctuations $S_x(\omega)$ is compared to the spectral density of photocurrent shot noise fluctuations $S_i^{shot}(\omega)$:

$$S_x^{shot}(\omega) = \frac{S_i(\omega)}{S_i^{shot}(\omega)} \quad (3.2)$$

where for the transmitted field:

$$S_i(\omega) = \left(\mathcal{R} \frac{dP_{out}}{dL}\right)^2 S_L(\omega) = \mathcal{R}^2 \left(\frac{2\pi}{\lambda}\right)^2 F P_{out}^2 C^2(F) S_L(\omega) \frac{A^2}{Hz}, \quad (3.3)$$

and

$$S_i^{shot}(\omega) = 2e\langle i \rangle = 2e\mathcal{R}P_{out} \frac{A^2}{Hz}. \quad (3.4)$$

The shot-noise-limited displacement sensitivity of the interferometer in amplitude units can be estimated by:

$$\sqrt{S_x^{shot}} = \frac{\lambda}{\pi} \sqrt{\frac{e}{2F\mathcal{R}}} \sqrt{\frac{1}{P_{out} C(F)}} \frac{1}{Hz}, \quad (3.5)$$

where e is the elementary charge and $C(F) = \sqrt{\frac{F}{1+F}}$.

The estimation can be done for a thermal displacement amplitude of the fundamental vibration mode of a membrane $l = 100$ nm, $a = 500$ μm , $\rho = 2.7$ g/cm^3 , $\omega_m/(2\pi) = 800$ kHz and $Q = 10^6$ at $\lambda = 900$ nm which has the effective mass $m \approx 8.4$ ng. The rms vibrational amplitude due to thermal agitation with energy $k_B T_{room}$ is $\sqrt{k_B T_{room}/m\omega_m^2} = 4.4$ pm for $T_{room} = 298$ K. Half of this displacement is contained in a bandwidth of $\omega_m/Q/(2\pi) = 0.8$ Hz, corresponding to a noise amplitude of ≈ 4.9 pm/ $\sqrt{\text{Hz}}$. Equation (3.5) suggests that the necessary probe power to achieve shot-noise-limited sensitivity at this level would be < 1 μW . In practice the commercial photodetector in the setup has the $\mathcal{R} \approx 0.56$ A/W and a transimpedance gain of 100 kV/A. For $T_{max} = 1$ and $F = 2.4$, we have $C(F) = 0.76$. Therefore, for a power ≈ 100 μW at 900 nm, the shot noise limited displacement sensitivity:

$$\sqrt{S_L^{shot}} \approx 9.3 \frac{fm}{\sqrt{\text{Hz}}}, \quad (3.6)$$

which means that in 1 Hz bandwidth we should be able to measure a thermal motion amplitude of 4.4 pm with a signal-to-noise (in power units) of 47 dB. However, the highest signal-to-noise that we have achieved in the same bandwidth was ≈ 23 dB. This difference could be a result of imperfections in alignment and mode-matching between the optical beam and the membrane as well as laser excess noise.

3.3.4.3 Q determination

3.3.4.3.1 Thermal noise spectra In the absence of driving force the thermal noise spectrum of the membrane mode can be visualized on the signal measured by the RSA as Lorentzian peaks centered at the vibrational mode frequencies, superposed to the laser and electronic noise. This can be seen in Fig. 3.26, which shows the noise spectrum of a single chip with a $5 \times 5 \text{ mm}^2$ Si frame and $500 \text{ }\mu\text{m}$ thickness, $0.5 \times 0.5 \text{ mm}^2$ Si_3N_4 window with 100 nm thickness that was recorded at $\lambda = 901.54 \text{ nm}$ and 10^{-7} mbar pressure. The peaks corresponding to (1,1), (1,2), (2,1) and (2,2) vibrational modes are identified. Using the expression for the frequencies of a tensile-stress dominated square drum mode $\omega_{mn} = \frac{\pi}{a} \sqrt{\frac{T}{\rho}} \sqrt{m^2 + n^2}$ (for $m, n = 1$), and taking $a = 500 \text{ }\mu\text{m}$, $T = 0.9 \text{ GPa}$, $\rho = 2.7 \times 10^3 \text{ kg/m}^3$ for a single membrane with 100 nm thickness, one obtains the values displayed in Table 3.1, which are in good agreement with the measured values for this particular sample.

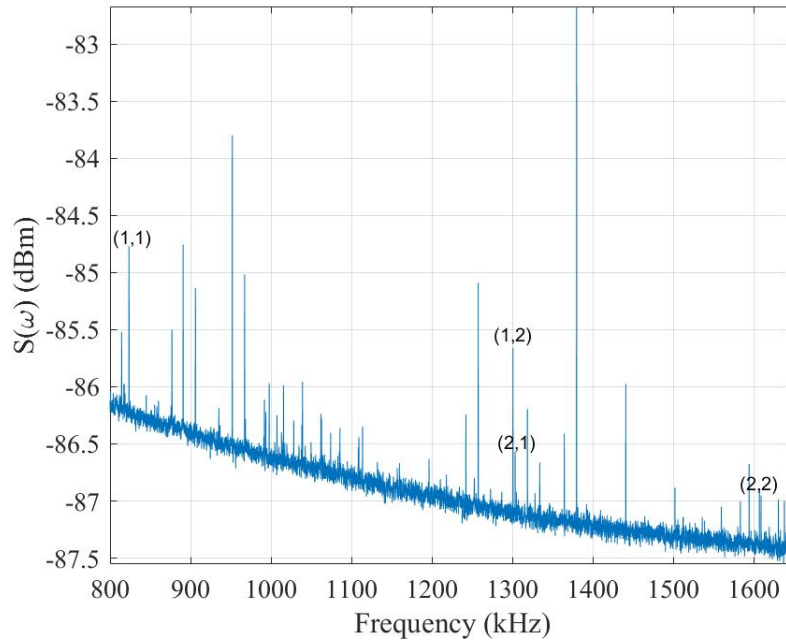


Figure 3.26: Thermal spectrum of a single membrane with 500 averages and resolution bandwidth 0.5 Hz .

The deviations of the observed frequencies from what was expected are less than 0.2% , and are most likely the result of inhomogeneous tensile stress of the membrane or a small degree of rectangularity if the drum is not exactly square.

Table 3.1: Resonance frequencies of mechanical modes of a single membrane

	(1,1)	(1,2)	(2,1)	(2,2)
Theoretical ω_m	824.14 kHz	1303.08 kHz	1303.08 kHz	1648.28 kHz
Experimental ω_m	824.25 kHz	1300.7 kHz	1305.07 kHz	1646.6 kHz

Recording the thermal noise spectrum with a resolution bandwidth (RBW) is less than the linewidth of the mechanical resonance, allows to fit the data with a Lorentzian:

$$f(A, f_m, \Delta f, f) = \frac{A}{1 + 4 \times \left(\frac{f-f_m}{\Delta f}\right)^2} \quad (3.7)$$

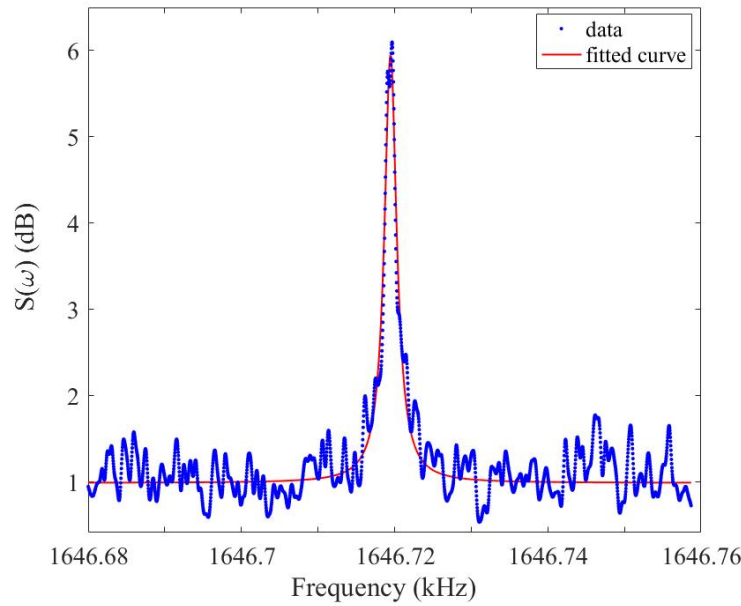


Figure 3.27: Thermal (2,2) mode spectrum of a single membrane with 500 averages and RBW 0.5 Hz.

in which the FWHM gives the γ and the mechanical Q factor will be:

$$Q = \frac{\omega_m}{\gamma} = \frac{f_m}{\Delta f}. \quad (3.8)$$

In Fig. 3.27, after recording thermal mode(2,2) the data points at RBW 0.5 Hz, the FWHM of the Lorentzian fit gives $\Delta f = (1.94 \pm 0.4)$ Hz at $f_m = (1646.72 \pm 1.87)$

kHz, which can be used to calculate $Q = (8.46 \pm 0.11) \times 10^5$. In principle, the limit for measuring the true mechanical linewidth is given by the minimal resolution of the RSA, which, in our case, is 0.1 Hz. However, the downside of using very low RBWs is that the acquisition time to achieve a resolution bandwidth of about a Hertz is on the order of seconds, and to get an ideal signal-to-noise ratio (SNR) of the spectrum, measurement averages of 50-100 traces are necessary. In this timescale, the resonance frequency drifts due to thermal fluctuations and this broadens the measured peak, preventing from reliably measuring very narrow linewidths (high Q s). For modes with very narrow mechanical linewidths, ringdown spectroscopy provides a more reliable alternative.

3.3.4.3.2 Ringdown spectroscopy In case of a driven force at the mechanical resonance which is stopped abruptly, i.e. in a step-like fashion, the oscillatory motion is exponentially damped as discussed in Sec. 2.1.2.2, and monitoring the decrease of oscillation amplitude in time is the principle of ringdown spectroscopy. As it was mentioned in Sec. 2.1.2.2, for an under damped oscillator ($\gamma \ll \omega_m$), the bare mechanical quality factor of the resonance is related to the ringdown time τ_c by:

$$Q = \pi f_m \tau_c. \quad (3.9)$$

Experimentally, the driven force is provided by a modulation at f_m of the voltage applied to the PZT. Stopping this modulation on a time scale which is shorter than the mechanical decay time and measuring the signal from the photodiode in a certain frequency window around f_m with the RSA in zero-span mode. In practice, two signal generators are used for this purpose, allowing to maximize the amplitude of the driven motion and subsequently switch the driven force on a millisecond timescale. The envelope function measured by the RSA in zero-span mode gives the sought exponential decay.

For the same single membrane mentioned in Sec. 3.3.4.3.1, a ringdown measurement at 1.646 MHz for (2,2) mode was done with RBW = 229 Hz at 10^{-7} mbar pressure which is shown in Fig. 3.28. The fit to that part of the spectrum gives $\tau_c = (167 \pm 1)$ ms and using Eq. (3.9) leads to $Q = (8.56 \pm 0.11) \times 10^5$. Performing successively multiple ringdowns yields an average $Q = (8.68 \pm 0.41) \times 10^5$, with a standard deviation larger than the individual fit errors. Ringdown spectroscopy has the advantage of being insensitive to slow thermal drifts, although the choice of the RBW and the fitting window may influence the results. In the case of low Q factor resonances, the ringdown spectroscopy cannot be performed, as a mechanical decay time faster than the PZT response time cannot be measured by this method.

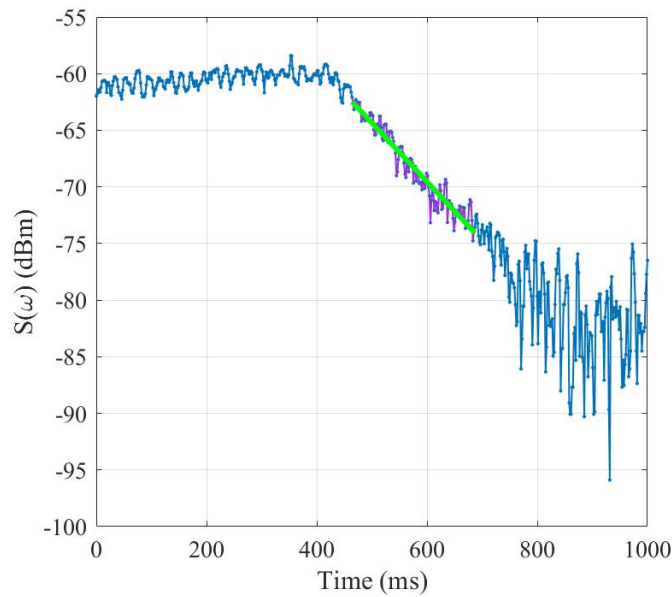


Figure 3.28: Ringdown spectroscopy of (2,2) mode of a single membrane with RBW = 229 Hz gives $\tau_c = (167 \pm 1)$ ms for this fit and $Q = (8.56 \pm 0.17) \times 10^5$.

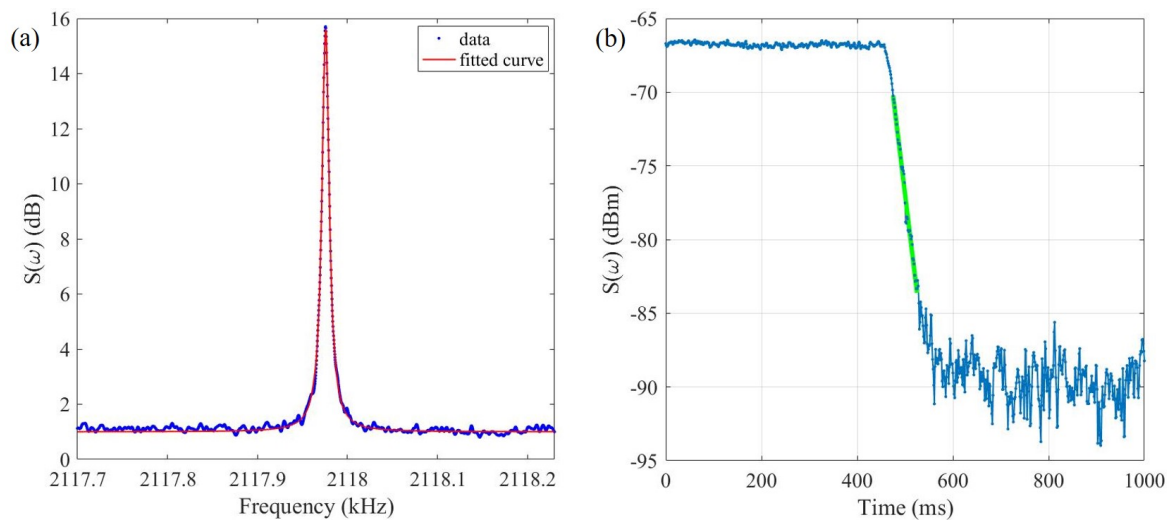


Figure 3.29: (a) The fit to thermal spectrum which gives $Q = (2.13 \pm 0.52) \times 10^5$ and (b) the ringdown spectroscopy of the same mode of a double-membrane array which gives $Q = (2.16 \pm 0.03) \times 10^5$.

The Q values calculated from both methods (fitting the thermal spectrum and ringdown spectroscopy) show results in reasonable agreement with each other and the deviation is likely due to the fact that recording the thermal spectrum is more

sensitive to the thermal drift which could underestimate the Q . Having a larger Q will increase this difference, which means that a reliable measurement of Q s above a million necessitates the ringdown spectroscopy method. However, for lower Q s, as it is illustrated in Fig. 3.29, the agreement between both methods is generally quite good. An example of a thermal spectrum of a double-membrane array recorded at RBW 0.5 Hz with 500 averages is shown in Fig. 3.29a in which the fit to the data points gives $Q = (2.13 \pm 0.52) \times 10^5$ and Fig. 3.29b presents the ringdown spectroscopy signal for the same mode which gives $Q = (2.16 \pm 0.03) \times 10^5$.

3.3.4.4 Effect of the resolution bandwidth

Practically, input voltage in the spectrum analyzer transforms to a voltage power spectrum and the power spectral densities are approximated by normalizing the measured power spectrum by its effective bandwidth. Therefore, the resolution bandwidth plays an important role in the recorded spectra. For a double-membrane array which was fabricated in the front-to-front geometry and having a spacer in between with $8.5 \mu\text{m}$ thickness, thermal noise spectrum of the fundamental mode of one of the membranes was recorded in different RBWs in the DPX display with 500 averages in order to be able to compare the results. Figure 3.30 shows the recorded thermal noise spectra in different RBWs 0.1, 0.2, 0.3, 0.5, 1, 2 and 3 Hz with an offset on top of each other to see the difference in data collection.

By doing Lorentzian fit to the measured spectra, the width and the energy in the mode could be deduced (see Fig. 3.31) and to compare the extracted values, each measurement in a specific RBW was repeated 5 times and a Lorentzian fit was done to each spectrum. The observed spread in the values being larger than the individual fit error, it is this error that was taken into account. While the energy in the mode (Fig. 3.31b) remains, as expected, rather independent of the RBW, the fit peak linewidth (Fig. 3.31a) has a minimum for a resolution bandwidth around 0.5 Hz. This might be expected, as too large an RBW does not allow to resolve the mechanical linewidth, and too low a linewidth increases the acquisition time and broadening due to thermal drifts.

Depending on the desired measurements (energy in the mode, linewidth), care has to be taken in choosing the RBW in general. Performing both thermal noise spectrum and ringdown spectroscopy measurements also allows to cross-check the consistency of the results.

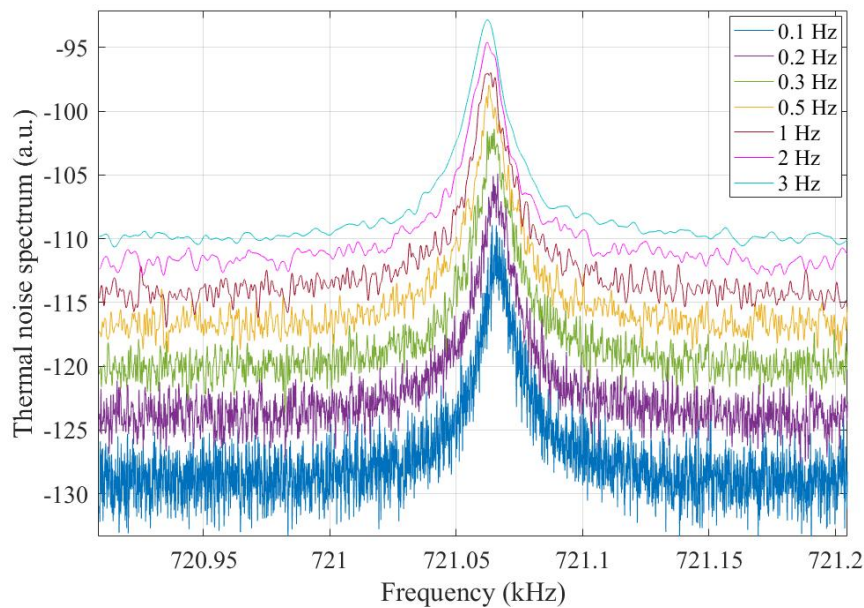


Figure 3.30: Thermal noise spectrum of the (1,1) mode of a membrane in a double-membrane array with a $500\ \mu\text{m}$ thick Si frame with the spacer in between with $8.5\ \mu\text{m}$ thickness. The spectra were recorded with 500 averages and in different RBWs.

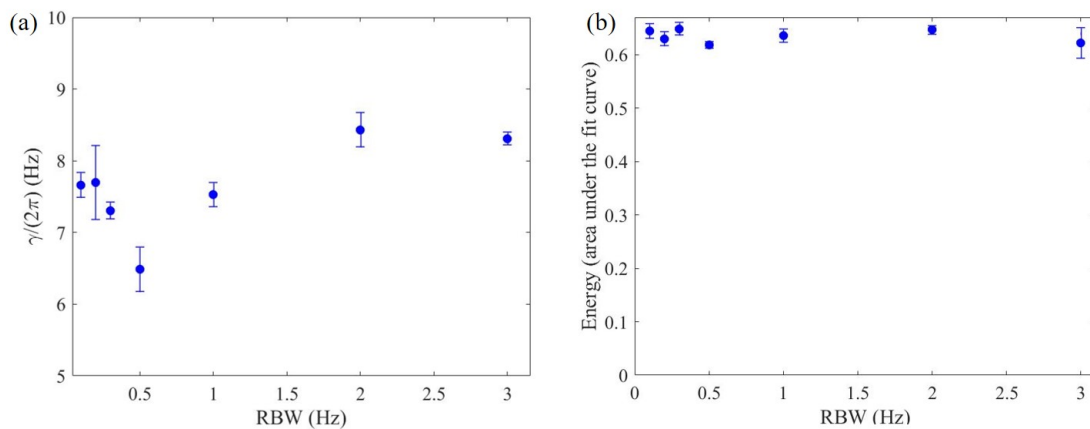


Figure 3.31: Extracted (a) $\gamma/(2\pi)$ (FWHM of the Lorentz fit) and (b) energy (area under the Lorentz fit) values for thermal (1,1) mode spectrum of a membrane in a double-membrane array with a $500\ \mu\text{m}$ thick Si frame with the spacer in between with $8.5\ \mu\text{m}$ thickness. The spectrum is recorded with 500 averages and repeated five times for different RBWs.

4

Pressure sensing with membrane sandwiches

The mechanical properties of the suspended SiN membranes are strongly dependent on their interaction with a surrounding fluid [33]. Their high-quality factors and small thickness/large area (nm/mm^2) make them well-suited resonators for pressure sensing applications. In general, in the free molecular flow regime, a suspended drum sandwich with compressed fluid inside its small gap experiences a squeeze film effect which can substantially modify mechanical resonance frequencies and dampings [36–41] and enables species-independent pressure measurements. Conventional miniaturized pressure sensors, such as capacitive or piezo-resistive sensors, are based on either a static determination of pressure by measuring the deflection of a suspended membrane due to a pressure difference with a reference cavity or dynamical changes in resonance frequencies [34] and typically operate from atmospheric pressure to low vacuum (millibar). For high and ultrahigh vacuum measurements, ionization gauge sensors commonly exhibit a high pressure sensitivity but require knowledge of the involved species and their ionization cross-sections. In contrast, squeeze film pressure sensors [33, 36, 50] –based on the dynamical modification of the mechanical properties of oscillating elements due to the compression of a fluid in a small gap region– allow in principle absolute and direct pressure measurements. The highest pressure responsivity in squeeze film MEMS pressure sensors reported has long been 200 Hz/mbar [43] until a higher responsivity in squeeze film pressure sensors based on thin graphene membrane has been recently reported by Dolleman et al. (9 kHz/mbar at down to mbar pressure and 1 kHz/mbar at atmospheric

pressure) [45].

This chapter presents a practical application of SiN membrane sandwiches as pressure sensors based on the results published in [85, 86], where the effects of pressure on the mechanical properties of SiN membrane sandwiches were studied. The chapter begins in Sec. 4.1 with a general discussion of the dynamics of plates oscillating in a fluid and introduces the hydrodynamics models required to interpret the experimental observations of Sec. 4.3. In Sec. 4.2, the experimental setup and the data collection procedure are explained. The chapter continues with the presentation of experimental data obtained with various membrane sandwiches and ends with a discussion of the potential of these sandwiches for absolute pressure sensing.

4.1 Effects of pressure on the mechanics

In the previous chapter, the mechanical properties (resonance frequencies and quality factors) of the membrane resonators were investigated in high vacuum ($10^{-6} - 10^{-7}$ mbar), where the interaction with the background gas molecules is essentially negligible. However, it is interesting to consider what happens to the mechanics at higher pressures. We start by a general discussion of the different regimes of the interaction of plates oscillating in a fluid in thermal equilibrium.

4.1.1 Knudsen number

We consider the oscillations of a plate with large transverse dimensions as compared to its thickness in a fluid at a given pressure. Different regimes for the dynamics of the resonator in the fluid can be distinguished based on the Knudsen number, which is the ratio of the gas molecule mean-free path and the typical structure dimension ($K_n = \frac{\lambda_{\text{mean free path}}}{L}$) (see Fig. 4.1).

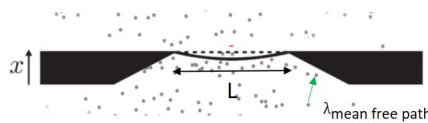


Figure 4.1: Schematic side view of a single-membrane resonator in a fluid in the free molecular regime.

High Knudsen numbers $K_n \geq 10$ correspond to the free molecular (or rarefied air) regime, in which the molecules experience collisions with the plate more often than with other molecules. In this regime the random kicks caused by the molecules

bouncing off the moving film lead to a friction force –kinetic damping– which is directly proportional to pressure [109]. At low Knudsen numbers, $K_n \leq 0.01$, the gas acts as a viscous fluid and damping becomes approximately independent of pressure [109, 110]. The range $0.01 \leq K_n \leq 10$ corresponds to a transition regime between the rarefied air and the viscous fluid regimes, in which neither a gas nor a viscous fluid treatment is in principle applicable [38]. Interestingly, for our membrane resonators operating in air at room temperature, the mean-free path of air molecules becomes of the order to the membrane dimension $a = 500 \mu\text{m}$ at pressures ~ 0.2 mbar.

For a membrane sandwich shown in Fig. 4.2a, which consists of two parallel thin clamped plates with lateral dimension a , thickness l and separated by a distance d , if the array is surrounded by air at ambient pressure P on all sides, the characteristic dimension to be taken into account is the intermembrane separation d rather its transverse extension a . The Knudsen number is then given by [109, 111, 112]:

$$K_n = \frac{k_b T}{\sqrt{2} \pi \sigma_{air}^2 P d}, \quad (4.1)$$

where $k_B = 1.38 \times 10^{-23} \text{ m}^2\text{kg}/(\text{s}^2\text{K})$ is the Boltzmann constant, T is the temperature and $\sigma_{air} = 4.9 \times 10^{-10} \text{ m}$ is the air molecule diameter.

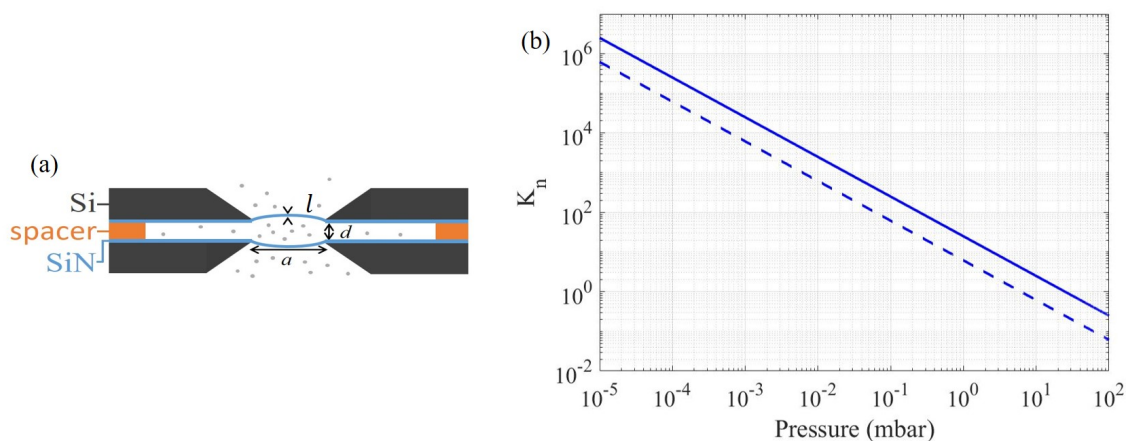


Figure 4.2: (a) Cross-section schematic of the membrane sandwich. [86] (b) Variations with pressure of the Knudsen number K_n for sandwiches with an inter-membrane separation d of $2.1 \mu\text{m}$ (solid line) and $8.5 \mu\text{m}$ (dashed line).

The variations of K_n in the pressure range $10^{-5} - 10^3$ mbar for two different arrays with the intermembrane separation d of $2.1 \mu\text{m}$ (solid line) and 8.5 (dashed line) μm are shown in Fig. 4.2b. As can be seen, the Knudsen number becomes

of order unity for pressures of order ten or a few tens of millibars, indicating the transition to the viscous fluid regime. For our resonators the rarefied air regime thus corresponds to pressures below ~ 1 mbar, the viscous fluid regime to pressures above $\sim 10^3$ mbar, and the transition regime occurs in the millibar range. [86]

In general, the Q factor of a mechanical oscillator is affected by all the sources of energy dissipation in the system, which could be loss mechanisms related to the coupling to the support structure, e.g. clamping losses, or external effects such as collisions with the fluid molecules [113].

In the rarefied air regime, the collisions of the air molecules with the membranes give rise to additional damping to the intrinsic damping provided by clamping losses discussed in the previous chapter. It was shown by Christian that this damping is proportional to the pressure and given by [110]:

$$\gamma_{air} = 4\sqrt{\frac{2}{\pi}}\sqrt{\frac{M_{air}}{RT}}\frac{P}{\rho l}, \quad (4.2)$$

where $\rho = 2700$ kg/m³ is the density of Si₃N₄ membrane, $M_{air} = 29$ g/mol is the molar mass of air, $R = 8.31$ J/(mol. K) is the ideal gas constant.

The total Q factor is then determined by the summation of the intrinsic damping at low pressure and the air damping:

$$Q = \frac{1}{(Q_i^{-1} + Q_{air}^{-1})}, \quad (4.3)$$

where Q_i is the intrinsic (vacuum) Q factor and $Q_{air} = \omega_m/\gamma_{air}$ is the contribution due to kinetic damping in the free molecular regime. For a membrane with thickness $l = 100$ nm and a fundamental mode oscillating at 800 kHz with a Q factor of 10^5 , the mechanical resonance is broadened by a factor 2 at pressures around 10^{-2} mbar at room temperature.

4.1.2 Squeeze film effect

For a membrane sandwich shown in Fig. 4.2a and in the free molecular regime, the presence of the second membrane changes the compression of the gas in between the membranes. Such a compression, if isothermal, produces an additional force on the membranes [40, 114], called squeeze film force, which we now discuss based on the study in [39].

In the free molecular regime, the movements do not happen instantaneously and a more relevant quantity to discuss the nature of the trapping of the fluid is the product $\omega\tau$ of the mechanical frequency by the molecular diffusion time which is the time constant for equalizing the pressure inside and outside the gap [37]. The relaxation time corresponds to the average time it takes the molecules to leave the gap, which can be estimated by:

$$\tau = \frac{8a^2}{\pi^3 d \bar{v}}, \quad (4.4)$$

where $\bar{v} = \sqrt{8RT/\pi M_{air}}$ is the mean velocity of the air molecules. The relaxation time can be increased by decreasing the gap size comparing to the lateral dimensions [115]. The variation of the gas density $\Delta n(t)$ inside the gap between one moving plate and one fixed plate is given by

$$\frac{d}{dt} \frac{\Delta n}{n} = -\frac{1}{\tau} \frac{\Delta n}{n} - \frac{d}{dt} \frac{z}{d}, \quad (4.5)$$

where n is the density equilibrium value and z is the coordinate pointing up from the plate ($z = 0$ corresponds to equilibrium position). This equation describes the rate of change of the density driven by the displacement of the moving plate, counteracted by the random walk of the molecules in the gap.

Assuming a forced membrane oscillation with (complex amplitude) displacement $z(t) = z_0 e^{i\omega t}$ and a trial solution $\Delta n(t)/n = (\Delta n_0/n) e^{i\omega t}$, one can obtain

$$\frac{\Delta n(t)}{n} = -\frac{z(t)}{d} \frac{i\omega\tau}{i\omega\tau + 1}. \quad (4.6)$$

Therefore, in case of isothermal density variations, the resulting force on the membrane for increased pressure $\Delta P(t)$ in the gap is

$$F_{squeeze} = \Delta n(t) k_B T a^2 = \Delta P(t) a^2. \quad (4.7)$$

Using Eqs. (4.6) and (4.7), one can calculate

$$F_{squeeze} = -\frac{Pa^2}{d} \frac{i\omega\tau}{i\omega\tau + 1} z, \quad (4.8)$$

as the squeeze force of the gas on the moving membrane which has both a real and an imaginary part. The real component is in phase with the amplitude z and contributes to modifying the natural spring constant of the mode, whereas the imaginary part is out of phase with the amplitude z and contributes to adding dissipation via the gas molecules to the natural dissipation via the coupling with the frame (squeeze film damping) [39, 40, 114]. Therefore, the differential equation for the complex amplitude $z(t)$ is given by

$$m\ddot{z} + m\gamma_t\dot{z} + k_t z = F_0 e^{i\omega t}, \quad (4.9)$$

in which $\gamma_t = \gamma + \gamma_{squeeze}$ and $k_t = m\omega^2 + k_{squeeze}$ with

$$k_{squeeze} = \frac{Pa^2}{d} \frac{(\omega\tau)^2}{1 + (\omega\tau)^2}, \quad (4.10)$$

$$\gamma_{squeeze} = \frac{Pa^2\tau}{md} \frac{1}{1 + (\omega\tau)^2}. \quad (4.11)$$

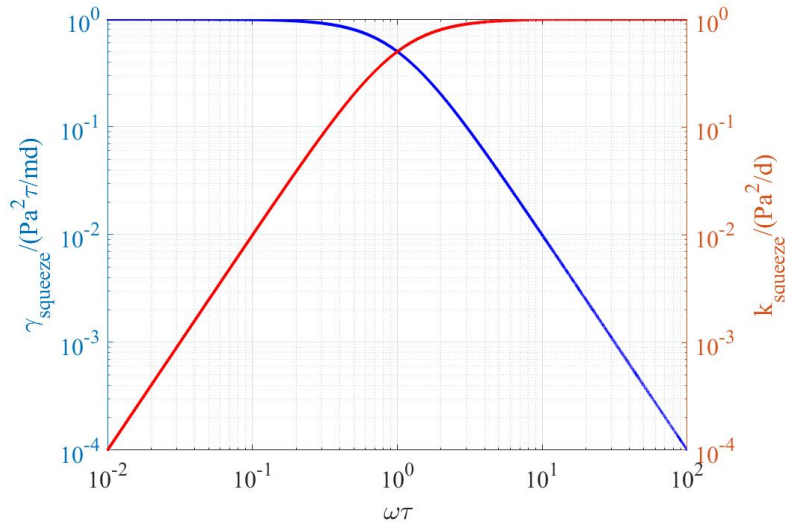


Figure 4.3: Frequency dependence of the squeeze film damping and spring constant.

Figure 4.3 illustrates the frequency dependence of the squeeze film damping and spring constant. In general, for a fluid with a relaxation time τ interacting with a resonator with frequency ω , the Newtonian hydrodynamics assumption that the fluid remains in the vicinity of equilibrium is valid when the Weissenberg number, $W_i = \omega\tau$, is much larger than unity [116]. Thereby as can be seen in Fig. 4.3, for high oscillation frequencies $\omega\tau \gg 1$, only the spring constant is modified by the squeeze film effect, while for low oscillation frequencies $\omega\tau \ll 1$, the squeeze film force is dissipative. The resonance frequency of our membrane modes is in MHz range, which typically puts our resonators in the high frequency regime. Using Eqs. (4.2), (4.4) and (4.11), the ratio of the kinetic damping to the squeeze film damping is then $16Ma^2\omega^2/(\pi^3RT) \sim 60$ for $\omega/(2\pi) = 1$ MHz and $a = 500 \mu\text{m}$, and one can expect the squeeze film to be negligible. Therefore, we expect $\gamma_{squeeze} \ll \gamma_{kin}$ and the squeeze film damping should be negligible with respect to the kinetic damping

in the situations considered here.

In the viscous regime, the fluid compressibility in the gap is determined by the dimensionless squeeze number σ which is used to characterize the fluid behavior [117] depending on its viscosity μ . The relative strengths of the elastic and damping forces depend on the σ [41]:

$$\sigma = \frac{\pi P d^2}{24 \mu a^2}. \quad (4.12)$$

The ratio of the in-phase and out of phase components of the squeeze film force coming from the fluid compression depends on the squeeze number. At low squeeze numbers, the squeeze film force is out of phase and the compressibility effects are negligible, which results in extra damping, but negligible frequency shift. At high squeeze numbers, the force is mostly in-phase and the trapped fluid does not have time to exit the gap where it is compressed. The squeeze film then results in a mechanical frequency shift, but negligible extra damping. [114, 117]

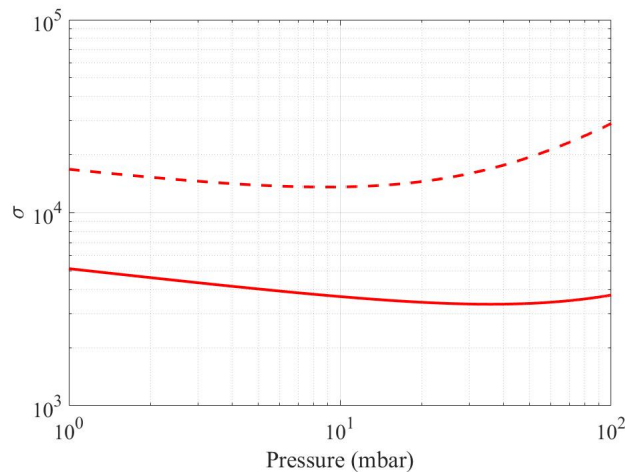


Figure 4.4: Variations of the squeeze parameter σ with pressure for sandwiches with an intermembrane separation d of $2.1 \mu\text{m}$ (solid line) and $8.5 \mu\text{m}$ (dashed line).

In Fig. 4.4, the variation of the σ for two different membrane sandwiches with the intermembrane separation d of $2.1 \mu\text{m}$ (solid) and $8.5 \mu\text{m}$ (dashed) is shown in the pressure range $10^{-5} - 10^3$ mbar. The empirical effective viscosity for the air $\mu_{eff} = \mu_0 / (1 + 9.658 K_n^{1.159})$, where $\mu_0 = 1.8 \times 10^{-5}$ Pa is the air viscosity at atmospheric pressure, was used [41]. As it can be seen, $\sigma \approx 10^3 - 10^4$ in the pressure range $1-10^2$, mbar which means that we expect to have an elastic squeeze film force in the whole pressure range of study.

4.1.3 Squeeze film dynamics in the rarefied air regime

As discussed above, in the free molecular regime and in the high frequency limit, for a large oscillating plate lying close to a fixed plate, the air-added spring constant (due to the squeeze film effect) $\kappa_{air} = \frac{k_{squeeze}}{m}$ is proportional to the pressure and results in a frequency shift of the plate mechanical resonance frequency shift given by the expression:

$$\tilde{\omega}^2 = \omega^2 + \kappa_{air} = \omega^2 + \frac{P}{\rho l d}. \quad (4.13)$$

In this study, we consider the vibrations of two parallel clamped membranes in the direction orthogonal to their plane (x-direction, see Fig. 4.1) and denote by x_1 and x_2 the amplitudes of two corresponding normal modes with frequencies ω_1 and ω_2 and intrinsic dampings (in vacuum) γ_1 and γ_2 , respectively. If only one membrane, say 1, was oscillating while the other was fixed, the equation of motion for the normal mode considered would be:

$$\ddot{x}_1 + (\gamma_1 + \gamma_{air})\dot{x}_1 + \omega_1^2 x_1 + \kappa_{air} x_1 = F_{th1} + F_{air1} \quad (4.14)$$

where γ_{air} is given by Eq. (4.2) and F_{th1} and F_{air1} are the noise forces associated to the thermal fluctuations and the collisions with air molecules.

In case of a double-membrane array consisting of two parallel and nearly identical membranes, the squeeze film forces are opposite on each membrane, resulting in the coupled dynamical equations:

$$\ddot{x}_1 + (\gamma_1 + \gamma_{air})\dot{x}_1 + \omega_1^2 x_1 + \kappa_{air}(x_1 - x_2) = F_{th1} + F_{air1} \quad (4.15)$$

$$\ddot{x}_2 + (\gamma_2 + \gamma_{air})\dot{x}_2 + \omega_2^2 x_2 + \kappa_{air}(x_2 - x_1) = F_{th2} + F_{air2}, \quad (4.16)$$

with F_{th2} and F_{air2} the noise forces for mode 2. Note that, in writing Eqs. (4.15) and (4.16), we assumed that modes 1 and 2 have similar frequencies and neglected the contributions due to other vibrational modes, whose frequencies were assumed to be very different and whose off-resonant contributions to the frequency shifts of modes could then be neglected, as is discussed below.

The dynamics of the pressure-coupled modes 1 and 2, and thereby their thermal noise spectra, depend on the relative strength of the air-induced coupling, the frequency separation between the modes and their respective (pressure-dependent) dampings. As it was shown in Sec. 2.1.3, in the good oscillator limit –i.e. assuming that the Q factors remain large over the pressure range considered– the frequencies of the normal modes can be found by analyzing the Fourier transforms of Eqs. (4.15) and (4.16) and are given by

$$\omega_{\pm} = [\omega_0^2 + \delta^2 + 2\eta\omega_0 \pm 2\omega_0\sqrt{\delta^2 + \eta^2}]^{1/2} \quad (4.17)$$

where

$$\omega_0 = (\omega_1 + \omega_2)/2, \quad \delta = (\omega_1 - \omega_2)/2, \quad \eta = \kappa_{air}/(2\omega_0). \quad (4.18)$$

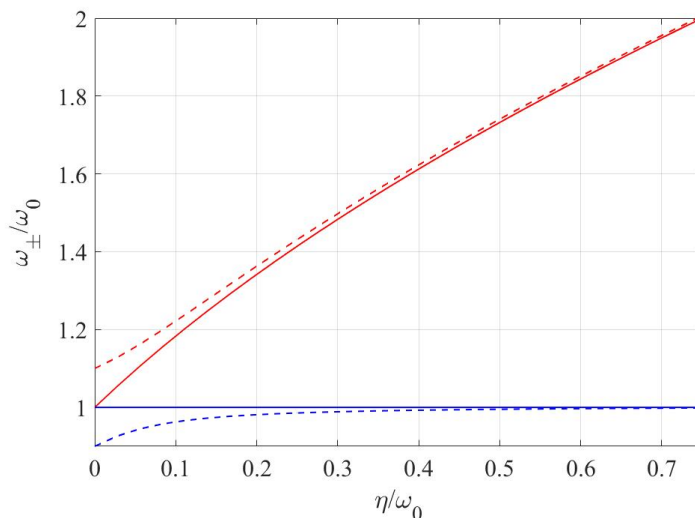


Figure 4.5: Normal mode frequency ω_+ (red) and ω_- (blue) as a function of coupling η (in units of ω_0) in case of $\delta = 0$ (solid lines) and $\delta = 0.08\omega_0$ (dashed lines). Blue and red represent ω_+ and ω_- , respectively.

And as it was presented in Sec. 2.1.3, the frequency shifts, $\delta\omega_{\pm} = \omega_{\pm} - (\omega_0 \pm \delta)$, are affected by the air-induced coupling η (proportional to the pressure) variation. Figure 4.5 illustrates the variations of the frequency shifts (ω_+ in red and ω_- in blue) as a result of different values for η for two cases of $\delta = 0$ (solid lines) and $\delta = 0.08\omega_0$ (dashed lines). In the case of $\delta = 0$, the bright mode experiences a doubled frequency shift 2η , which is doubled as compared to what a single membrane coupled to a fixed plate would experience, while the dark mode does not experience any frequency shift. However, for a nonzero frequency separation δ , both modes experience the same positive frequency shift η as long as $\eta \ll \delta$, until the point where $\eta \sim \delta$ and the mode hybridize and the same behavior as discussed in the $\delta = 0$ case is observed.

4.2 Experimental setup

In order to characterize the mechanical properties of the assembled arrays, the setup introduced in Sec. 3.3.4.1 was used and it is summarized in Fig. 4.6. The

samples were lying inside a 450 cm³ vacuum chamber on a ring-shaped mount where the corners of the lower chip were resting on the ring. A 50:50 beamsplitter (BS), placed approximately 7 mm away from the sample, formed a linear Fabry Perot interferometer whose length was adjustable with a piezoelectric transducer (PZT). The length of the interferometer could be adjusted so as to maximize the displacement sensitivity (typically close to the interference signal midfringe) and a monochromatic light coming from a tunable external cavity laser diode (~900 nm) entered perpendicularly on the formed interferometer. The transmission of monochromatic light was recorded with a fast photodiode and the fluctuations of the photocurrent were analyzed using a low-resolution bandwidth spectrum analyzer.

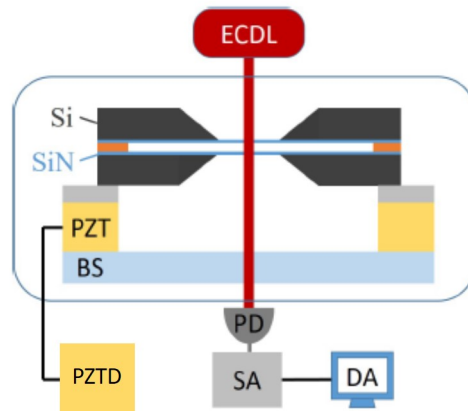


Figure 4.6: Schematic of the optomechanical characterization setup. ECDL: external cavity diode laser, PZT: piezoelectric transducer, BS: beamsplitter, PD: photodiode, SA: spectrum analyzer, PZTD: PZT driver, DA: data analysis. [86]

The data collection process included Q factor measurements which were done by the ringdown spectroscopy or Lorentzian fit to the thermal noise spectrum as well as frequency shift and broadening of mechanical mode which were determined by the thermal noise spectrum. The thermal noise spectra were typically recorded over a span range of a few to a few hundreds of kilohertz with a resolution bandwidth (RBW) of 0.5 Hz and averaged 500 times in DPX display of the spectrum analyzer.

We observed thermal drifts for the resonance frequencies during the data collection process due to the fact that the vacuum chamber temperature was not being actively stabilized. The measured thermal drifts were typically a few tens of hertz per hour. These shifts did not have a significant effect on measurements at high pressures. However, in order to compensate the thermal drifts during sensitive data

collection at low pressures, the resonance frequency drifts were corrected during long acquisition time measurement series by recording a reference spectrum at a pressure lower than 10^{-5} mbar for different data points in time.

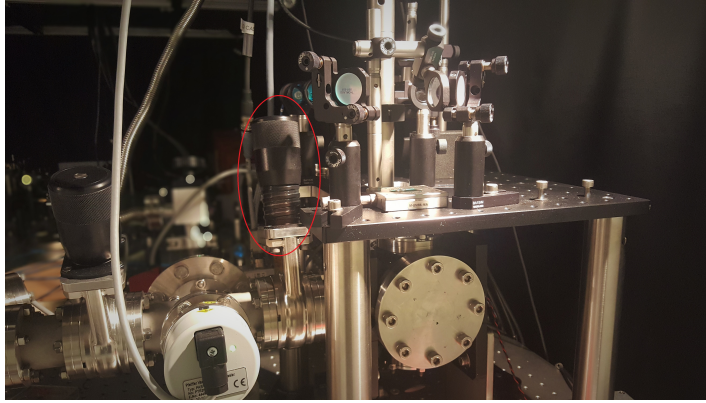


Figure 4.7: Picture of the setup including the valve (in a red circle) which controls the pressure inside the chamber.

The pressure in this setup was controlled by opening the valve to the chamber shown in Fig. 4.7 and measured using an ion gauge sensor (PKR 251). The pressure measurements were also checked with two other sensors, a compact piezo gauge (APR 250) a compact Pirani gauge (TPR 280), which is shown in Fig. 4.8 where the points recorded by our sensor are plotted against the two other ones. The pressure measurements could be calibrated against APR 250 whose air pressure responsivity was absolutely calibrated in the range 1-50 mbars [118]. The calibrated piezo sensor response is accurate to within a few percent in that range and its response is used to calibrate that of the measuring ion gauge sensor over the whole pressure range.

4.3 Experimental results

4.3.1 Effects of pressure on "medium" arrays

This section focuses on the investigation of the effect of pressure on the Q factor and the frequency of the fundamental modes of $8.5 \mu\text{m}$ -long membrane arrays shown in Fig. 4.9b in the range 10^{-6} -10 mbar [85].

The arrays used in this study were made from two $(0.5 \times 0.5) \text{ mm}^2$, 92 nm-thick, high-tensile stress ($\sim 0.9 \text{ GPa}$) SiN membranes deposited on $(5 \times 5) \text{ mm}^2$, $500 \mu\text{m}$ -

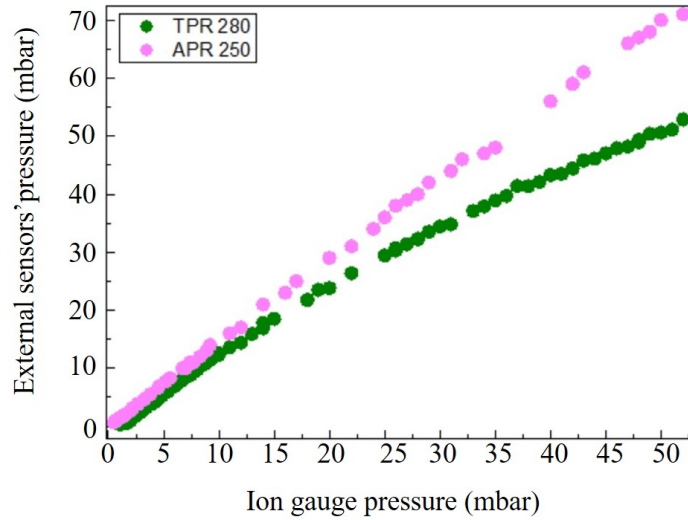


Figure 4.8: Pressure measurements using two external sensors, a piezo gauge (purple) and a Pirani gauge (green), against the ion gauge sensor that is used in our experimental setup.

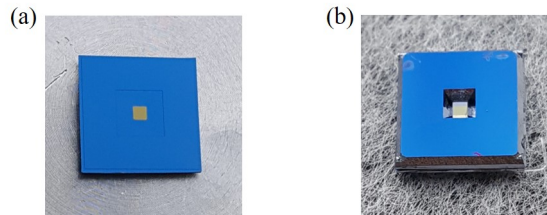


Figure 4.9: Pictures of (a) a commercial chip with a $8.5 \mu\text{m}$ spacer deposited on SiN film and (b) a "medium" array made in the front-to-front geometry with $d = 8.5 \mu\text{m}$.

thick Si frames. The chips were separated by an $8.5 \mu\text{m}$ spacer (Fig. 4.9a) in the front-to-front geometry by the 1st generation assembly technique including the preselection process and optimizing the parallelism using a white light source. The arrays were then glued together from the sides to form "medium" d arrays (Fig. 4.9b).

To characterize the fluid behavior for this arrays, the values for σ and W_i were considered in different regimes. Since the Knudsen number is here of order unity at \sim mbar pressures, the dynamics happen in the transition regime between the free molecular and the viscous regimes. At atmospheric pressure, $\sigma \sim 40$, which suggests an essentially elastic squeeze film force and negligible squeeze film damping. Moreover, in the free molecular regime $W_i = \omega\tau \sim 80$, also predicting an essentially elastic squeezed film force in this regime. Therefore, we do not include any extra

damping due to the squeeze film effect in the theoretical predictions for these arrays.

Figure 4.10 shows the variations with pressure of the mechanical quality factor of the fundamental mode for a single membrane in gray crosses and for the double-membrane array in red triangles. The membranes have similar fundamental frequencies (718.4 kHz and 721.8 kHz) and intrinsic quality factors (1.8×10^5 and 1.2×10^5). The Q-factors were measured by ringdown spectroscopy in the range of $10^{-6} - 10^{-1}$ mbar or by Lorentzian fits to the thermal noise spectrum in the range of $10^{-2} - 10$ mbar. While at low pressures (below 10^{-1} mbar) ringdown spectroscopy provided a more accurate determination of the quality factors, the faster decay times prevented its use at higher pressures. The thermal noise spectra, broadened as compared to high vacuum, were in contrast more resilient to thermal drifts and were used to determine the quality factors. Both methods were found to agree well in the range $10^{-2} - 10^{-1}$ mbar.

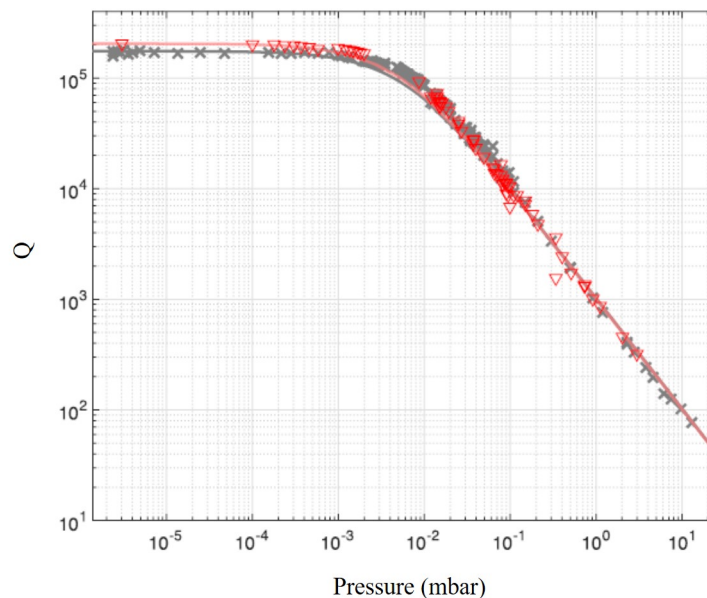


Figure 4.10: Variation of the fundamental mode mechanical quality factor with pressure for a single resonator (crosses) and a double-membrane resonator (triangles). The lines show the theoretical predictions including intrinsic and kinetic damping. [85]

As it is presented, at low pressures, the Q factor is constant dissipation is dominated by the intrinsic damping, whereas, at high pressures, the quality factor decreases as $1/P$ [85]. These variations of the Q factor due to pressure change are well-reproduced by the theoretical predictions given by Eq. (4.3). Both the single membrane and the double-membrane array are seen to experience the same

damping which means that the kinetic damping is enough to explain the results.

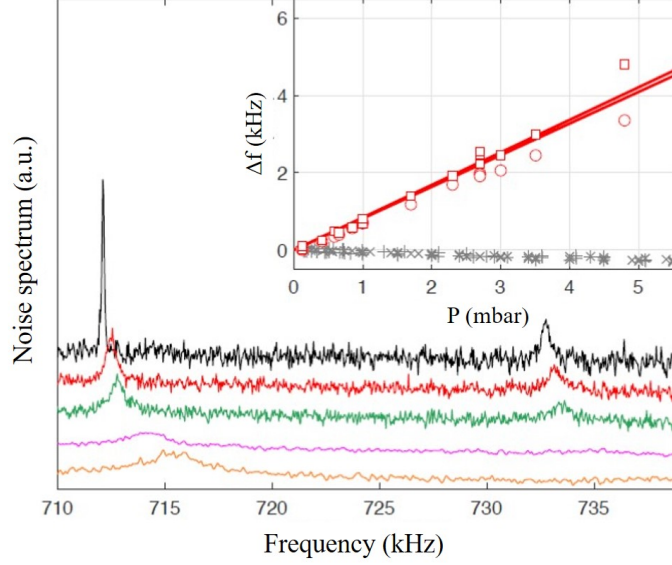


Figure 4.11: Noise spectra at different pressures 0.18 to 5.1 mbar from top to bottom (the spectra are offset vertically for visibility) for a double-membrane resonator with well-separated frequency modes. The inset shows the resonance frequency shifts as a function of pressure for single membranes (crosses) and the membranes of an array (circles and squares). The lines show the results of the squeeze film predictions. [85]

In order to study the frequency shift of a vibrational mode due to the pressure variation, Lorentzian fit to the noise spectrum was used to determine the resonance frequencies at a given pressure and the shift was then measured with respect to the low-pressure value. Figure 4.11 shows typical vibrational mode spectra of well-separated fundamental modes of the $8.5 \mu\text{m}$ double-membrane array at different pressures, as well as the variations of the resonant frequency of the fundamental mode with pressure for both single membrane and double-membrane array.

For a single membrane, a small frequency shift $\Delta f/P = -50 \text{ Hz/mbar}$ was observed, in accordance with the fact that the effective mass of the displaced fluid has to be added to the resonator mass (the shift due to the decrease in Q factor is still negligible at these pressures). In contrast, the double-membrane array's fundamental modes at 712 and 733 kHz exhibited much larger and positive linear frequency shifts as the pressure was increased. The expected frequency shifts

$$\Delta f \simeq \frac{P}{8\pi^2 \rho l d}. \quad (4.19)$$

of 842 and 818 Hz/mbar are corroborated by the experimental observations.

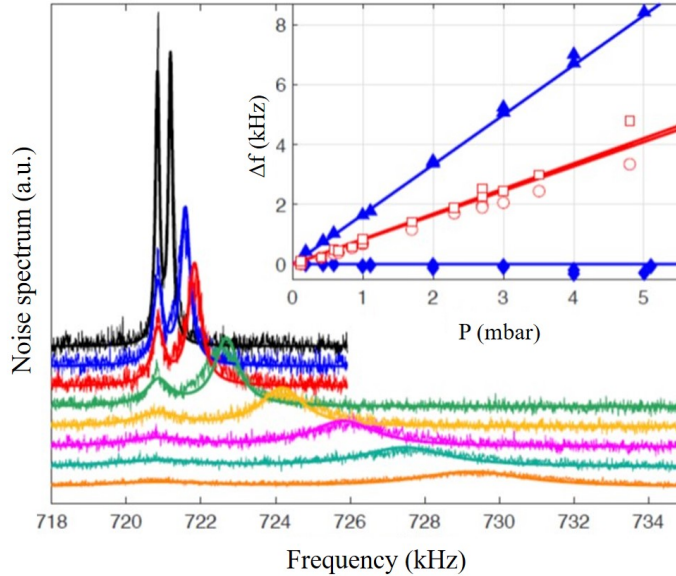


Figure 4.12: Noise spectra at different pressures 0.18 to 5.1 mbar from top to bottom (the spectra are offset vertically for visibility) for a double-membrane resonator with near degenerate frequency modes. The solid lines show the result of a global fit to the theoretical model. The inset shows the hybridized mode frequency shifts as a function of pressure (full symbols), while the frequency shifts for the resonator with well-separated frequency modes are shown for comparison. [85]

The results presented so far illustrated the case of membranes with well-separated fundamental modes. Interestingly, due to the high degree of uniformity exhibited by membranes from the same fabrication batch, several of the assembled arrays displayed near-degenerate frequency modes. In that case, not only does the gas modify mechanical damping and resonant frequencies, but also couples the vibrational modes of each membrane when the air-induced shift becomes of the order of the mode frequency separation. Figure 4.12 shows typical noise spectra of a double-membrane array for which the fundamental modes of each membrane are separated by 0.2 kHz in vacuum which we refer to as a near-degenerate case. As the pressure is increased, the modes are clearly seen to hybridize into a “dark” mode whose spring constant remains essentially unchanged and a “bright” mode whose spring constant is effectively doubled as compared to the non-interacting mode scenario.

The measured noise spectrum thus corresponds to that of an a priori unknown linear combination of the membrane displacements $a[\cos(\theta)x_1 + \sin(\theta)x_2]$, where

x_1 and x_2 are obtained by solving Eqs. (4.15) and (4.16) in the Fourier domain and calculating the noise spectrum as described in Sec. 2.1.2.1. This combination depends on the modematching of the interferometer, the overlap between the optical beam and the mechanical modes, the distances between the mirrors, and the operating wavelength. The results of a global fit with the model, with a and θ as free parameters and with γ_{air} and k_{air} as given by the theoretical predictions, are shown in Fig. 4.12 and are seen to well reproduce the measured spectra. In addition to that, the independently measured resonance frequency shifts from Lorentzian fits to the spectra shown in the inset of Fig. 4.12 are likewise in good agreement with the theoretically expected shifts of $\simeq 0$ and 1664 Hz/mbar.

To conclude, squeeze film effects in a "medium" d double-membrane arrays have been investigated in the molecular and quasi-molecular regimes and squeeze film-induced hybridization between modes of distinct resonators has been observed. For very non-degenerate resonance frequencies, as the pressure was increased, the damping was found to be essentially of kinetic origin, while the compressibility of the fluid was observed to add a positive mechanical spring constant which was proportional to pressure. Therefore, they behaved independently and their mechanical resonance frequencies were shifted by a nearly equal amount at a given pressure. In the case of membranes with near-degenerate mode frequencies, hybridization of the vibrational modes of both membranes was observed and normal "bright" and "dark" modes had to be introduced.

The experimental observations in this study were in good agreement with theoretical predictions and allowed us to demonstrate the physical mechanisms behind the workings of membrane sandwiches as pressure sensors. In order to increase the magnitude of the squeeze film effects, the intermembrane separation was subsequently reduced using the new assembly method (second generation arrays in the front-to-front geometry).

4.3.2 Effects of pressure on "short" arrays

In this section, we discuss on the realization of squeeze film pressure sensors based on suspended, high-mechanical Q ($\sim 10^5$) SiN membranes forming a small gap double-membrane arrays with $d = 2.95 \mu\text{m}$ and $d = 2.1 \mu\text{m}$ and characterize the modifications of their mechanical properties in air in the range $10^{-3} - 50$ mbar [86].

The arrays used in this study were made with the same assembly technique introduced in Chap. 3 (second generation) in the front-to-front geometry forming few micron cavities in the "short" d category. These double-membrane array were

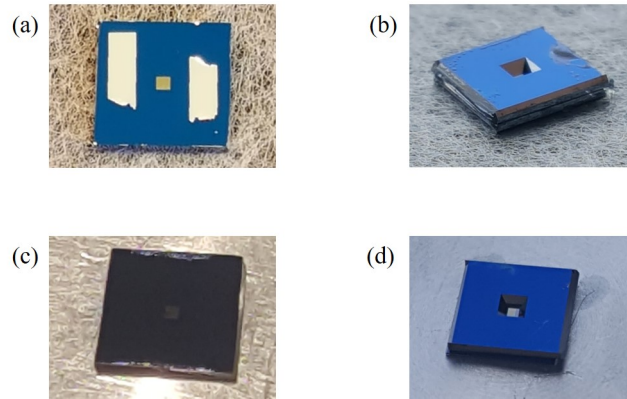


Figure 4.13: Pictures of (a) a commercial chip with Al spacer deposited on SiN film, (b) a short array with $d = 2.95 \mu\text{m}$ including Al spacer, (c) a commercial chip with two thin lines of UV resist spacer on SiN film and (d) a short array with $d = 2.1 \mu\text{m}$ array including UV resist spacer.

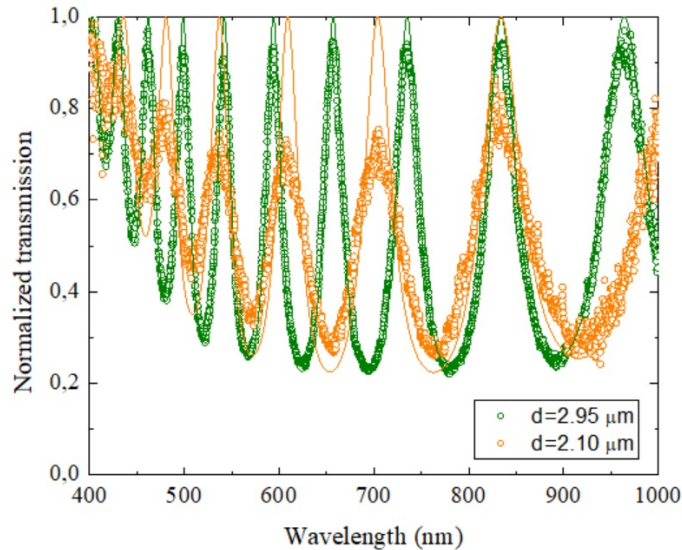


Figure 4.14: Normalized transmission spectra of membrane sandwiches in Fig. 4.13 with $d = 2.95 \mu\text{m}$ (green) and $d = 2.10 \mu\text{m}$ (orange) under broadband illumination. The solid lines indicate the results of fits with the theoretical model discussed in Chap. 2 (Eq. (2.84)). [86]

made from two $(0.5 \times 0.5) \text{ mm}^2$, 87 nm-thick, high-tensile stress ($\sim 0.9 \text{ GPa}$) SiN membranes deposited on $(5 \times 5) \text{ mm}^2$, 500 μm -thick Si frames. In the first array shown in Fig. 4.13b, two rectangular 1 μm -thick aluminum spacers ($0.5 \times 1 \text{ mm}^2$) were deposited onto one chip about 1 mm from the suspended membrane (Fig. 4.13a). Small dabs of UV resist (OrmoComp, Micro resist technology GmbH) were deposited on the sides of the frame and the resist cured when reasonable parallelism

was achieved which led to $d = 2.95 \mu\text{m}$. For the second array shown in Fig. 4.13d, two thin lines of UV resist were deposited close to two edges of the lower chip played the role of a flexible spacer (Fig. 4.13c) and cured at the final stage which gave $d = 2.10 \mu\text{m}$.

Figure 4.14 shows the normalized optical transmission spectra of both short d arrays under the broadband illumination in the range 400-1000 nm and in air. The solid lines are the result of fits to the theoretical model of a linear Fabry Perot etalon introduced in Chap. 2 (Eq. (2.84)), which takes into account the refractive index of SiN. From these fits the intermembrane separation d and the membrane thickness $l = 87(1)$ nm can be accurately determined. The reduced contrast in the interference fringes of these arrays is attributed to a rather poor degree of parallelism (estimated tilt angle ~ 2 mrad) achieved after the "short" arrays' assembly which has bearings on the squeeze film effect for this sample, as will be discussed later.

As previously, it is possible to characterize the fluid behavior for these membrane sandwiches by considering $d = 2.1 \mu\text{m}$ and a fundamental mode frequency $\omega = (2\pi)820$ kHz, which leads to $W_i \simeq 340$ and means that the squeeze film force is expected to be elastic in the rarefied air regime. Moreover, we can use the empirical effective viscosity of [41] and get $\sigma = 3600$ for $d = 2.1 \mu\text{m}$ and $P = 10$ mbar (see also Fig. 4.4). Thereby we can again reasonably expect to have an elastic squeeze film force for these double-membrane arrays in the whole pressure range considered in this work.

4.3.2.1 2.95 μm double-membrane array

The characterization of the mechanics of the Al-spacer array in high vacuum revealed that one of the membranes had modes with reasonably high Q factors (membrane 2) whereas the other membrane modes had substantially reduced Q factors (membrane 1) which could be the result of the Al deposition or manipulation in the course of the deposition process. The fundamental (1,1) mode frequencies of both membranes were $\omega_1/(2\pi) = 824.1$ kHz and $\omega_2/(2\pi) = 826.7$ kHz, and their intrinsic quality factors $Q_1 = 1500$ and $Q_2 = 65000$, respectively. Some examples of thermal noise spectra for these modes for different pressures are shown in Fig. 4.15 in which positive frequency shifts and broadening of the spectra with increasing pressure are clearly observed for both modes. Due to its lower Q factor the thermal fluctuations of membrane 1's fundamental mode are no longer resolved for pressures above 0.3 mbar, however, in contrast, membrane 2's thermal fluctuations could be resolved up to much higher pressures (see Fig. 4.16).

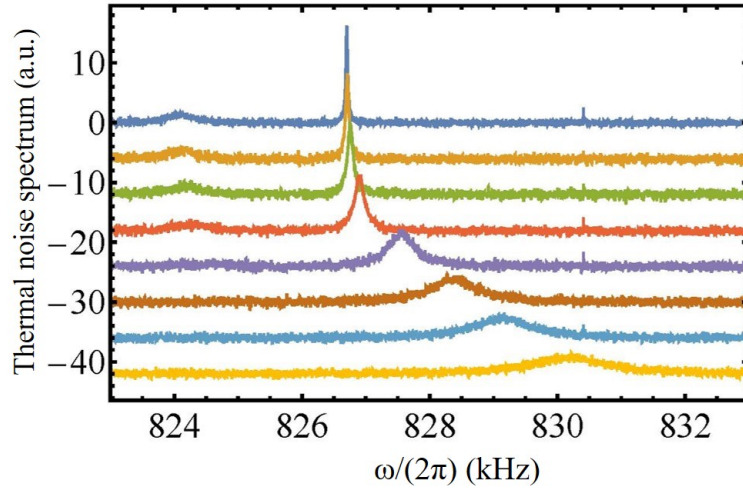


Figure 4.15: Thermal noise spectra for $2.95 \mu\text{m}$ array around the fundamental mode frequencies for different pressures (from top to bottom: $P = 5 \times 10^{-8}, 0.018, 0.055, 0.13, 0.35, 0.6, 0.82, 1.05$ mbar). The background-subtracted spectra are shown with a logarithmic scale and vertically offset for clarity. [86]

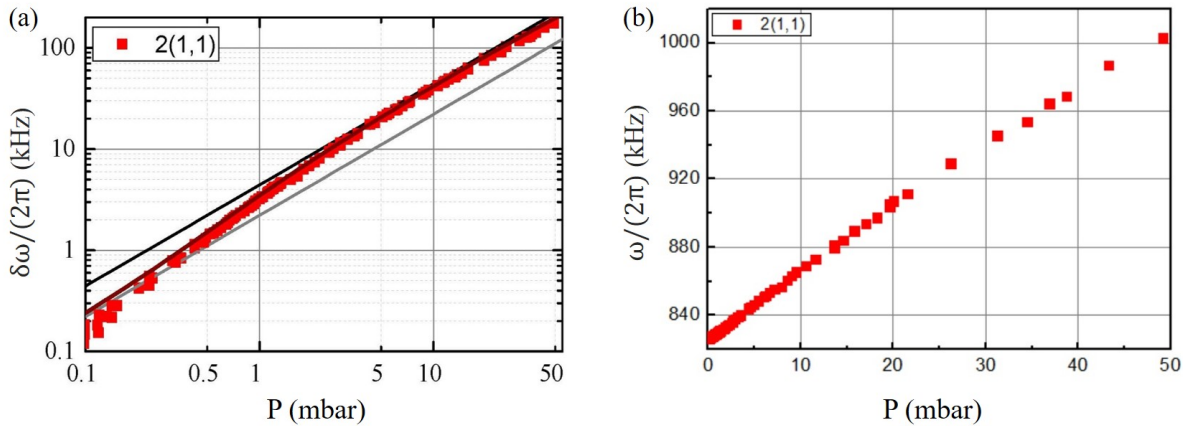


Figure 4.16: (a) Resonance frequency shift of membrane 2's fundamental mode as a function of pressure (logarithmic scale). The solid lines show the predictions of the squeeze film model (red), as well as the single- and double-linear shifts (gray and black, respectively). [86] (b) Resonance frequency of membrane 2's fundamental mode as a function of pressure (linear scale).

To study the effect of pressure on the resonance frequency of the mechanical modes of this sandwich, the thermal noise spectrum of the fundamental mode of membrane 2 was recorded in the pressure range 10^{-3} -50 mbar and the frequency shifts were extracted from Lorentzian fits to thermal noise spectra as shown above.

Figure 4.16 shows the variations with pressure of the resonance frequency shift of membrane 2's fundamental mode, denoted by 2(1,1) (where 2 stands for membrane 2 and (1,1) for $m = n = 1$) in both logarithmic (Fig. 4.16a) and linear (Fig. 4.16b) scales. The observed frequency shifts are in good agreement with the predictions of the coupled-oscillator squeeze film model given the measured intermembrane separation $d = 2.95 \mu\text{m}$. The resonance frequency shift for this mode was measured as high as 176 kHz at 50 mbar. The crossover from independent to coupled modes predicted by the squeeze film model discussed in Sec. 4.1.2 is also clearly visible, resulting in a pressure responsivity of almost 4 kHz/mbar in the range 2-20 mbar.

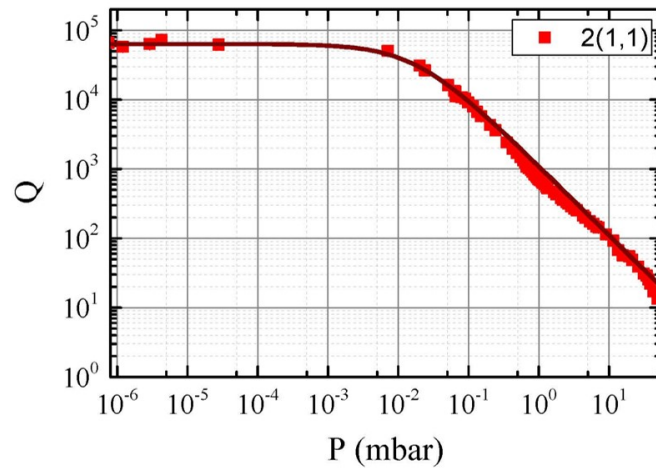


Figure 4.17: The mechanical quality factor of membrane 2's fundamental mode as a function of pressure (logarithmic scale). The solid line shows the kinetic damping predictions. [86]

The variations of membrane 2's Q factor with pressure were also extracted from Lorentzian fits to thermal noise spectra which are shown in Fig. 4.17. The measured quality factors were observed to be in good agreement with the kinetic damping predictions, confirming that extra damping due to the essentially elastic squeeze film force is negligible with respect to kinetic damping.

In order to verify these observations, the effects of pressure on the resonance frequency and the damping rate of two higher-order modes, the (1,2) mode with a frequency of 1306 kHz and intrinsic Q of 2.4×10^4 and the (2,3) mode with a frequency of 2108 kHz and intrinsic Q of 3.83×10^5 , were also investigated. As is clearly seen from Fig. 4.18, the frequency shift responsivity is inversely proportional with the resonance frequency, as expected from the squeeze film model predictions ($\eta \propto 1/\omega_0$, see Eq. (4.18)).

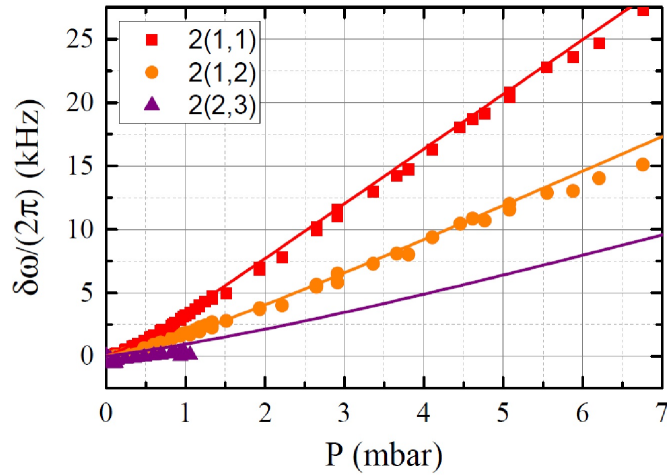


Figure 4.18: Resonance frequency shift for three modes of membrane 2 as a function of pressure (logarithmic scale). Red squares: (1,1) mode, orange circles: (1,2) mode, purple triangles: (2,3) mode. The solid lines show the theoretical predictions. [86]

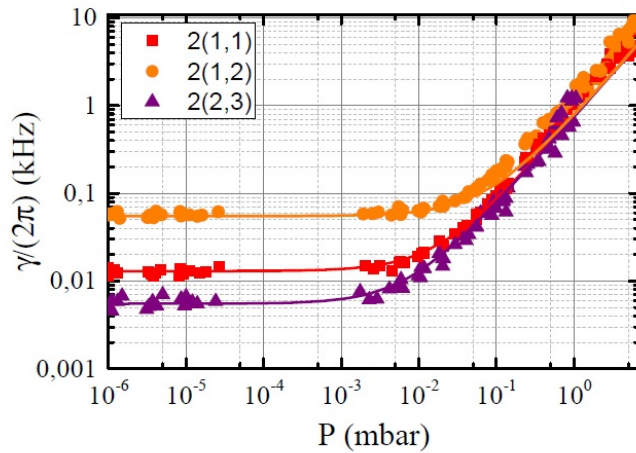


Figure 4.19: Array with $d = 2.95 \mu\text{m}$: Damping rates versus pressure for three modes of membrane 2. Red squares: (1,1) mode, orange circles: (1,2) mode, purple triangles: (2,3) mode. The solid lines show the theoretical predictions. [86]

In Fig. 4.19, the damping rates for the mentioned mechanical modes are plotted for different pressures which confirm that the variations of the damping rates with pressure above 10^{-3} are frequency-independent, as expected from kinetic damping.

4.3.2.2 2.10 μm double-membrane array

In the case of the double-membrane array assembled using the UV resist-spacer approach, the intermembrane separation was slightly smaller ($d = 2.1 \mu\text{m}$) than the previous one and higher quality factor modes were observed for both membranes, which may be an indication that this assembly method does not affect clamping losses as much as the previous one. The fundamental modes of both membranes have resonance frequencies $\omega_1/(2\pi) = 820.1 \text{ kHz}$ and $\omega_2/(2\pi) = 831.2 \text{ kHz}$ with intrinsic Q factors of 86000 and 46000, respectively. Figure 4.20 shows examples of thermal noise spectra at different pressures and the variations of the resonance frequency shifts of both modes with pressure are presented in Fig. 4.21a in logarithmic scale which shows a large positive resonance frequency shifts.

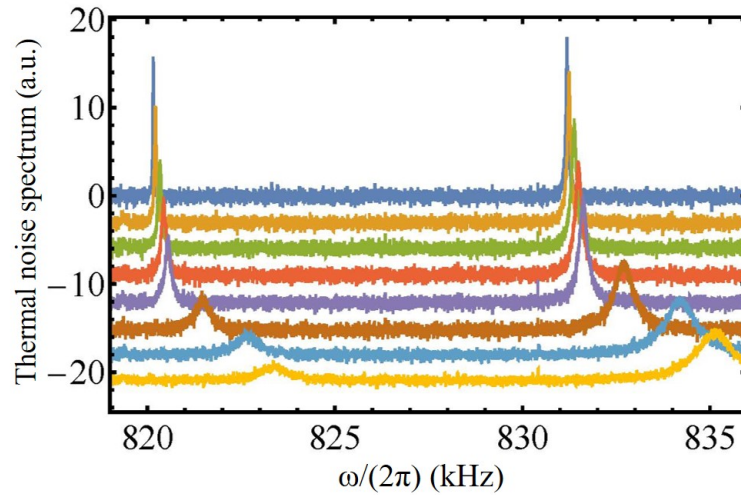


Figure 4.20: Thermal noise spectra of 2.10 μm array around the fundamental mode frequencies for different pressures (from top to bottom: $P = 1.3 \times 10^{-4}, 0.02, 0.07, 0.11, 0.15, 0.47, 0.89, 1.12$ mbar). The background-subtracted spectra are shown with a logarithmic scale and vertically offset for clarity. [86]

At low pressures, both modes experience similar linear frequency shifts with a responsivity of 3 kHz/mbar, as expected from the squeeze film predictions. However, the resonance frequency shifts in the crossing region do not vary in exactly the same way as with the previous sample. Moreover, the lower frequency mode still exhibits a noticeable frequency shift at high pressure, while the high frequency mode sees its responsivity increase, but less than by a factor of 2. Figure 4.21b also shows zoom-in of the resonance frequency variation due to the pressure for both modes in the linear scale where it can be seen that 1(1,1) mode does not stop at the middle of the frequency separation of the modes and its resonance frequency

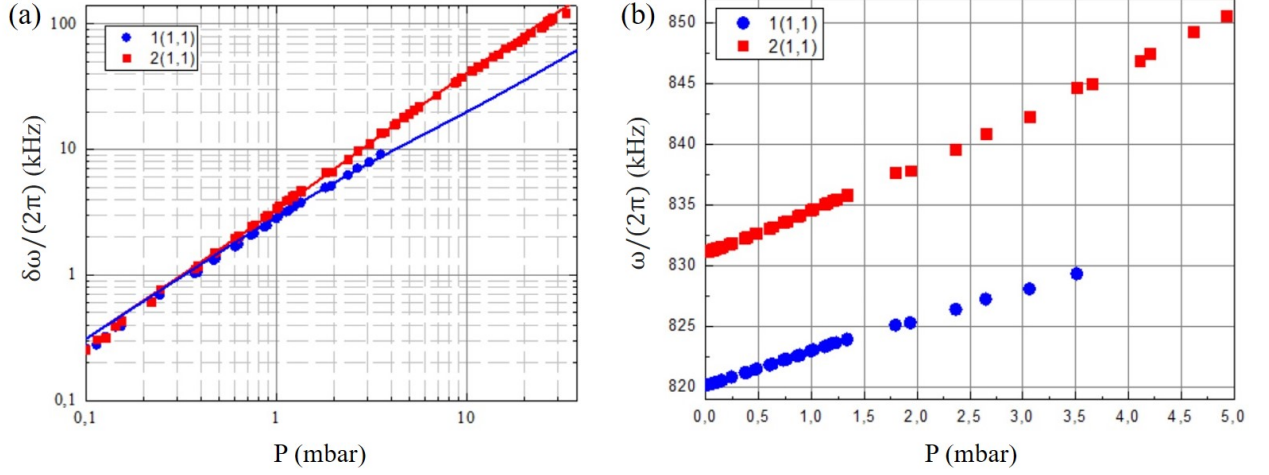


Figure 4.21: (a) Resonance frequency shifts of both membranes' fundamental modes as a function of pressure (logarithmic scale). The solid lines indicate the predictions of the two-spring squeeze model discussed in the text. [86] (b) Resonance frequency shifts of both membranes' fundamental modes as a function of pressure (linear scale).

continues to rise while going towards higher pressure.

This qualitatively different behavior can be accounted for by considering that a fraction of the squeeze film-added spring constant couples the two modes together as previously, while the remaining fraction affects each mode independently. The latter interaction, corresponding to each membrane being spring-coupled to the other one behaving like a "fixed" plate, can be reasonably envisaged if the modes of each membrane are transversely offset with respect to each other or if the membranes are not parallel, as we strongly surmise is the case for this array. Assuming for simplicity the same membrane-"fixed" plate spring constant for both modes, Eqs. (4.15) and (4.16) are modified to:

$$\ddot{x}_1 + (\gamma_1 + \gamma_{air})\dot{x}_1 + \omega_1^2 x_1 + \kappa'_{air}(x_1 - x_2) + \kappa''_{air}x_1 = F_1 \quad (4.20)$$

$$\ddot{x}_2 + (\gamma_2 + \gamma_{air})\dot{x}_2 + \omega_2^2 x_2 + \kappa'_{air}(x_2 - x_1) + \kappa''_{air}x_2 = F_2 \quad (4.21)$$

where κ'_{air} and κ''_{air} are the air-induced membrane-membrane and membrane-plate spring constants, respectively. The normal mode frequency shifts are accordingly given by:

$$\omega_{\pm} = [\omega_0^2 + \delta^2 + 2(\eta' + \eta'')\omega_0 \pm 2\omega_0\sqrt{\delta^2 + \eta'^2}]^{1/2} \quad (4.22)$$

where $\eta' = \kappa'_{air}/(2\omega_0)$ and $\eta'' = \kappa''_{air}/(2\omega_0)$ are both proportional to the pressure, as previously.

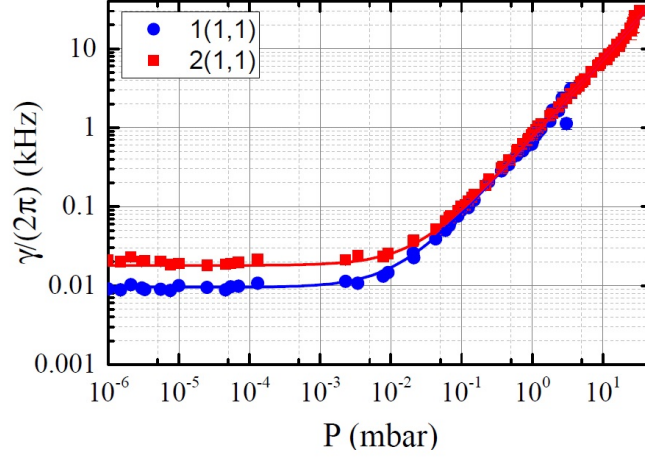


Figure 4.22: Array with $d = 2.10 \mu\text{m}$: Damping of both membranes' fundamental modes as a function of pressure (logarithmic scale). The solid lines indicate the kinetic damping predictions. [86]

At low pressures –as long as $\delta \gg \eta', \eta''$ – both modes experience the same linear frequency shift $\eta' + \eta''$. At high pressures –when $\delta \gg \eta', \eta''$ – the higher frequency mode experiences a shift given by $2\eta' + \eta''$, while the lower frequency mode experiences a shift η'' . The solid lines in Fig. 4.21a show the predictions of Eq. (4.22) when $\eta' + \eta''$ is equal to the full shift η given by the squeeze film model [Eq. (4.13)] for $d = 2.1 \mu\text{m}$ and when $\eta' \simeq \eta''$; these predictions match well the experimental data in the crossover and high pressure regions. The slight apparent discrepancy at pressures around 0.1 mbar is most likely the result of thermal drifts during the measurement series.

The variations of the damping rates of both modes with pressure are shown in Fig. 4.22 and are again consistent with a kinetic damping broadening of the spectra.

4.3.3 Pressure sensitivity

In order to estimate the pressure sensitivity of our sensors in the sub-millibar range and to be less sensitive to the thermal drifts in the chamber, the sequential measurements for the $2.1 \mu\text{m}$ array was carried out during which the air pressure was first quickly increased from high vacuum ($\sim 10^{-5}$ mbar) to a certain value in the sub-millibar range, the thermal noise spectrum acquired, and the pressure quickly decreased again to below 10^{-4} mbar and the thermal noise spectrum measured again.

Therefore, to each point recorded above 10^{-4} mbar was associated a "reference" frequency which was obtained from a fit to the thermal noise spectrum below 10^{-4} mbar to compensate for the thermal drift during the data collection process. Figure 4.23 shows an example of the evolution of the "reference" frequency in time for the 1(1,1) mode.

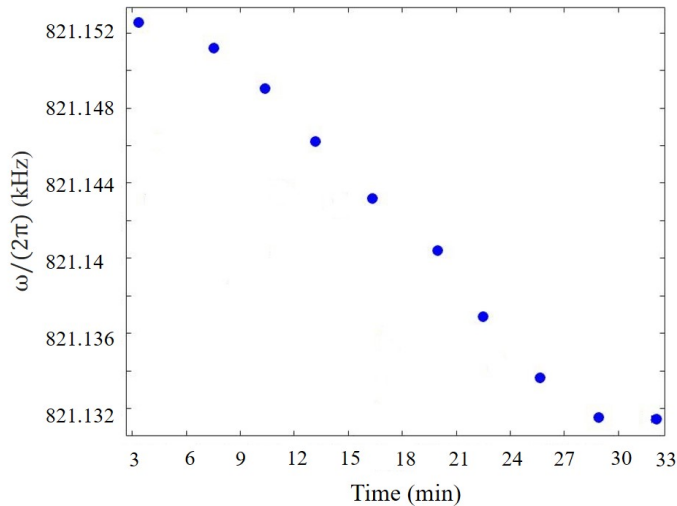


Figure 4.23: Thermal drift of the 1(1,1) mode as a function of time.

By having the "reference" point it is possible to monitor the frequency shift more precisely while changing the pressure. Repeating this sequence for various pressures in the range $10^{-3} - 10^{-1}$ mbar yield the corresponding frequency shifts shown in Fig. 4.24. Equal frequency shifts with a responsivity of 3.1 kHz/mbar are observed for each mode in good agreement with the theoretical expectations. Zooming into the few 10^{-3} mbar region (inset of Fig. 4.24) shows that the current pressure sensitivity using the squeeze film frequency shift is at the 0.1 Pa level.

In principle, the kinetic damping broadening of such high Q mechanical resonances can also be used to infer pressure, although in a species-dependent way. Figure 4.25 shows the variations in the linewidth of the thermal noise spectrum of each mode at various pressures in the same range, as well as the corresponding linewidths measured in high vacuum. The linewidth measurements typically reveal a larger statistical spread than the frequency shift measurements. Given the lower pressure responsivity of the broadening $-\gamma_{air}/P \simeq (2\pi)0.7$ kHz/mbar than that provided by the resonance frequency shift, the resulting sensitivity is found to be slightly worse.

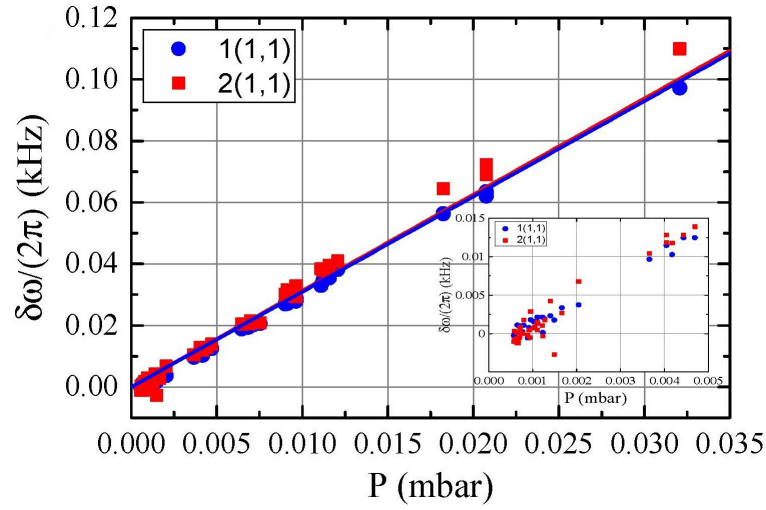


Figure 4.24: Frequency shifts of both membranes' fundamental modes of 2.1 μm array as a function of pressure. The inset shows a zoom into the few 10^{-3} mbar region. [86]

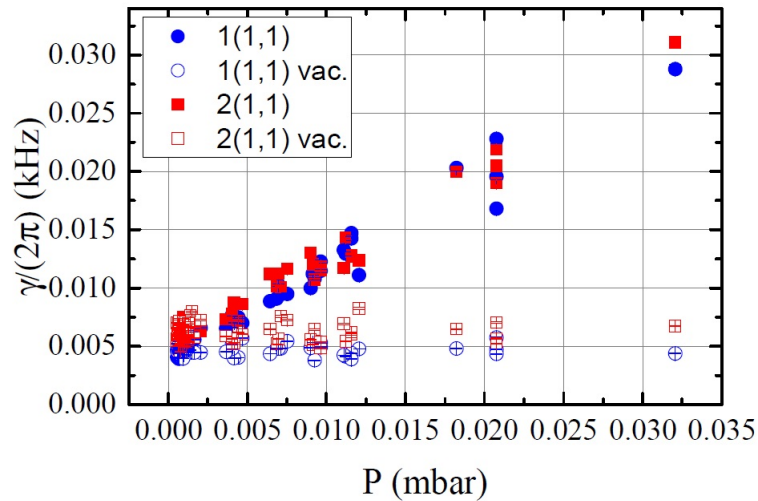


Figure 4.25: Corresponding linewidths (full symbols). The empty symbols show the linewidths measured in the corresponding sequence in a high vacuum (below 10^{-5} mbar). For all data the Lorentzian fit result uncertainties are smaller than the size of the symbols. [86]

To sum up, the effects of air pressure on SiN membrane double-membrane arrays with gaps in the 2-3 micron range were investigated in the rarefied air and transition regimes (10^{-3} -50 mbar), via the measurement of their thermal noise spectra by optical interferometry. The essentially elastic squeeze film force due to the compression of the gas in between the membranes results in strong positive shifts of the mechanical resonance frequencies, as well as coupling between the

membrane resonator modes. The experimental observations are in good agreement with a simple coupled-oscillator model including squeeze film and kinetic damping effects.

4.4 Conclusion

Pressure-induced frequency shift responsivity as high as 4 kHz/mbar was demonstrated for the "short" d membrane sandwiches, which represents a substantial improvement over "medium" d membrane sandwiches. Such performances result from a combination of several factors: the small gap (2-3 μm) and the membrane thickness (< 100 nm) make for strong squeeze film effects, the high tensile stress allows for operating with high-frequency (\sim MHz) and high-Q ($\sim 10^5$) modes, the large area (0.25 mm²) ensures trapping of the gas and an essentially elastic squeeze film force, and last, the squeeze film-induced couplings in the chosen sandwich geometry allows for increasing the pressure responsivity. While the responsivity is already comparable with that of graphene drum sensors and the sub-pascal sensitivity better, the performances of such membrane sandwich pressure sensors could be further enhanced by:

- Improving the experimental setup: Have an active temperature stabilization and better interferometric displacement sensitivity,
- Selecting the mechanical properties: Using a lower frequency mechanical mode and higher Q mechanical resonances which can lead to decrease the statistical spread in the linewidth determination (one can use e.g. mechanical ringdown spectroscopy techniques to determine the mechanical properties),
- Assembly process: Reduction of the intermembrane separation which increases the squeeze film effect,
- Use of strongly frequency degenerate membranes to benefit from the coupling enhancement at low pressures. This could be achieved e.g. by piezoelectric stress control and tuning of the mechanics, as will be discussed in the next chapter.

These steps would make such sensors attractive for direct and absolute pressure measurements in rarefied air and high vacuum environments.

5

Electromechanics in membrane arrays

Suspended dielectric membrane resonators can efficiently couple to electromagnetic fields, whether in the high (optical) frequency domain or in the low (dc, radiofrequency, microwave) frequency domain. The coupling with low-frequency electric fields can be achieved in different ways, e.g. by patterning the membranes with metallic electrodes and capacitive coupling [50, 52], or by using closely lying electrodes and the application of gradient forces [119]. Another approach to induce electromechanical coupling of such tensioned resonators is via the tensile stress. Electromechanical actuation via piezoelectricity of a single membrane resonator through piezoelectricity was demonstrated in [71]. The same method was subsequently applied to tune the eigenfrequencies of the vibrational modes of a pair of distant membranes in an optical cavity [82]. In this chapter we study electromechanical couplings induced in monolithic double-membrane arrays by piezoelectrical control of their tensile stress, results which were reported in [87, 88]. The chapter begins in Sec. 5.1 by describing these electromechanical arrays and the experimental setup used to investigate their properties, followed by a study on the noninvasive tuning of the membranes' mechanical mode spectrum for different samples. The chapter continues with a study of the nonlinear response of such arrays, in particular of the parametric amplification of their thermal fluctuations in Sec. 5.2 and of their resonant excitations in high amplitude states in Sec. 5.3.

5.1 Electromechanical array

5.1.1 Electromechanical array assembly

The samples studied in this chapter include a single membrane and two double-membrane arrays which were assembled in either front-to-front or back-to-front geometries, forming respectively a "medium" and a "long" d array. As shown in Fig. 5.1, three corners of one of the chips were glued with UV resist (in green) to a 6 mm inner diameter piezoelectric transducer (PZT) ring Noliac NAC2123 which was used to apply a compressive force (the horizontal purple arrows indicate the direction of the piezoelectric force for a positive voltage difference between the outer and inner electrodes). As it was explained in Chap. 3, in order to send both RF modulation and DC signal to PZT, we used a combination box letting us combine both inputs using a 100 k Ω resistor and a 4.5 μ F capacitor.

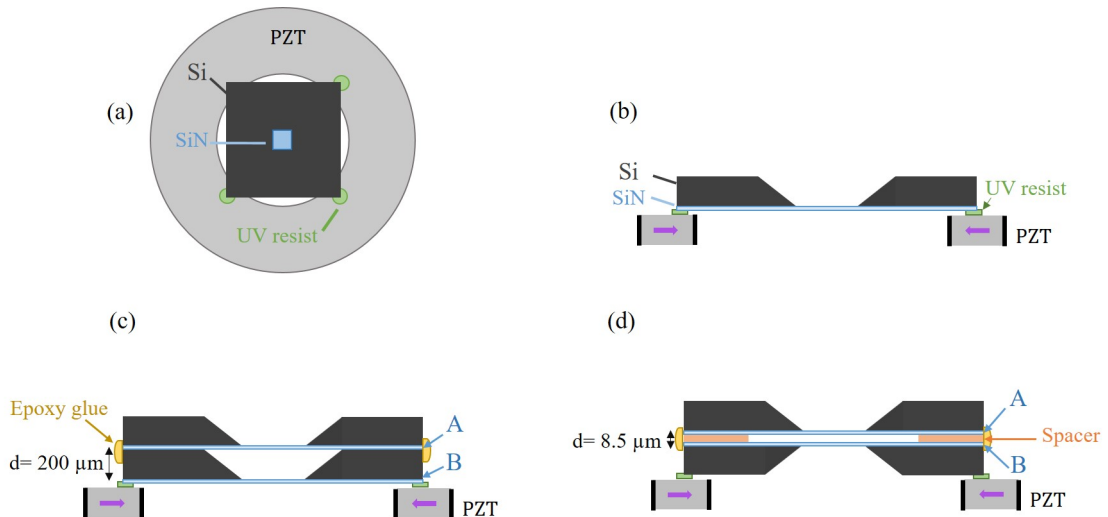


Figure 5.1: Schematic (a) top and (b), (c), (d) transverse cut of the assembly where three corners of the bottom chip glued with the UV resist (in green) on a piezoelectric transducer (PZT) ring (not to scale). (b) A single membrane and (c) a "long" array are glued with the substrate down and (d) shows a "medium" array. The horizontal purple arrows indicate the direction of the compressive piezoelectric force for a positive applied dc-voltage.

In the case of the single membrane (Fig. 5.1b) and the "long" array (Fig. 5.1c), the installations were done in such a way that the substrate was facing down, whereas for the "medium" array –because of the front-to-front geometry in the array assembly– the array was positioned on the back of the Si frame, as shown in Fig. 5.1d. For arrays, in order to distinguish each membrane, we refer to the bottom membrane whose chip was glued to the PZT, as membrane B and the top

one as membrane A. The application of a piezoelectric compressive force to one of the membrane chips (see Fig. 5.2) allows for modifying the tensile stress of the membranes and tuning their mechanical mode spectrum.

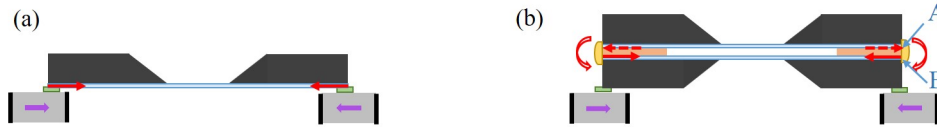


Figure 5.2: Schematic pictures of (a) a single membrane and (b) a membrane array glued on the PZT. The horizontal purple arrows indicate the direction of the compressive piezoelectric force for a positive applied dc-voltage. The horizontal red arrows show the direction of PZT-induced force for modification of the membrane's tensile stress.

In the tensile stress dominated regime, the vibrational mode frequencies of membrane resonators can be estimated by $\omega_{m,n} = \sqrt{\frac{T}{\rho} \frac{\pi}{a} \sqrt{m^2 + n^2}}$, where T is the tensile stress, $\rho = 2700 \text{ kg/m}^3$ is the density of silicon nitride, $a = 500 \text{ }\mu\text{m}$ is the lateral dimension of the membrane and n and m are positive integers. As can be seen in Fig. 5.2a for a single membrane, applying a bias voltage decreases the tensile stress of the membrane which is in contact with the PZT and consequently the mode resonance frequency is reduced. In the case of a double membrane array shown in Fig. 5.2b, regardless of the chosen geometry for the array assembly, the applied bias voltage contracts the bottom chip, which results in less tensile stress for membrane B and causes a bending of the top chip (due to the epoxy glue that connects both chips to each other), which leads to an increased tensile stress for membrane A. Therefore, both membranes are expected to experience opposite frequency shifts due to their tensile stress modifications.

5.1.2 Experimental characterization

The vibrations of the membranes in vacuum (10^{-7} mbar) were monitored by optical interferometry using the setup introduced in Sec. 3.3.4.1 for mechanical characterization. Figure 5.3 presents a summarized graph of the setup used for the single membrane and the "medium" array, while, in case of the "long" array, the beamsplitter in the setup was removed, since good displacement sensitivity for the Fabry Perot etalon could be obtained without it.

As explained in Chap. 3, the mechanical resonance frequencies can be determined by Lorentzian fits to the thermal noise spectrum –typically recorded with a resolution bandwidth of 0.5 Hz and averaged 500 times– and the mechanical quality factors are determined either from the results of the Lorentzian fits to the

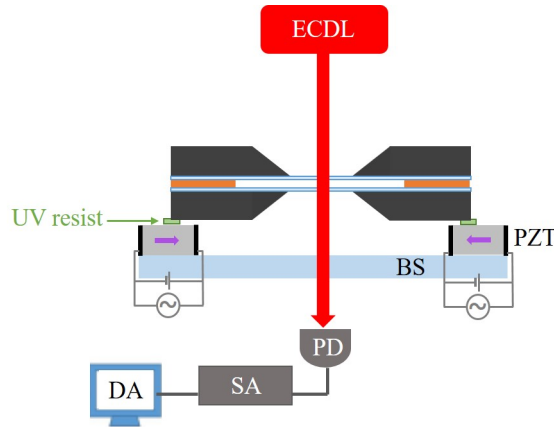


Figure 5.3: Schematic of the optomechanical characterization setup where an array is glued on the PZT ring. ECDL: external cavity diode laser, PZT: piezoelectric transducer, BS: beamsplitter, PD: photodiode, SA: spectrum analyzer, DA; data analysis.

thermal noise spectrum, or by performing ringdown spectroscopy of the resonantly excited mode.

5.1.3 Experimental results

5.1.3.1 Single membrane

The first attempt to tune the mechanical mode frequencies via piezoelectricity was done with a single $(0.5 \times 0.5) \text{ mm}^2$, 100 nm-thick, high-tensile stress ($\sim 0.9 \text{ GPa}$) SiN membrane deposited on $(5 \times 5) \text{ mm}^2$, 200 μm -thick Si frame formed as a notch chip Fig. 5.4. The chip is glued from three corners with its substrate facing down on the PZT ring, as illustrated in Fig. 5.1b.

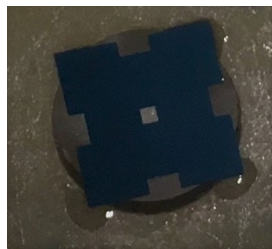


Figure 5.4: Photograph of the single membrane mounted on the piezoelectric transducer ring.

As discussed above, the modification of the membrane's tensile stress due to the applied compressive force causes a linear reduction of the resonance frequencies

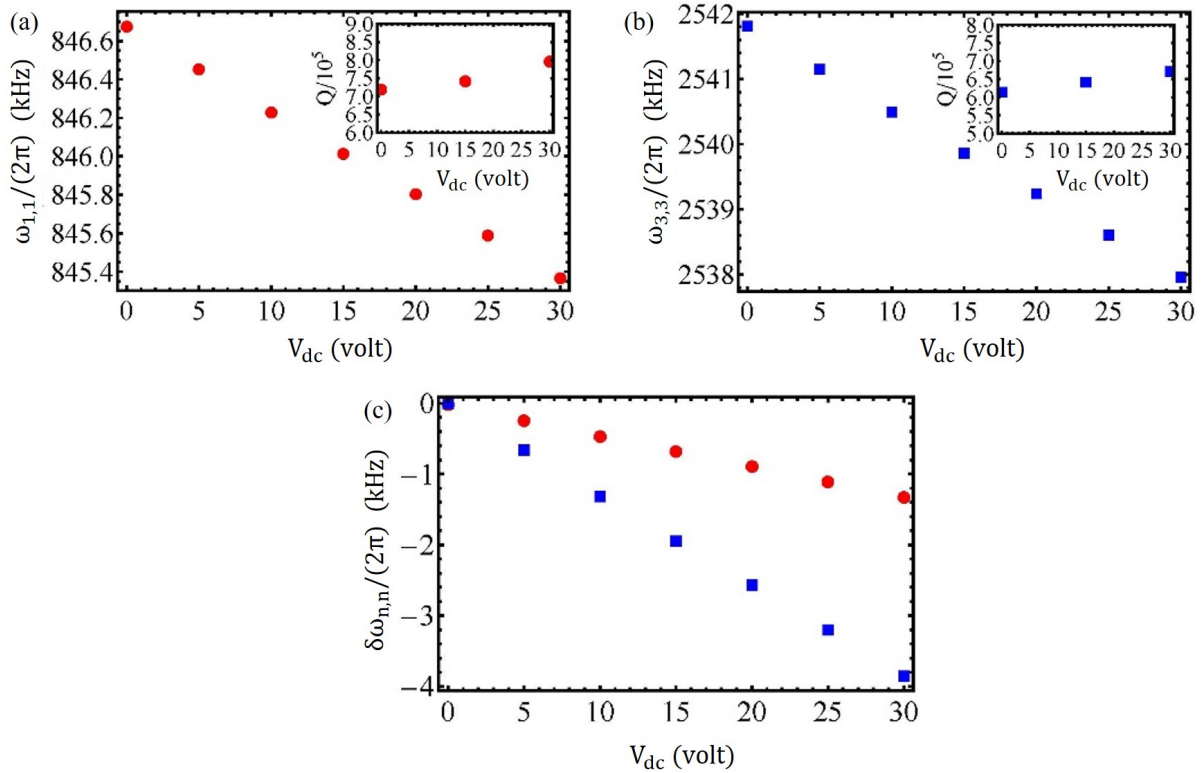


Figure 5.5: Resonance frequencies of (a) (1,1) and (b) (3,3) modes of membrane as a function of the applied bias voltage V_{dc} . Insets in (a) and (b) show mechanical quality factors $Q = \omega/\gamma$ for (1,1) and (3,3) versus V_{dc} , respectively. (c) Frequency shift of both modes as a function of the applied bias voltage V_{dc} . [88]

with the applied bias voltage V_{dc} . This reduction for the fundamental ($m = 1, n = 1$) and a higher-order ($m = 3, n = 3$) mode frequencies is observed in Fig. 5.7a,b. As shown in Fig. 5.7c, the mode (1,1) experiences a resonance frequency shift of -43 Hz/V and the (3,3) mode experiences a shift of -130 Hz/V, which agrees well with the theoretical expectation, since the resonance frequency of the (3,3) mode is three times bigger than that of the (1,1) mode. The mechanical Q factors of both modes were also measured for different bias voltages (insets of Fig. 5.7a,b) and are observed to be only weakly (slight increase for this sample) dependent on the bias voltage.

5.1.3.2 "Long" array

In order to investigate the possibility of tuning of mechanical modes and decrease the frequency separation between them, we performed the same experiment on a

”long” array. The array in this study was made from two notched chips with the same properties as the previous sample. The back-to-front geometry was chosen to put both membranes parallel to each other and the steps of the first generation assembly process were followed by applying epoxy glue from the sides. The fundamental modes of both membranes in this array had much lower Q s than those typically measured with single membrane resonators from the same batch [84]. As also discussed in Chap. 4, during the assembly process of the array, we quite often observed increased clamping losses for the fundamental modes, but not necessarily for higher-order modes. The installation of the array on the PZT ring was done as illustrated in Fig. 5.1c and is shown in Fig. 5.6.

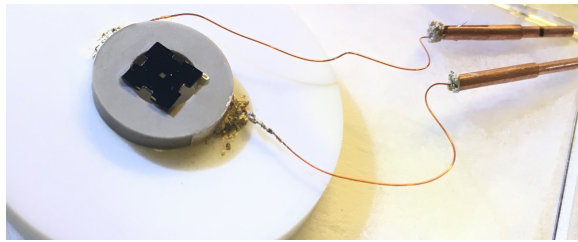


Figure 5.6: Photograph of the ”long” array mounted on the piezoelectric transducer ring.

Figure 5.7a illustrates the observed opposite frequency shifts for both fundamental (1,1) modes of each membrane over the bias voltage range 0-30 V. The compressive force on the bottom chip resulted in a reduced tensile stress for the SiN film (membrane B) deposited on this chip, and thereby a decreasing resonance frequency with positive bias voltage. Membrane A deposited on the top chip, glued at its corners to the bottom one, then experienced increased tensile stress and an increasing resonance frequency with the bias voltage.

The same measurements were performed for (3,3) modes of both membranes and the experimental results are shown in Fig. 5.7b. In order to have a clearer picture of the response, Fig. 5.7c presents the frequency shift of each mode at different bias voltages comparing to its initial value at 0 V. The frequency shift of the A(1,1) (red open squares) and B(1,1) (blue open circles) modes are 9 Hz/V and -16 Hz/V, respectively, and the frequency shifts of the A(3,3) (red full squares) and B(3,3) (blue full circles) modes are 29 Hz/V and -44 Hz/V, respectively. In addition, the insets in Fig. 5.7a,b show that the mechanical quality factors of both modes are essentially independent of the bias voltage.

These measurements were one of our first trials for this effect, and were therefore performed in a conservative way in the sense that we did not dare apply too

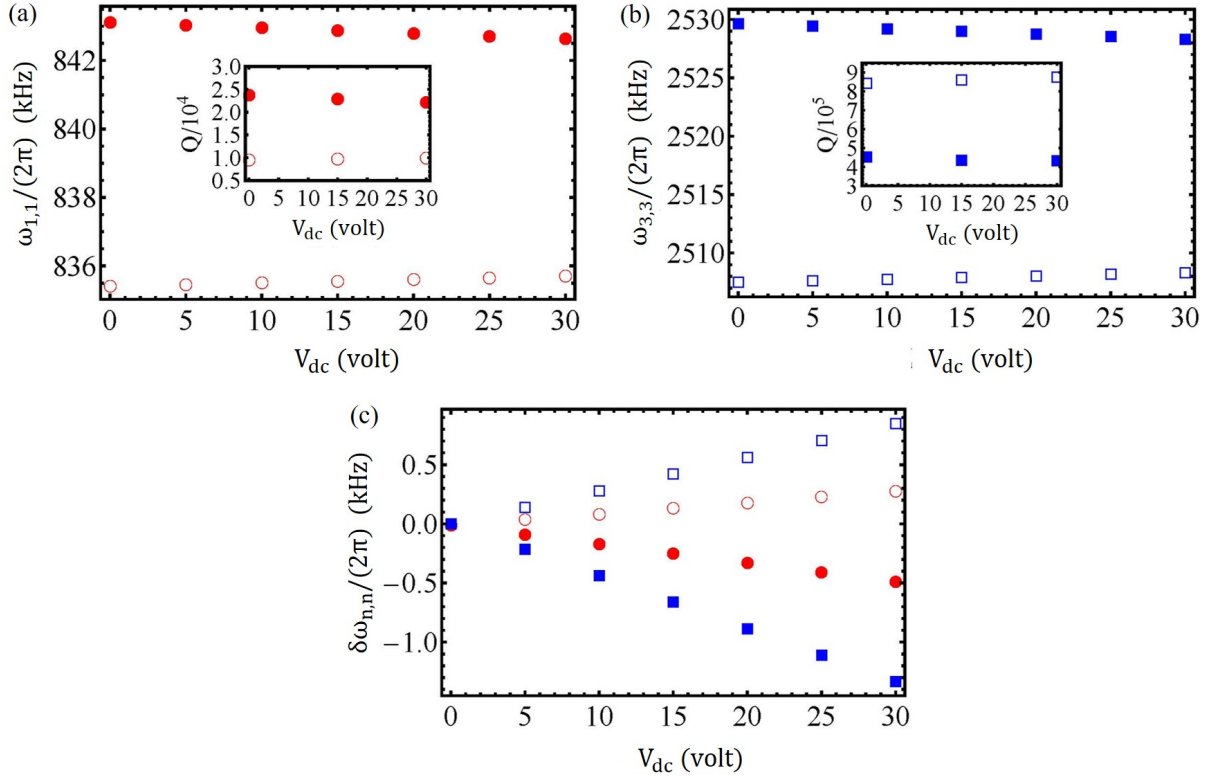


Figure 5.7: Resonance frequencies of (a) the fundamental modes of both membranes A(1,1) (empty circles) and B(1,1) (full circles), (b) A(3,3) (empty squares) and B(3,3) (full squares) as a function of the applied bias voltage V_{dc} . Insets in (a) and (b) show mechanical quality factors $Q_\alpha = \omega_\alpha/\gamma_\alpha$, ($\alpha = A, B$) for (1,1) and (3,3) versus V_{dc} , respectively. (c) Frequency shift of both modes for both membranes as a function of the applied bias voltage V_{dc} . [88]

strong a bias voltage. Even though the measurements explicitly showed that the mechanical modes of both membranes experienced opposite frequency shifts and were moving towards each other while increasing the biasing voltage, the significant bare frequency separation, would most likely have prevented reaching frequency degeneracy within the available PZT range (0-200 V). We thus chose to make another attempt with another ("medium") array for which the bare modes were closer to each other.

5.1.3.3 "Medium" array

In this section, we demonstrate that the vibrational mode frequencies of two membranes in a "medium" array can be tuned to degeneracy and strongly coupled via the application of a static bias voltage to the piezoelectric transducer based on the presented results in [87]. The array was made from two commercial high-stress, 500

mm-square stoichiometric silicon nitride thin films (thickness 92 nm) deposited on a 5 mm-square silicon chip (thickness 500 nm). The chip with an 8.5 μm spacer (membrane A) was assembled parallel to the other chip without any spacer (membrane B) in the front-to-front geometry and the assembly process followed the steps of the first generation arrays, in which epoxy glue on the chips' sides at the corners and a $d \sim 8.5 \mu\text{m}$ intermembrane separation was achieved. In order to mount this array on the PZT in the geometry of Fig. 5.1d, three corners of one of the chips were glued to the PZT ring actuator as shown in Fig. 5.8.

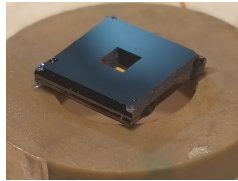


Figure 5.8: Photograph of the "medium" array mounted on the piezoelectric transducer ring. [87]

Before applying any external force, both membranes' fundamental mechanical mode had a quite close resonance frequencies; the (1,1) modes bare frequency difference was only 0.5 kHz, while that of the (2,2) modes was 0.6 kHz. Figures 5.9a and 5.9b show the opposite, linear frequency shifts with similar magnitude for the (1,1) and (2,2) modes of each membrane (positive and negative frequency shifts for membrane A and B, respectively like previous samples) over the bias voltage range 0-80V. As previously, no noticeable effect of the bias voltage on the mechanical quality factors was observed.

Piezoelectric biasing in the geometry of Fig. 5.1d thus allowed for achieving frequency degeneracy of the (1,1) and (2,2) for bias voltages V_{dc} of 56 V and 38 V, respectively. The fact that noninvasive actuation was still possible even in this geometry where there was a much thicker frame (500 μm instead of 200 μm) between the PZT and the membrane, makes the result of the experiment more interesting. To compare the resonance frequency shift of both fundamental modes in both geometries for the array, one should look at the same voltage range. In the bias voltage range 0 – 30 V, the frequency shifts of the A(1,1) mode for "long" and "medium" arrays are 9 Hz/V and 99 Hz/V, respectively, and the frequency shifts of the B(1,1) are -16 Hz/V and -129 Hz/V, respectively. Thus, the "medium" array experiences larger frequency shifts than the "long" array for both membranes.

The intermode coupling via the frame/spacer structure can also be investigated by analyzing the observed thermal noise spectrum around the degeneracy points, as shown in Fig. 5.10 where thermal noise spectra in the vicinity of the (1,1) and (2,2)

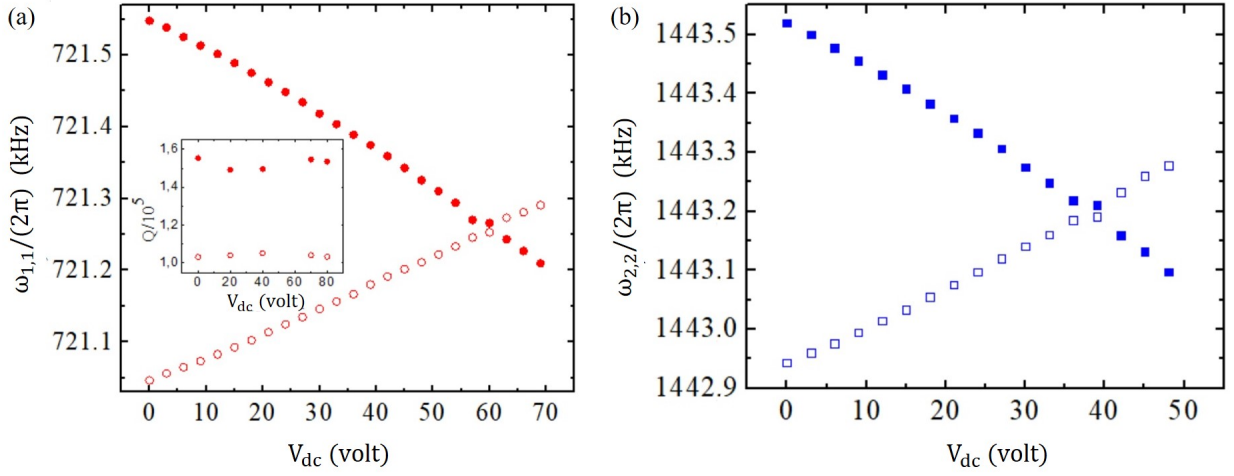


Figure 5.9: Resonance frequencies of (a) the fundamental modes of both membranes A(1,1) (empty circles) and B(1,1) (full circles) and (b) A(2,2) (empty squares) and B(2,2) (full squares) as a function of the applied bias voltage V_{dc} . The inset in (a) shows the mechanical quality factors $Q_\alpha = \omega_\alpha/\gamma_\alpha$, ($\alpha = A, B$) of (1,1) modes versus V_{dc} . [87]

mode resonances spectra are sorted by the dc voltage values in ascending order from bottom to top. These spectra can be understood on the basis of a simple coupled oscillator model (explained in Sec. 2.1.3) in which the dynamics of the mode amplitudes $x_{A,B}$ are given by

$$\ddot{x}_A + \gamma_A \dot{x}_A + (\omega_A + \varepsilon_A V_{dc})^2 x_A = \eta(x_B - x_A) + F_A, \quad (5.1)$$

$$\ddot{x}_B + \gamma_B \dot{x}_B + (\omega_B + \varepsilon_B V_{dc})^2 x_B = \eta(x_A - x_B) + F_B \quad (5.2)$$

where $\gamma_{A,B}$ are the mode mechanical damping rates, $\varepsilon_{A,B} V_{dc}$ are the linear voltage dependent frequency shifts, η is the intermode coupling constant and $F_{A,B}$ are the thermal noise forces (divided by the mode effective mass). Fourier transforming these equations readily yields the Fourier component amplitudes at frequency ω , e.g.,

$$x_A = \frac{\chi_B(\omega) F_A(\omega) + \eta F_B(\omega)}{\chi_A(\omega) \chi_B(\omega) - \eta^2}, \quad (5.3)$$

$$x_B = \frac{\chi_A(\omega) F_B(\omega) + \eta F_A(\omega)}{\chi_B(\omega) \chi_A(\omega) - \eta^2}, \quad (5.4)$$

where

$$\chi_\alpha(\omega) = -\omega^2 - i\gamma_\alpha \omega + (\omega_\alpha + \varepsilon_\alpha V_{dc})^2 + \eta \quad (\alpha = A, B). \quad (5.5)$$

The interferometric signal measured by the spectrum analyzer was proportional to the noise spectrum of $x_A - x_B$

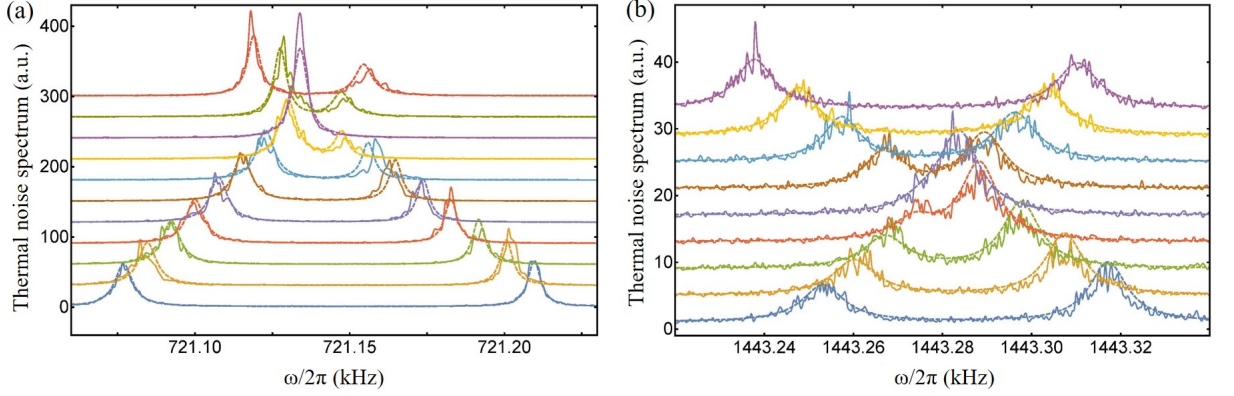


Figure 5.10: Thermal noise spectrum for different bias voltages around the degeneracy point for (a) (1,1) modes and (b) (2,2) modes. V_{dc} is varied from 40 V (lower curve) to 60 V (upper curve) in (a) and from 33 V (lower curve) to 41 V (upper curve) in (b). The spectra are offset vertically for clarity. The dashed lines show the results of a global fit to the coupled oscillator model described in the text. [87]

$$S_{x_A-x_B}(\omega) = \frac{|\chi_B(\omega) - \eta|^2 S_{F_{thA}}(\omega) + |\chi_1(\omega) - \eta|^2 S_{F_{thB}}}{|\chi_A \chi_B - \eta^2|^2}. \quad (5.6)$$

The dashed lines in Fig. 5.10 show the results of a global fit of the data to the model, fixing the mechanical damping rates and thermal force amplitudes using the spectra far from the degeneracy points, and leaving as free parameters the voltage-dependent frequency shift rates $\varepsilon_{A,B}$, as well as the intermode coupling rate $\bar{\eta} = 2\eta/(\omega_A + \omega_B)$. The resulting spectra are observed to match well the observed data, in particular in the avoided crossing region, where the intermode coupling plays a significant role. Remarkably, the extracted value for the (1,1) modes, $\bar{\eta}/(2\pi) \simeq 8$ Hz, was found to be slightly larger than both mechanical decay rates $\gamma_A/(2\pi) \simeq 7$ Hz and $\gamma_B/(2\pi) \simeq 4.5$ Hz, which placed such an electromechanical array at the border of the strong coupling regime. For the (2,2) modes, whose mechanical quality factors were a bit lower, $\bar{\eta}/(2\pi) \simeq 8$ Hz, was found to be slightly larger than both mechanical decay rates $\gamma_A/(2\pi) \simeq 7$ Hz and $\gamma_B/(2\pi) \simeq 7$ Hz was slightly smaller than $\gamma_{A,B}/(2\pi) \simeq 10$ Hz.

The possibility to (~strongly) couple the membranes was shown, however, it would be interesting to perform similar studies on even shorter arrays, such as the ones used in the previous chapters, or with stronger actuation, to see if the electromechanical coupling can be further increased.

5.2 Parametric actuation

The parametric amplification of thermal fluctuations of both membranes' fundamental modes can be studied for different bias voltages by applying a resonant parametric modulation close to the second harmonic frequency of the fundamental mode, $\omega_p \simeq 2\omega_{1,1}$, (see Fig. 5.11) and monitoring the evolution of the noise spectrum as a function of the modulation voltage amplitude V_{ω_p} . This section is based on the study presented in [87, 88].

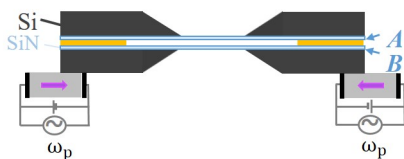


Figure 5.11: Schematic transverse cut of the assembly with a positive parametric dc-voltage modulation applied to the PZT at ω_p and purple arrows indicate the direction of the compressive piezoelectric force.

In principle, a parametric modulation of the spring constant, $k = k_0(1 + \xi \sin(\omega_p t))$, where k_0 is the spring constant in absence of modulation and ξ the normalized modulation amplitude –proportional to the applied modulation voltage amplitude– the classical dynamics of the amplitude around equilibrium of the normal mode considered, $x(t)$, can be modeled by the following differential equation [95]

$$\ddot{x} + \gamma \dot{x} + \omega_m^2 [1 + \xi \sin(\omega_p t)] x = \frac{F_{th}}{m}, \quad (5.7)$$

where $\omega_m = \sqrt{k_0/m}$ is the bare mechanical resonance frequency, m the effective mass of the mode. Assuming a high-quality factor mode ($\omega_m \gg \gamma$) and a pump modulation frequency $\omega_p = 2(\omega_m + \delta)$ close to the second harmonic frequency, the average noise spectrum of such phenomena at the parametric resonance ($\delta = 0$) is given by

$$\bar{S}_{\delta=0}(\omega) = \frac{k_B T \gamma}{m \omega_m^2} \left[\frac{1}{\Gamma^2 (1 - \epsilon)^2 + \omega^2} + \frac{1}{\Gamma^2 (1 + \epsilon)^2 + \omega^2} \right] \quad (5.8)$$

where

$$\Gamma = \frac{\gamma}{2} \quad \text{and} \quad \epsilon = \frac{\omega_m \xi}{4\Gamma} = \frac{Q\xi}{2}. \quad (5.9)$$

As we discussed in Chap. 2, the average noise spectrum is to a good approximation Lorentzian either at low gains ($\epsilon \ll 1$) or close to the parametric threshold

$\epsilon \rightarrow 1$. At the parametric threshold $\epsilon = 1$ –or, equivalently $\xi = 2/Q$ – the linewidth of the noise spectrum diverges (in the absence of nonlinearities).

Moreover, the variance of the amplitude $\Delta x^2 = \langle x^2 \rangle$ –and consequently the average energy in the mode $\bar{E} = \frac{1}{2}m\omega_m^2\langle x^2 \rangle$ – can be obtained:

$$\Delta x^2 = \int_0^\infty \bar{S}(\omega) \frac{d\omega}{2\pi} = \frac{k_B T}{m\omega_m^2} \frac{1}{1 - \epsilon^2/(1 + \delta^2/\Gamma^2)}. \quad (5.10)$$

In the absence of parametric modulation, the average energy is $\bar{E}_0 = \frac{1}{2}k_B T$ whereas in the presence of parametric modulation the value increases as $1/(1 - \epsilon^2)$ and diverges at the threshold. For a nonzero pump detuning, the gain in energy is reduced following Eq. (5.10) and the parametric resonance linewidth depends on both γ and ϵ .

5.2.1 Parametric gain study

Parametric excitation of the membranes of the 8.5 μm membrane array was investigated for different values of the biased voltage by applying a resonant parametric modulation at the second harmonic frequency of the fundamental mode of one of the membranes (membrane B). The evolution of the noise spectrum of the fundamental modes was then monitored as a function of the modulation voltage amplitude V_{ac} , until the parametric oscillation threshold was reached. The bias voltage V_{dc} , which determined the frequency separation between the fundamental mode frequencies $\Delta = \omega_{1,1}^A - \omega_{1,1}^B$ was chosen in such a way that the second harmonic of the excited fundamental mode frequency, $2\omega_{1,1}^A$ or $2\omega_{1,1}^B$, did not coincide with a (2,2) mode resonance frequency. We verified experimentally that neither the non-resonantly driven (1,1) mode nor the (2,2) modes were not excited in the presence of the parametric drive.

Figure 5.12 shows examples of average noise spectra of membrane B's fundamental mode, obtained for a bias voltage corresponding to a frequency separation $\Delta/(2\pi) = 30$ Hz, and for increasing modulation amplitudes (the voltage amplitude was obtained from the input power from the signal generator after a calibration provided by the monitor output of the combining box shown in Fig. 5.13), which were normalized to the parametric threshold voltage. The results of Lorentzian fits to the data are also shown. It can be seen that the amplified noise spectra are generally well-approximated by Lorentzians with increasing peak value/area and reduced linewidth, as the parametric modulation amplitude is increased.

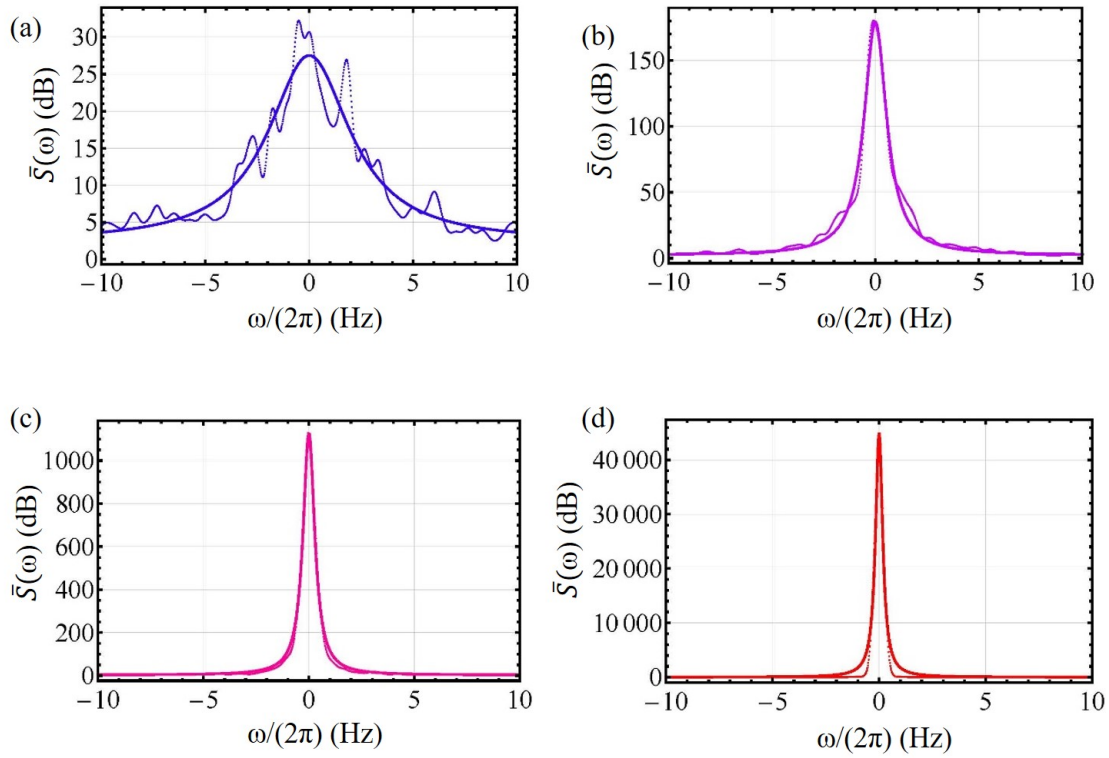


Figure 5.12: Average noise spectra of B(1,1) at a bias voltage corresponding to $\Delta/(2\pi) = 30$ Hz and for different modulation amplitudes corresponding to (a) $\epsilon = 0.069$, (b) $\epsilon = 0.809$, (c) $\epsilon = 0.908$, (d) $\epsilon = 0.996$. The solid lines are the results of Lorentzian fits to the data. The y -axis scale, in arbitrary units, is the same for all figures. [88]

The average energy is obtained by numerical integration of the spectrum and the energy gain –i.e. the ratio \bar{E}/\bar{E}_0 of the average energy for a given ϵ to the average energy for $\epsilon = 0$ – is shown in Fig. 5.14a as a function of ϵ (where $\epsilon = 1$ corresponds to a pump power of 12.8 dBm). Parametric gains of about 100 were observed for this mode at this particular bias voltage before the parametric oscillation threshold was reached. The solid line represents the result of a fit with a function of the form $1/(1 - \epsilon^2)$, according to Eq. (5.10).

The variations of Γ obtained from HWHM of the Lorentzian fits with ϵ is also shown in Fig. 5.15b in which the solid line shows a linearly decreasing linewidth of the form $\Gamma_B(1 - \epsilon)$, where Γ_B is the HWHM in absence of modulation. As one approaches the threshold, effects due to the finite resolution bandwidth of the spectrum analyzer become visible and the measured linewidth is effectively limited by the RBW of the spectrum analyzer. This does not affect the determination of the average energy, however, since the latter is related to the integral of the

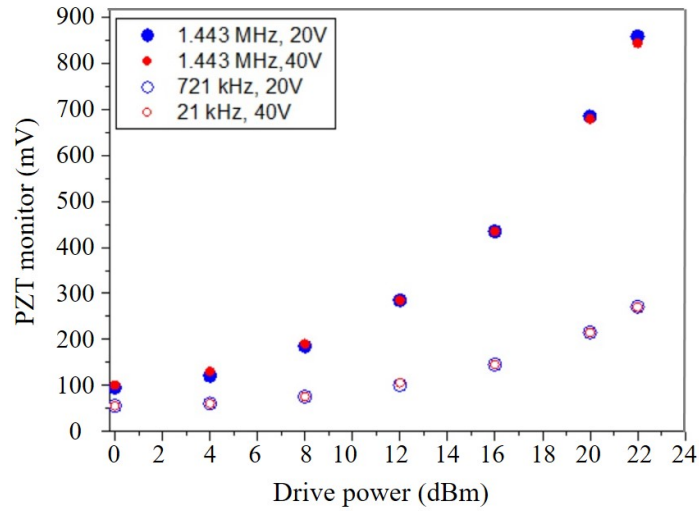


Figure 5.13: Measured voltage from the monitor output of the combining box at dc bias voltages of 20 and 40 V as a function of the modulation drive power in dBm at 721 kHz and 1.443 MHz frequencies.

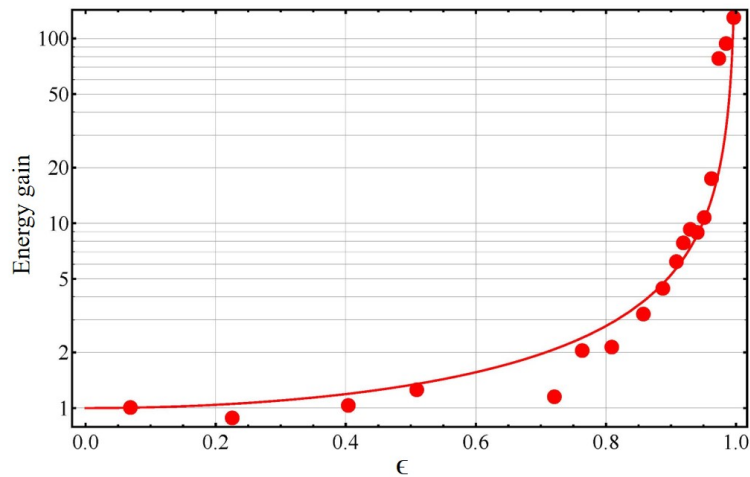


Figure 5.14: Energy gain \bar{E}/\bar{E}_0 as a function of the normalized parametric modulation amplitude ϵ for B(1,1) at a bias voltage corresponding to $\Delta/(2\pi) = 30$ Hz. The solid line shows the result of a fit to Eq. (5.10). [88]

noise spectrum and is independent of the RBW. Similar behavior –though with different gains and thresholds, as will be discussed further– were observed for both fundamental modes and different bias voltages.

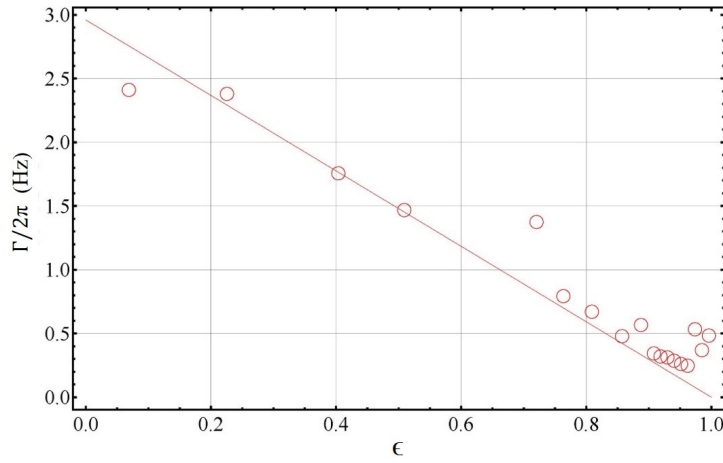


Figure 5.15: HWHM of the B(1,1) noise spectrum resulting from the Lorentzian fit, as a function of ϵ at a bias voltage corresponding to $\Delta/(2\pi) = 30$ Hz. The solid line represents a linearly decreasing linewidth of the form $\Gamma_B(1 - \epsilon)$. [88]

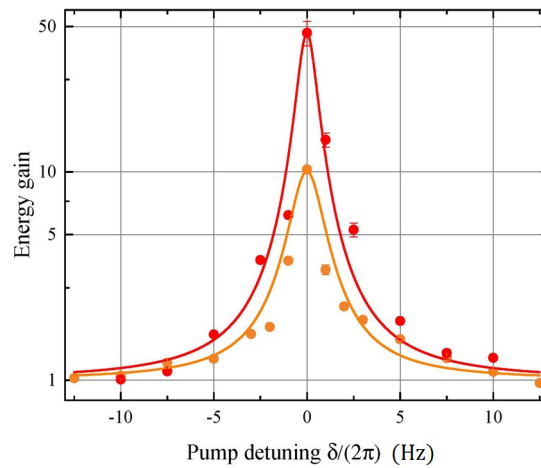


Figure 5.16: Energy gain as a function of pump detuning δ for membrane B's fundamental mode for $\Delta/(2\pi) = 250$ Hz and for two modulation voltage amplitudes corresponding to $\epsilon = 0.949$ (orange dots) and $\epsilon = 0.989$ (red dots). Each point is an average of three data points and the solid lines are the theoretical predictions of Eq. (5.10). [88]

In order to verify the resonant nature of the parametric excitation, the parametric modulation frequency (pump frequency) was slightly varied around the second harmonic frequency of the mode, $\omega_p = 2(\omega_m + \delta)$. Figure 5.16 shows the variation of the energy gain –deduced from the noise spectra as previously– as a function of the pump detuning δ , for membrane B's fundamental mode at a bias voltage such that $\Delta/(2\pi) = 250$ Hz and for two different parametric modulation amplitudes close to

the threshold. The solid lines show the theoretical predictions of Eq. (5.10) in which ϵ is determined by the zero-detuning value and Γ is the HWHM measured in absence of modulation.

Clearly, the highest energy gain was reached at the parametric resonance frequency for the modulation and the linewidth values agree with the theoretical expectation.

5.2.2 Amplification at different bias voltages

After discussing the parametric excitation of membrane B's fundamental mode at the fixed bias voltage, now we can extend the study to the influence of the bias voltage V_{dc} on the resonant parametric amplification of the fundamental modes of both membranes. The energy gains of both modes for different bias voltages are shown in Fig. 5.17 as a function of the modulation amplitude and the lines represent the results of fits to Eq. (5.10). The amplitude is arbitrarily normalized to the parametric amplification threshold amplitude, pump power of 16.4 dBm (which corresponds to $V_{ac} = 448$ mV), of membrane A's fundamental mode at $\Delta/(2\pi) = 250$ Hz. As can be seen, increasing the bias voltage leads to lower parametric oscillation thresholds for both membranes and parametric gains of a few tens to a few hundred were observed until the parametric oscillation threshold $\xi \sim 2/Q$ was reached. Moreover, increasing the bias voltage caused amplified noise spectra at lower values of ϵ for both membranes which meant lower threshold values for parametric excitation. Therefore, we did a more systematic study on the parametric oscillation threshold voltage at comparable V_{dc} s.

Figure 5.18 shows the variations of the parametric oscillation threshold voltage of both membranes' fundamental mode with the bias voltage and illustrates the fact that applying a positive bias voltage strongly reduces the parametric oscillation threshold of both membrane modes, in a seemingly relatively similar fashion in the whole range. Moreover, the thresholds for membrane A are systematically higher than those for B, for a comparable bias voltage. We discuss in the next section the reasons for this lowering of the thresholds and enhancement of the parametric gains with the bias voltage. Let us also note that, due to thermal drifts during the measurements, variations in the highest achievable gains close to the threshold were typically observed, so that one cannot rule out that higher subthreshold gain values may be achievable by better temperature control.

Let us also remark that, at degeneracy ($\Delta = 0$), the single parametrically excited mode picture breaks down as the dynamics of the two coupled modes have in principle to be taken into account [65]. However, since the parametric gain for

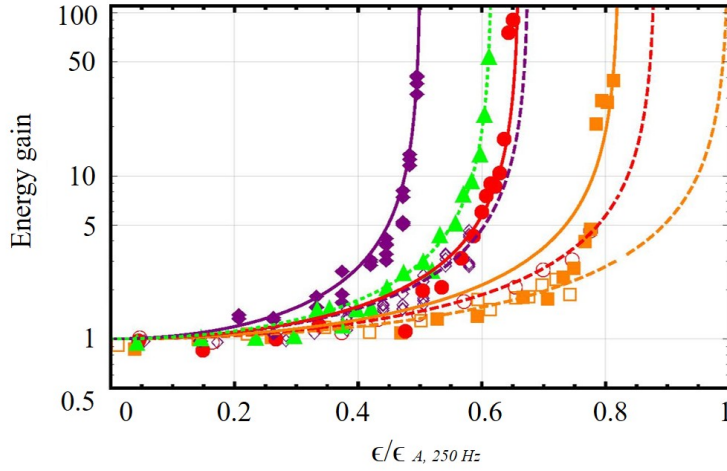


Figure 5.17: Energy gains as a function of normalized modulation amplitude for both fundamental modes for increasing V_{dc} , such that $\Delta/(2\pi) = 250$ Hz (yellow squares), 30 Hz (red circles) and -100 Hz (purple diamonds). The empty and full symbols are for membranes A and B, respectively. The green triangles correspond to the energy gains measured at the degeneracy ($\Delta = 0$). The modulation amplitude is arbitrarily normalized to the threshold amplitude for membrane A's fundamental mode at $\Delta/(2\pi) = 250$ Hz. The solid lines show the results of fits to Eq. (5.10). [88]

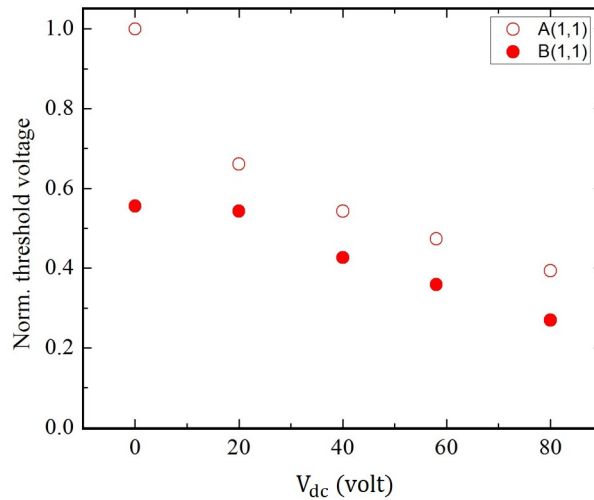


Figure 5.18: The parametric oscillation threshold voltage for both fundamental modes (normalized to the 448 mV threshold voltage of the A(1,1) mode at zero bias voltage) as a function of the bias voltage V_{dc} . [87]

membrane B is substantially stronger than for membrane A, the total amplified noise spectrum becomes quickly dominated by that of membrane B's fundamental mode, as the modulation amplitude is increased. The observed parametric gains

and threshold values thus consistently follow those of membrane B.

5.3 Nonlinearity of the linearly driven mode

To assess the effect of biasing on the dynamical response of the membranes, the (1,1) and (2,2) modes of each membranes were driven independently at their mechanical resonance frequency (Fig. 5.19), for a fixed bias voltage and increasing modulation amplitudes, and the noise spectrum peak value $S(\omega_m)$ was recorded. A linear response was observed over a wide range of modulation amplitudes before nonlinearities kick in.

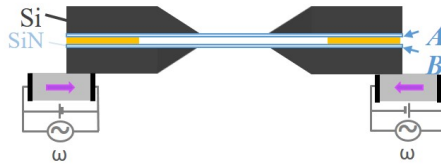


Figure 5.19: Schematic transverse cut of the assembly with a positive linear dc-voltage modulation applied to the PZT at ω_α ($\alpha = A, B$) and purple arrows indicate the direction of the compressive piezoelectric force for a positive voltage difference between the outer and inner electrodes. [87]

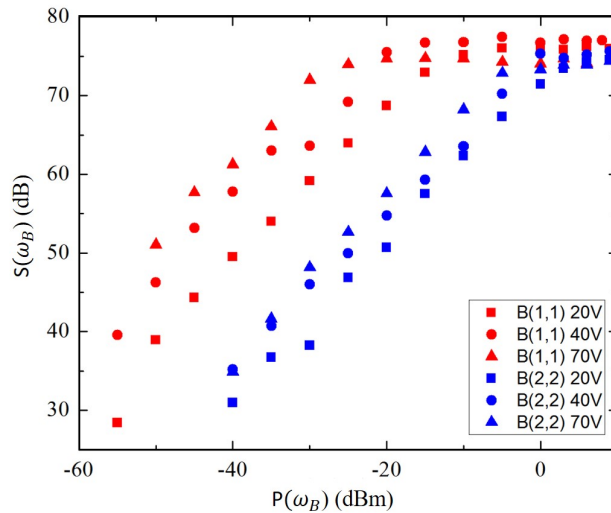


Figure 5.20: Driven response of the (1,1) and (2,2) modes of membrane B: Noise spectrum at resonance (dB) as a function of the power of the modulation voltage at the mechanical resonance frequency $\omega_{(1,1),(2,2)}$ for three different bias voltages. [87]

As can be seen in Fig. 5.20, the linear response of the modes of membrane B

–which is directly coupled to the piezoelectrically stressed silicon frame– is strongly affected by the bias voltage and going towards higher biasing voltages increases the linear response at the same modulation amplitude for both (1,1) and (2,2) modes. In particular, its increased response at $\omega_{2,2} \simeq 2\omega_{1,1}$ accounts well for the decrease of the parametric oscillation threshold of B(1,1) with V_{dc} observed in Fig. 5.18.

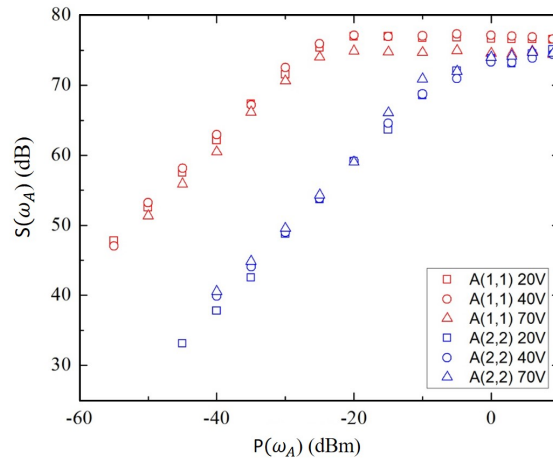


Figure 5.21: Driven response of the (1,1) and (2,2) modes of membrane A: Noise spectrum at resonance (dB) as a function of the power of the modulation voltage at the mechanical resonance frequency ω_A for three different bias voltages. [87]

However, the same measurements presented in Fig.5.21 for membrane A illustrates that the linear response of the modes, whether at the fundamental or the second harmonic frequency, is fairly independent of the bias voltage. Therefore, the lowering of the threshold for membrane A cannot be explained by an enhancement of the direct parametric modulation of its tensile stress, as for membrane B.

To investigate the role of the biasing voltage on the nonlinear response of membrane A, its fundamental mode was driven in the high amplitude regime before the onset of bistability and frequency scans around $\omega_{1,1}$ of the signal were measured in the zero-span mode of spectrum analyzer’s DPX display. The ratio of the amplitude of the driven motion to that of the thermal motion, x/x_0 , was obtained by taking the square root of the noise spectrum peak values with and without modulation. The experiment was repeated for different modulation amplitudes and different bias voltages. The data extracted from these scans are presented in Figs. 5.22, clearly show nonlinearly distorted resonance profiles.

Such profiles can be accurately reproduced by introducing a Duffing nonlinearity (explained in Sec. 2.1.2.4) in the equation of motion for the mode dynamics:

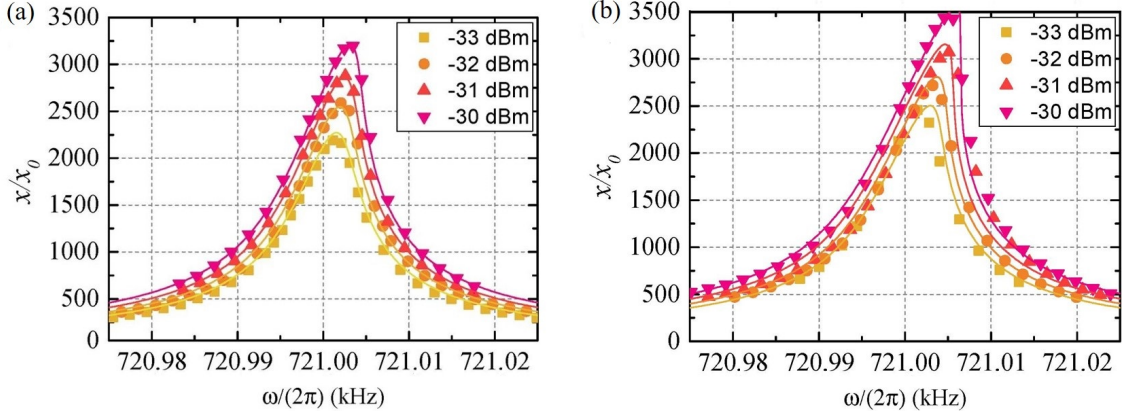


Figure 5.22: Amplitude (normalized to the thermal motion amplitude x_0) of the A(1,1) mode as a function of drive frequency around $\omega_{1,1}$, for different drive powers (a power of -30 dBm corresponds to an applied modulation voltage amplitude of $9.2 \mu\text{V}$): (a) $V_{dc} = 20 \text{ V}$ and (b) $V_{dc} = 80 \text{ V}$. The solid lines show the results of global fits to the nonlinear Duffing oscillator model discussed in the text. [87]

$$\ddot{x} + \gamma\dot{x} + (\omega_m^2[1 + \beta x^2])x = F_{th} + F_\omega \cos(\omega t), \quad (5.11)$$

where F_ω is the amplitude of the driving force at frequency ω and β is the Duffing nonlinearity coefficient. For a small nonlinearity and neglecting the thermal force, the Fourier component amplitude at ω is approximately given by a solution of the implicit equation [102]:

$$|x| = \frac{F_\omega/2}{\sqrt{(\omega_m^2(1 + \frac{3}{4}\beta|x(\omega)|^2) - \omega^2)^2 + \gamma^2\omega^2}}. \quad (5.12)$$

The solid lines in Fig. 5.22 show the results of global fits of this equation to the data, using low drive power scans to fix ω_m and γ and leaving as free parameters β and a global amplitude for the driving force, the respective amplitudes being appropriately scaled by the known applied powers. The fits matches well the observed spectra and yields values of β (in units of $\frac{1}{x_0^2} \times 10^{-12}$) 1.11 ± 0.16 and 1.75 ± 0.07 for $V_{dc} = 20 \text{ V}$ and 80 V , respectively. Application of a bias voltage thus increased the nonlinear response of membrane A to a driving force at the resonance frequency ω_m . Since the nonlinear Duffing term in x^2 in Eq. (5.11) under such driving can be seen to represent an effective modulation at twice the resonance frequency, as in Eq. (5.7), the bias voltage-dependent Duffing nonlinearity coefficient β of A(1,1) is thus expected to be proportional to the A(1,1) parametric modulation coefficient ξ . This is corroborated by the $\sim 60\%$ increase in β when increasing the bias voltage from 20 V to 80 V , which matches well the observed

reduction in the parametric oscillation threshold voltage by about the same amount.

5.4 Conclusion

Noninvasive tuning of the mechanical resonance frequencies of suspended membrane resonators in form of a single membrane and monolithic vertical arrays with "long" and "medium" d was demonstrated using a simple scheme where the membrane chips were directly mounted on a piezoelectric ring actuator. The application of a piezoelectrically controlled force to the bottom chip allowed for modifying the tensile stress of the membrane resonators and thereby change their frequencies, in particular, a negative frequency shift for the membrane on the chip which is in contact with the PZT and a positive frequency shift for the top membrane were observed. It was demonstrated that for membranes with not too different bare mechanical frequencies, tuning to degeneracy by the application of a dc bias voltage to the PZT is possible, as the bottom and top membrane experience opposite frequency shifts with the bias voltage. One could envisage extending these studies by having more membranes in the assembly, different PZT mounting geometries or inserting another PZT on the other side of the array. Such tuning of both the linear and nonlinear response of membrane resonators in vertical arrays is promising for exploring collective effects and investigating phonon dynamics, as is currently investigated with optomechanical membrane arrays [74, 81–83], or for sensing applications using such arrays [85, 86].

We also demonstrated dynamical actuation of both membranes in a "medium" array by the application of an ac voltage at twice the mechanical resonance frequencies of the fundamental modes of the membranes and observing the parametric amplification of their thermal fluctuations until the parametric oscillation threshold was reached. The enhancement of the nonlinear response of membranes' thermal fundamental modes due to the simultaneous application of a dc bias voltage was confirmed and resulted in higher amplification gains and a lowering of the parametric oscillation thresholds. The origin of this dependence was then revealed by the direct linear modulation of the spring constant and the nonlinearity of a linear drive. We showed that the lower membrane (B) experienced a direct modulation of its tensile stress at the parametric resonance frequency through the compression of the lower frame and the parametric oscillation threshold could be reached by the application of a moderate modulation voltage. In contrast, such a direct modulation of the SiN film spring constant was much weaker for the upper membrane (A). However, the application of a static compressive force to the chips resulted in a modification of the nonlinear response/stress of membrane A, which accounts for

the lowering of the parametric amplification threshold with the bias voltage.

While the enhancement of the nonlinear response of membranes is useful for various sensing applications, tuning the modes' resonance frequency and engineering electromechanical couplings in such electro-optomechanical arrays is essential for future collective optomechanics investigations. Increasing the strong coupling and performing more systematic studies on the parametric amplification by considering the non-degenerate and degenerate cases would be promising for further achievements. In principle, by having parametric coupling two modes close to degeneracy and keeping track of the phase, we should be able to engineer two-mode thermomechanical squeezed states, a signature of which may be extracted from the noise spectra. However, for the array studied in Sec. 5.2, the amplified noise spectrum of the modes when brought close to degeneracy was completely dominated by the membrane B mode, whose amplification was much stronger. Investigations with arrays in which more comparable gains/stronger intermembrane couplings can be achieved would be interesting in that respect.

6

Conclusion

In this thesis, we reported on fabrication and optomechanical characterization of SiN membrane arrays along with some practical applications for pressure sensing and electromechanics. In chapter 3, we introduced a new experimental setup for assembling these membrane arrays in a more controllable and precise way which attempted to address some of the challenges encountered during the assembly of the first generation of arrays (PhD thesis of Bhagya Nair [84]). Substantially higher peak transmissions (at the 99.9% level) and also different intermembrane separation d were achieved. The optomechanical characterization of assembled SiN membrane arrays was explained and the results were shown. In particular, the possibility to make arrays with a few micron intermembrane separation opens up for the realization of performant pressure sensors discussed in Chap. 4. The assembly method also initiate reliably making highly parallel, multiple (more than 2) membrane arrays, which would be interesting for more advanced collective optomechanics investigations [21, 27, 28].

Chapter 4 presented an investigation of the effects of pressure on "medium" SiN membrane arrays and the variations of the fundamental drum mode mechanical resonant frequencies and damping with air pressure were determined in the free molecular and quasi-molecular regimes. A kinetic damping linear friction force and a positive resonant frequency shift due to the compression of the fluid inside membrane sandwiches were proportional to the pressure in the range of 0.01 – 10 mbars and the squeeze film-induced hybridization between modes of distinct resonators was revealed. For very non-degenerate resonance frequencies,

as the pressure was increased, the damping was found to be essentially of kinetic origin, while the compression of the fluid was observed to add a positive mechanical spring constant which was proportional to pressure. For membranes with near-degenerate mode frequencies, hybridization of the modes due to the squeeze film effect was also observed where normal "bright" and "dark" modes had to be introduced by a simple spring-coupled oscillator model. The intermembrane spacing was fixed at $8.5 \mu\text{m}$ in the first study and in order to increase the magnitude of the squeeze film effect, we used "short" arrays with subsequently reduced d using the new assembly method (second generation arrays in the front-to-front geometry).

The chapter continued by investigating the effects of air pressure on the mechanical vibrations of high-Q SiN membrane sandwiches with gaps in the 2-3 micron range and characterization of the modifications of their mechanical properties in air in the rarefied and transition regimes (10^{-3} – 50 mbar) was done by the measurement of their thermal noise spectra. The essentially elastic squeeze film force due to the compression of the gas between the membranes resulted in strong positive shifts of the mechanical resonance frequencies of the membranes, which could be enhanced by the air-induced coupling between the membrane modes. The experimental observations were in good agreement with a simple coupled-oscillator model which includes both squeeze film and kinetic damping effects. The high-pressure responsivity (pressure-induced frequency shifts as high as 4 kHz/mbar) exhibited by these squeeze film sensors were substantially improved by a factor~3 over the "medium" sandwiches and sub-pascal sensitivity was demonstrated. These results compare well with state-of-the-art squeeze film graphene sensors [45].

The responsivity and sensitivity of such membrane sandwich pressure sensors could be further enhanced by reduction of the intermembrane separation, lower frequency mechanical mode and higher Q mechanical resonances, strongly frequency degenerate membranes, an active temperature stabilization, and better interferometric displacement sensitivity. Such squeeze pressure sensors would be attractive for absolute and direct pressure measurements in rarefied air or high vacuum environments. Moreover, since the combination of optical measurement and cavity enhancement provides high sensitivity as it was showed for ultrasound sensors for pressure sensing [124], inserting SiN membrane sandwiches inside an optical cavity for pressure sensing measurements would initiate interesting studies.

The goal of the studies presented in Chap. 5 was to investigate electromechanical piezoelectric control of such tensioned resonators via their tensile stress. A simple and noninvasive scheme, for tuning the vibrational mode frequencies of high-Q suspended membrane resonators in forms of a single membrane or two mono-

lithic double-membrane arrays was demonstrated. By controlling the membrane resonators' tensile stress via a piezoelectrically applied compressive force applied to the membrane chip, we demonstrated the possibility to tune mechanical modes into degeneracy as well as strong intermode electromechanical coupling. The nonlinear response of the membranes was studied by performing parametric amplification of the thermal fluctuations of their fundamental modes and the enhancement of their nonlinear response due to the application of a bias voltage was evidenced by the reduction of the parametric oscillation thresholds.

Inserting membranes into an optical cavity allows for strong coupling and collective optomechanics studies [21, 29, 30], therefore, tuning the modes' resonance frequencies and engineering intermembrane couplings of such SiN membrane arrays would be promising for future investigations in these fields such as coherent phonon manipulations [60–65], or entanglement and multimode squeezing generation [29–31, 120]. In addition to the linear engineering, investigating the nonlinear dynamics of membranes [62, 121] in such arrays when resonantly driven into high amplitude states [122, 123] or above the parametric oscillation threshold would be also interesting for synchronization [57, 58]. The enhancement of this nonlinear response is also useful for applications involving thermomechanical squeezing [31, 63, 71, 120].

Furthermore, placing SiN membranes with enhanced reflectivity into a cavity [131] have been used for cavity optomechanics studies [75, 125–130] and are also beneficial for sensitivity enhancements. The possibility to realize one-dimensional subwavelength gratings (SGs) on such suspended membranes to have enhanced and electrically tunable reflectivity, was recently demonstrated in the group [132]. Figure 6.1 shows a SEM image of a SG patterned area which was fabricated via Electron Beam Lithography (EBL).

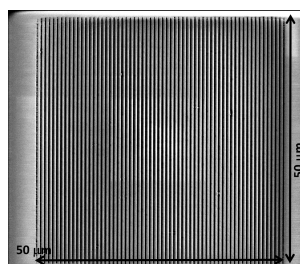


Figure 6.1: Topview SEM image of the $50 \times 50 \mu\text{m}^2$ SG patterned area on a SiN membrane. [132]

The insertion of these patterned membrane resonators, with increased and strongly wavelength dependent reflectivity, into short and/or piezoelectrically controlled arrays, would be extremely interesting in connection with many of the

above-mentioned applications.

Bibliography

- [1] M. Aspelmeyer, T.J. Kippenberg, and F. Marquardt *Cavity optomechanics* Rev. Mod. Phys. 86, 1391, 2014
- [2] T.J. Kippenberg and K.J. Vahala *Cavity opto-mechanics* Opt. Express 15, 17172-17205, 2007
- [3] R. Weiss *Nobel Lecture: LIGO and the discovery of gravitational waves I** Rev. Mod. Phys. 90, 040501, 2018
- [4] B.C. Barish *Nobel Lecture: LIGO and gravitational waves II** Rev. Mod. Phys. 90, 040502, 2018
- [5] K.S. Thorne *Nobel Lecture: LIGO and gravitational waves III** Rev. Mod. Phys. 90, 040503, 2018
- [6] T.J. Kippenberg, H. Rokhsari, T. Carmon, A. Scherer, and . J. Vahala *Analysis of radiation-pressure induced mechanical oscillation of an optical microcavity* Phys. Rev. Lett. 95, 033901, 2005
- [7] A. Schliesser, P. Del'Haye, N. Nooshi, K.J. Vahala, and T.J. Kippenberg *Radiation pressure cooling of a micromechanical oscillator using dynamical backaction* Phys. Rev. Lett. 97, 243905, 2006
- [8] O. Arcizet, P.F. Cohadon, T. Briant, M. Pinard, and A. Heidmann *Radiation-pressure cooling and optomechanical instability of a micromirror* Nature 444, 71–74, 2006
- [9] S. Gigan, H.R. Bohm, M. Paternostro, F. Blaser, G. Langer, J.B. Hertzberg, K.C. Schwab, D. Bauerle, M. Aspelmeyer, and A. Zeilinger *Self-cooling of a micromirror by radiation pressure* Nature 444, 67–70, 2006
- [10] J.D. Thompson, B.M. Zwickl, A.M. Jayich, F. Marquardt, S.M. Girvin, and J.G. E. Harris *Strong dispersive coupling of a high-finesse cavity to a micromechanical membrane* Nature 452, 72-75, 2008

- [11] E. Verhagen, S. Deléglise, S. Weis, A. Schliesser, and T.J. Kippenberg *Quantum-coherent coupling of a mechanical oscillator to an optical cavity mode* Nature 482, 63–67, 2012
- [12] J.D. Teufel, T. Donner, Dale Li, J.W. Harlow, M.S. Allman, K. Cicak, A.J. Sirois, J.D. Whittaker, K.W. Lehnert, and R.W. Simmonds *Sideband cooling of micromechanical motion to the quantum ground state* Nature 475, 359–363, 2011
- [13] J. Chan, T.P. Mayer Alegre, A.H. Safavi-Naeini, J.T. Hill, Al. Krause, S. Gröblacher, M. Aspelmeyer, and O. Painter *Laser cooling of a nanomechanical oscillator into its quantum ground state* Nature 478, 89–92, 2011
- [14] L. Midolo, A. Schliesser, and A. Fiore *Nano-opto-electro-mechanical systems* Nature Nanotechnology 13, 11–18, 2018
- [15] M. Yuan, V. Singh, Y.M. Blanter, and G.A. Steele *Large cooperativity and microkelvin cooling with a three-dimensional optomechanical cavity* Nature Communications 6, 8491, 2015
- [16] C.A. Regal, J.D. Teufel, and K.W. Lehnert *Measuring nanomechanical motion with a microwave cavity interferometer* Nature Physics 4, 555–560, 2008
- [17] D.J. Wilson, C.A. Regal, S.B. Papp, and H.J. Kimble *Cavity optomechanics with stoichiometric SiN films* Phys. Rev. Lett. 103, 207204, 2009
- [18] T. Bagci, A. Simonsen, S. Schmid, L. G. Villanueva, E. Zeuthen, J. Appel, J.M. Taylor, A. Sørensen, K. Usami, A. Schliesser, and E.S. Polzik *Optical detection of radio waves through a nanomechanical transducer* Nature 507, 81–85, 2014
- [19] T.P. Purdy, R.W. Peterson, and C.A. Regal *Observation of radiation pressure shot noise on a macroscopic object* Science 339, 801–804, 2013
- [20] R.W. Andrews, R.W. Peterson, T.P. Purdy, K. Cicak, R.W. Simmonds, C.A. Regal, and K.W. Lehnert *Bidirectional and efficient conversion between microwave and optical light* Nature Physics 10, 321–326, 2014
- [21] A. Xuereb, C. Genes, and A. Dantan *Strong coupling and long-range collective interactions in optomechanical arrays* Phys. Rev. Lett. 109, 223601, 2012
- [22] A. Xuereb, C. Genes, and A. Dantan *Collectively enhanced optomechanical coupling in periodic arrays of scatterers* Phys. Rev. A 88, 053803, 2013
- [23] B. Nair, A. Xuereb, and A. Dantan *Cavity optomechanics with arrays of thick dielectric membranes* Phys. Rev. A 94, 053812, 2016

- [24] H. Seok, L.F. Buchmann, S. Singh, and P. Meystre, *Optically mediated nonlinear quantum optomechanics* Phys. Rev. A 86, 063829, 2012
- [25] T. Kipf and G.S. Agarwal *Superradiance and collective gain in multimode optomechanics* Phys. Rev. A 90, 053808, 2014
- [26] F. Bemani, A. Motazedifard, R. Roknizadeh, M.H. Naderi, and D. Vitali *Synchronization dynamics of two nanomechanical membranes within a fabry-perot cavity* Phys. Rev. A 96, 023805, 2017
- [27] A. Xuereb, A. Imparato, and A. Dantan *Heat transport in harmonic oscillator systems with thermal baths: Application to optomechanical arrays* New J. Phys. 17, 055013, 2015
- [28] A. Xuereb, C. Genes, G. Pupillo, M. Paternostro, and A. Dantan *Reconfigurable long-range phonon dynamics in optomechanical arrays* Phys. Rev. Lett. 112, 133604, 2014
- [29] M. Bhattacharya and P. Meystre *Multiple membrane cavity optomechanics* Phys. Rev. A 78, 041801, 2008
- [30] M.J. Hartmann and M.B. Plenio *Steady state entanglement in the mechanical vibrations of two dielectric membranes* Phys. Rev. Lett. 101, 200503, 2008
- [31] Y.S. Patil, S. Chakram, L. Chang, and M. Vengalattore *Thermomechanical two-mode squeezing in an ultrahigh-Q membrane resonator* Phys. Rev. Lett. 115, 017202, 2015
- [32] T.P. Purdy, P.L. Yu, R.W. Peterson, N.S. Kampel, and C.A. Regal, *Strong optomechanical squeezing of light* Phys. Rev. X 3, 031012, 2013
- [33] K.L. Ekinici, V. Yakhot, S. Rajauria, C. Colosqui, and D.M. Karabacak, *High-frequency nanofluidics: a universal formulation of the fluid dynamics of mems and nems* Lab Chip, 10, 3013-3025, 2010
- [34] K.N. Bhat *Silicon micromachined pressure sensors* J. Indian Inst. Sci. 87, 2007
- [35] S. Joshi, S. Hung, and S. Vengalattore *Design strategies for controlling damping in micromechanical and nanomechanical resonators* EPJ Techniques and Instrumentation 1, 5, 2014
- [36] M. Bao *Micro mechanical transducers* Handbook of Sensors and Actuators, Elsevier Science, 2000

- [37] M. Andrews, I. Harris, G. Turner *A comparison of squeeze-film theory with measurements on a microstructure* Sens. Actuator A-Phys. 36, 79-87, 1993
- [38] S.S. Verbridge, R. Ilic, H.G. Craighead, and J.M. Parpia *Size and frequency dependent gas damping of nanomechanical resonators* Appl. Phys. Lett. 93, 013101, 2008
- [39] M. Suijlen, J.J. Koning, M.A.J. van Gils, and H.C. W. Beijerinck *Squeeze film damping in the free molecular flow regime with full thermal accommodation* Sens. Actuator A-Phys. 156, 171-179, 2009
- [40] M. Bao and H. Yang *Squeeze film air damping in MEMS* Sens. Actuator A-Phys. 136, 3-27, 2007
- [41] T. Veijola, H. Kuisma, J. Lahdenperä, and T. Ryhänen *Equivalent-circuit model of the squeezed gas film in a silicon accelerometer* Sens. Actuator A-Phys. 48, 239-248, 1995
- [42] M. Andrews, G. Turner, P. Harris, and I. Harris *A resonant pressure sensor based on a squeezed film of gas* Sens. Actuator A-Phys. 36, 219-226, 1993
- [43] D.R. Southworth, H.G. Craighead, and J.M. Parpia *Pressure dependent resonant frequency of micromechanical drumhead resonators* Appl. Phys. Lett. 94, 213506, 2009
- [44] L. Kumar, K. Reimann, M.J. Goossens, W.F.A. Besling, R. J. Dolleman, R.H.W. Pijnenburg, C. van der Avoort, L.P.M. Sarro, and P.G. Steeneken *MEMS oscillating squeeze-film pressure sensor with optoelectronic feedback* J. Micromech. Microeng. 25, 045011, 2015
- [45] R.J. Dolleman, D. Davidovikj, S.J. Cartamil-Bueno, H.S.J. vander Zant, P.G. Steeneken *Graphene squeeze-film pressure sensors* Nano Lett. 16, 568-571, 2016
- [46] P.G. Steeneken, Th.G.S. M. Rijks, J.T.M. van Beek, M.J.E. Ulenaers, J. De Coster, R. Puers *Dynamics and squeeze film gas damping of a capacitive RFMEMS switch* J. Micromech. Microeng. 15, 176-184, 2004
- [47] L. Mol, L.A. Rocha, E. Cretu, R.F. Wolffenbuttel *Squeezed film damping measurements on a parallel-plate MEMS in the free molecule regime* J. Micromech. Microeng., 19, 074021, 2009
- [48] M. Stifter, M. Sachse, T. Sauter, W. Hortschitz, F. Keplinger *Pressure dependence of the quality factor of a micromachined cantilever in rarefied gases* J. Phys.: Conf. Ser. 362, 012033, 2012

- [49] A. Kainz, W. Hortschitz, M. Stifter, J. Schalko, F. Keplinger *Optimization of passive air damping of moems vibration sensors* Procedia Eng. 87, 440–443, 2014
- [50] K.L. Ekinici and M.L. Roukes *Nanoelectromechanical systems* Review of Scientific Instruments 76, 061101, 2005
- [51] M. Rossi, D. Mason, J. Chen, Y. Tsaturyan, and A. Schliesser *Measurement-based quantum control of mechanical motion* Nature 563, 53–58, 2018
- [52] I. Kozinsky, H.W.Ch. Postma, I. Bargatin, and M. L. Roukes *Tuning nonlinearity, dynamic range, and frequency of nanomechanical resonators* Appl. Phys. Lett. 88, 253101, 2006
- [53] A. Jockel, M.T. Rakher, M. Korppi, S. Camerer, D. Hunger, M. Mader, and P. Treutlein *Spectroscopy of mechanical dissipation in micro-mechanical membranes* Appl. Phys. Lett. 99, 143109, 2011
- [54] S.C. Jun, X.M.H. Huang, M. Manolidis, C.A. Zorman, M. Mehregany, and J. Hone *Electrothermal tuning of Al–SiC nanomechanical resonators* Nanotechnology 17, 1506–1511, 2006
- [55] S.S. Verbridge, D. Finkelstein, S. Harold, G. Craighead, and J.M. Parpia *Macroscopic tuning of nanomechanics: substrate bending for reversible control of frequency and quality factor of nanostring resonators* Nano Lett. 7, 1728–1735, 2007
- [56] R. St-Gelais, S. Bernard, C. Reinhardt, and J.C. Sankey *Swept-frequency drumhead optomechanical resonators* ACS Photonics 6, 525–530, 2019
- [57] M.H. Matheny, M. Grau, L.G. Villanueva, R.B. Karabalin, M.C. Cross, and M.L. Roukes *Phase synchronization of two anharmonic nanomechanical oscillators* Phys. Rev. Lett. 112, 014101, 2014
- [58] S.-B. Shim, M. Imboden, and P. Mohanty *Synchronized oscillation in coupled nanomechanical oscillators* Science 316, 95–99, 2007
- [59] M. Bagheri, M. Poot, M. Li, W.P.H. Pernice, and H.X. Tang *Dynamic manipulation of mechanical resonators in the high amplitude regime through optical backaction* Nature Nanotechnology 6, 726–732, 2011
- [60] I. Mahboob, K. Nishiguchi, H. Okamoto, and H. Yamaguchi *Phonon-cavity electromechanics* Nat. Phys. 8, 387–392, 2012

- [61] T. Faust, J. Rieger, M.J. Seitner, J.P. Kotthaus, and E.M. Weig *Coherent control of a classical nanomechanical two-level system* Nat. Phys. 9, 485–488, 2013
- [62] F. Yang, F. Rochau, J.S. Huber, A. Brioussel, G. Rastelli, E.M. Weig, and E. Scheer *Spatial Modulation of Nonlinear Flexural Vibrations of Membrane Resonators* PRL 122, 154301, 2019
- [63] J.S. Huber, G. Rastelli, M. Seitner, J. Maximilian, J. Köbl, W. Belzig, M.I. Dykman, and E.M. Weig *Detecting squeezing from the fluctuation spectrum of a driven nanomechanical mode* arxiv:1903.07601, 2019
- [64] H. Okamoto, A. Gourgout, C.-Y. Chang, K. Onomitsu, I. Mahboob, E.Y. Chang, and H. Yamaguchi *Coherent phonon manipulation incoupled mechanical resonators* Nat. Phys. 9, 480–484, 2013
- [65] I. Mahboob, H. Okamoto, K. Onomitsu, and H. Yamaguchi *Two-Mode Thermal-Noise Squeezing in an Electromechanical Resonator* Phys. Rev. Lett., 113, 167203, 2014
- [66] Norcada Inc. <http://www.norcada.com>
- [67] S. Chakram, Y.S. Patil, L. Chang, and M. Vengalattore *Dissipation in ultrahigh quality factor SiN membrane resonators* Phys. Rev. Lett. 112, 127201, 2013
- [68] Y. Tsaturyan, A. Barg, E.S. Polzik, and A. Schliesser *Ultrasqueezed nanomechanical resonators via soft clamping and dissipation dilution* Nature Nanotechnology 12, 776-783, 2017
- [69] A.M. Jayich, J.C. Sankey, B.M. Zwickl, C. Yang, J.D. Thompson, S.M. Girvin, and A.A. Clerk *Dispersive optomechanics: A membrane inside a cavity* New J. Phys. 10 , 095008 , 2008
- [70] D. J. Wilson. *Cavity optomechanics with high-stress silicon nitride Films [PhD thesis]*. California Institute of Technology, 2012
- [71] S. Wu, J. Sheng, X. Zhang, Y. Wu, and H. Wu *Parametric excitation of a SiN membrane via piezoelectricity* AIP Advances 8, 015209, 2018
- [72] A. Yilmaz, S. Schuster, P. Wolf, D. Schmidt, M. Eisele, C. Zimmermann, S. Slama *Optomechanical damping of a nanomembrane inside an optical ring cavity* New J. Phys. 19, 013038, 2017

- [73] T.P. Purdy, P.-L. Yu, N.S. Kampel, R.W. Peterson, K. Cicak, R.W. Simmonds, and C.A. Regal *Optomechanical Raman-ratio thermometry* Phys. Rev. A 92, 031802, 2015
- [74] P. Piergentili, L. Catalini, M. Bawaj, S. Zippilli, N. Malossi, R. Natali, D. Vitali, and G. Di Giuseppe *Two-membrane cavity optomechanics* New J. Phys. 20, 083024, 2018
- [75] C. Reinhardt, T. Müller, A. Bourassa, and J.C. Sankey *Ultralow-noise SiN trampoline resonators for sensing and optomechanics* Phys. Rev. X 6, 021001, 2016
- [76] J. Guo, R.A. Norte, and S. Gröblacher *Integrated optical force sensors using focusing photonic crystal arrays* Opt. Express 25, 9196–9203, 2017
- [77] M. Karuza, C. Biancofiore, M. Bawaj, C. Molinelli, M. Galassi, R. Natali, P. Tombesi, G. Di Giuseppe, and D. Vitali *Optomechanically induced transparency in a membrane-in-the-middle setup at room temperature* Phys. Rev. A 88, 013804, 2013
- [78] S. Camerer, M. Korppi, A. Jöckel, D. Hunger, T.W. Hänsch, and P. Treutlein *Realization of an optomechanical interface between ultracold atoms and a membrane* Phys. Rev. Lett. 107, 223001, 2011
- [79] P. Christoph, T. Wagner, H. Zhong, R. Wiesendanger, K. Sengstock, A. Schwarz, and C. Becker *Combined feedback and sympathetic cooling of a mechanical oscillator coupled to ultracold atoms* New J. Phys. 20, 093020, 2018
- [80] I. Moaddel Haghghi, N. Malossi, R. Natali, G. Di Giuseppe, and D. Vitali *Sensitivity-bandwidth limit in a multimode optoelectromechanical transducer* Phys. Rev. Applied 9, 034031, 2018
- [81] B. Nair, A. Naesby, and A. Dantan *Optomechanical characterization of silicon nitride membrane arrays* Opt. Lett. 42, 1341–1344, 2017
- [82] X. Wei, J. Sheng, C. Yang, Y. Wu, and H. Wu *Controllable two-membrane-in-the-middle cavity optomechanical system* Phys. Rev. A 99, 023851, 2019
- [83] C. Gärtner, J.P. Moura, W. Haaxman, R. A. Norte, and S. Gröblacher *Integrated optomechanical arrays of two high reflectivity SiN membranes* Nano Lett., 18, 7171–7175, 2018
- [84] B. Nair *Towards collective optomechanics with nanomembranes [PhD thesis]*. Aarhus University, 2017

- [85] A. Naesby, S. Naserbakht, and A. Dantan *Effects of pressure on suspended micromechanical membrane arrays* Appl. Phys. Lett. 111, 201103, 2017
- [86] S. Naserbakht and A. Dantan *Squeeze film pressure sensors based on SiN membrane sandwiches* Sensors and Actuators A 298, 111588, 2019
- [87] S. Naserbakht, A. Naesby, and A. Dantan *Electromechanics in vertically coupled nanomembranes* Appl. Phys. Lett. 115, 061105, 2019
- [88] S. Naserbakht, A. Naesby, and A.n Dantan *Frequency tuning and parametric amplification of the vibrations of coupled nanomembranes by piezoelectrical control of their tensile stress* Manuscript in preparation
- [89] W. Weaver, S. Timoshenko, and D. H. Young *Vibration problems in engineering* John Wiley and Sons, Inc 1990
- [90] S. Timoshenko and S. Woinowsky-Krieger *Theory of plates and shells* McGraw-Hill, 1959
- [91] S.S. Rao *Vibration of continuous systems* John Wiley and Sons, Inc 2007
- [92] S.S. Rao *Mechanical vibrations* Addison-Wesley Reading, MA 1993
- [93] L.D. Landau and E.M. Lifshitz *Mechanics (Vol. 1 of: Course of theoretical physics)* Pergamon Press Ltd. 1960
- [94] A. Champneys *Encyclopedia of Complexity and Systems Science* Springer, New York 2012
- [95] D. Rugar and P. Grütter *Mechanical parametric amplification and thermomechanical noise squeezing* Phys. Rev. Lett. 67, 699-702 , 1991
- [96] K.L. Turner, S.A. Miller, P.G. Hartwell, N.C. MacDonald, S.H. Strogatz, and S.G. Adams *Five parametric resonances in a microelectromechanical system* Nature 396, 149–15, 1998
- [97] A. Dana, F. Ho and Y. Yamamoto *Mechanical parametric amplification in piezoresistive gallium arsenide microcantilevers* Appl. Phys. Lett. 72, 1152, 1998
- [98] W. Lacarbonara, S.S. Antman *What is a parametric excitation in structural dynamics* in: ENOC-2008, Saint Petesburg, Russia, 2008
- [99] Branislav Ftorek, Pavol Orsansky, Helena Samajova *Parametric oscillations of the mechanical systems* MATEC Web of Conferences 157, 08002, 2018

- [100] R. Kawaia, K. Lindenberg, C. Van den Broeck *Parametrically modulated oscillator dimer: an analytic solution* Physica A, 312, 119–140, 2002
- [101] A. Leuch, L. Papariello, O. Zilberberg, C.L. Degen, R. Chitra, and A. Eichler *Parametric symmetry breaking in a nonlinear resonator* Phys. Rev. Lett. 117, 214101, 2016
- [102] D.W. Jordan and P. Smith *Nonlinear ordinary differential equations* Oxford, Clarendon Press 1987
- [103] P.J. Holmes and D.A. Rand *The bifurcations of duffing's equation: An application of catastrophe theory* Journal of Sound and Vibration, Volume 44, Issue 2, Pages 237-253, 1976
- [104] A. Xuereb, P. Domokos, J. Asbáoth, P. Horak, and T. Freearge *Scattering theory of cooling and heating in optomechanical systems* Physics Review A 79 , 053810, 2009
- [105] E. Hecht *Optics* Addison-Wesley Reading ,MA 2002
- [106] C. Genes and A. Dantan *Light-matter interactions in multi-element resonators* Journal of Physics B: Atomic, Molecular and Optical Physics, 50, 2017
- [107] A. Gover, A. Nause, E. Dyunin, and M. Fedurin. *Beating the shot-noise limit* Nature Physics, 8, 2012
- [108] M. Jurna, E. Buttner, J.P. Korterik, C. Otto, I. Rimke, and H.L. Offerhaus *Shot noise limited heterodyne detection of CARS signals* Opt. Express 15, 15207-15213, 2007
- [109] F.R. Blom, S. Bouwstra, M. Elwenspoek, and J.H.J. Fluitman *Dependence of the quality factor of micromachined silicon beam resonators on pressure and geometry* Journal of Vacuum Science and Technology B: Microelectronics and Nanometer Structures Processing, Measurement, and Phenomena 10, 19, 1992
- [110] R.G. Christian *The theory of oscillating-vane vacuum gauges* Vacuum 16, 175-178, 1966
- [111] R.B. Bhiladvala and Z.J. Wang *Effect of fluids on the Q factor and resonance frequency of oscillating micrometer and nanometer scale beams* Phys. Rev. E 69, 036307, 2004
- [112] S. Bianco, M. Cocuzza, S. Ferrero, E. Giuri, G. Piacenza, C.F. Pirri, A. Ricci, L. Scaltrito, D. Bich, A. Merialdo, P. Schina, and R. Correale *Silicon resonant microcantilevers for absolute pressure measurement* J. Vac. Sci. Technol. B 24, 1803, 2006

- [113] K.Y. Yasumura, T.D. Stowe, E.M. Chow, T. Pfafman, T.W. Kenny, B.C. Stipe, and D. Rugar *Quality factors in micron- and submicron-thick cantilevers* Journal of Microelectromechanical Systems 9, 117-125, 2000
- [114] R. Pratap and A. Roychowdhury *Vibratory MEMS and squeeze film effects. In: Micro and smart devices and systems* Springer Tracts in Mechanical Engineering, Springer 2014
- [115] R.Lqtenberg and H.A.C. Tilmans *Electrostatically driven vacuum-encapsulated polysilicon resonators, Part I. Design and fabrication* Sens. Actuator A-Phys. 45, 57-66, 1994
- [116] K.L. Ekinci, V. Yakhot, S. Rajauria, C. E Colosqui, and D.M. Karabacak *High-frequency nanofluidics: a universal formulation of the fluid dynamics of MEMS and NEMS* Lab on a chip, 10, 2010
- [117] M. Biet, F. Giraud, B. Lemaire-Semail *Squeeze film effect for the design of an ultrasonic tactile plate* EEE Transactions on Ultrasonics, Ferroelectrics, and Frequency Control 54, 2678-2688, 2007
- [118] F. Völklein and A. Meier, *Microstructured vacuum gauges and their future perspectives* Vacuum 82, 420-430, 2007
- [119] M.J. Seitner, M. Abdi, A. Ridolfo, M.J. Hartmann, and E.M. Weig *Parametric Oscillation, Frequency Mixing, and Injection Locking of Strongly Coupled Nanomechanical Resonator Modes* PRL 118, 254301, 2017
- [120] A. Pontin, M. Bonaldi, A. Borrielli, L. Marconi, F. Marino, G. Pandraud, G.A. Prodi, P.M. Sarro, E. Serra, and F. Marin *Dynamical Two-Mode Squeezing of Thermal Fluctuations in a Cavity Optomechanical System* Phys. Rev. Lett. 116, 103601, 2016
- [121] T. Antoni, K. Makles, R. Braive, T. Briant, P.-F. Cohadon, I. Sagnes, I. Robert-Philip, and A. Heidmann *Nonlinear mechanics with suspended nanomembranes* EPL 100, 68005, 2012
- [122] I. Mahbooba and H. Yamaguchi *Piezoelectrically pumped parametric amplification and Q enhancement in an electromechanical oscillator* Appl. Phys. Lett. 92, 173109, 2008
- [123] D.W. Carr, S. Evoy, L. Sekaric, H.G. Craighead, and J.M. Parpia *Parametric amplification in a torsional microresonator* Appl. Phys. Lett. 77, 1545, 2000
- [124] S. Basiri-Esfahani, A. Armin, S. Forstner, and W.P. Bowen *Precision ultrasound sensing on a chip* Nature communication 10, 132, 2019

- [125] C.H. Bui, J. Zheng, S.W. Hoch, L.Y.T. Lee, J.G.E. Harris, and C. Wei Wong *High-reflectivity, high-Q micromechanical membranes via guided resonances for enhanced optomechanical coupling* Appl. Phys. Lett. 100, 021110, 2012
- [126] U. Kemiktarak, M. Durand, M. Metcalfe, and J. Lawall *Cavity optomechanics with sub-wavelength grating mirrors* New J. Phys. 14, 125010, 2012
- [127] U. Kemiktarak, M. Metcalfe, M. Durand, and J. Lawall *Mechanically compliant grating reflectors for optomechanics* Appl. Phys. Lett. 100, 061124, 2012
- [128] S. Bernard, C. Reinhardt, V. Dumont, Y.-A. Peter, and J.C. Sankey *Precision resonance tuning and design of SiN photonic crystal reflectors* Opt. Lett. 41, 5624-5627, 2016
- [129] R.A. Norte, J.P. Moura, and S. Gröblacher *Mechanical Resonators for Quantum Optomechanics Experiments at Room Temperature* PRL 116, 147202, 2016
- [130] X. Chen, C. Chardin, K. Makles, C. Caër, S. Chua, R. Braive, I. Robert-Philip, T. Briant, P.-F.s Cohadon, A. Heidmann, T. Jacqmin, and S. Deléglise *High-finesse Fabry–Perot cavities with bidimensional Si₃N₄ photonic-crystal slabs* Light: Science and Applications 6, e16190, 2017
- [131] A. Naesby and A. Dantan *Microcavities with suspended subwavelength structured mirrors* Optics Express 26, 29886-29894, 2018
- [132] B. Nair, A. Naesby, B.R. Jeppesen, and A. Dantan *Suspended silicon nitride thin films with enhanced and electrically tunable reflectivity* Physica Scripta 94, 125013, 2019